On the stability of anode (photo-)electrocatalysts in the solar to hydrogen nexus

Über die Stabilität von Anoden(photo-)elektrokatalysatoren in der Solar zu Wasserstoff Verbindung

Der Technischen Fakultät
der Friedrich-Alexander-Universität
Erlangen-Nürnberg

zur
Erlangung des Doktorgrades Dr.-Ing.

vorgelegt von

Julius Knöppel
aus Bad Honnef, Deutschland

Als Dissertation genehmigt
von der Technischen Fakultät
der Friedrich-Alexander-Universtität Erlangen-Nürnberg
Tag der mündlichen Prüfung: 23.08.2022

1. Gutachter: Prof. Dr. Karl J. J. Mayrhofer
2. Gutachter: Prof. Dr. Markus Valtiner

Remember, kids, the only difference between screwing around and science is **writing it down**.
-Adam Savage, Mythbusters

Abstract

The sustainable production of hydrogen for energy storage and utilization is an important cornerstone to overcome global warming, one of the biggest challenges of our time. One method to produce hydrogen is (photo-)electrochemical water splitting. It facilitates the sustainable splitting of water into hydrogen and oxygen from electricity or directly from the sunlight. While tremendous progress has been made in the last decades towards utilizing (photo-)electrochemical water splitting, both technologies are still not at the needed technology readiness level for widespread application. One of the issues that both technologies share is limited operational stability.

Proton exchange membrane water electrolysis (PEMWE) the most promising technology for electrochemical water splitting, suffers from high demand of scarce iridium on the anode side, where the oxygen evolution (OER) reaction takes place. Testing in aqueous model systems (AMS) shows high degradation rates of iridium under OER conditions. However, recent reports question the applicability of these results for PEMWE.

In the field of photoelectrochemistry, on the other hand, stability is still widely neglected. Stability is mostly estimated with thermodynamical data or measured with simple photoelectrochemical methods without gaining profound knowledge of the underlying degradation mechanisms.

This work aims at deepening the understanding of the degradation mechanisms of anode catalysts (photo-)electrochemical water splitting. The discrepancy between iridium degradation in AMS and membrane electrode assemblies (MEA), as used in PEMWE is confirmed by comparing iridium dissolution in a scanning flow cell coupled to an inductively coupled plasma mass spectrometer (SFC-ICP-MS), an AMS, to iridium in a specifically designed (MEA). The reasons for the measured discrepancy are determined by a thorough parameter study, identifying overestimated acidity and stabilization with time in MEA as the main contributors to the discrepancy.

In order to determine the stability of photoelectrocatalysts in real-time, the SFC-ICP-MS system is modified by introducing a light source. This modified setup is used to measure the dissolution of WO_3, a seemingly stable photoanode, as proof of concept. In further studies, the dissolution stability of WO_3 was determined in different electrolytes, identifying varying reaction kinetics at the photoanode surface as the origin for diverging stability between electrolytes. The application of iridium as co-catalyst to the WO_3 surface, as the final study, gives insights into photoanode stability under varied catalytic conditions and the best utilization of scarce iridium.

Kurzfassung

Die nachhaltige Erzeugung von Wasserstoff zur Energiespeicherung und Nutzung ist ein wichtiger Grundpfeiler um die globale Erwärmung, eine der größten Herausforderungen unserer Zeit, aufzuhalten. Eine Methode zur Erzeugung von Wasserstoff ist (photo-)elektrochemische Wasserspaltung. Diese ermöglicht die Spaltung von Wasser in Wasserstoff und Sauerstoff aus nachhaltigem elektrischem Strom, oder direkt aus dem Sonnenlicht. Obwohl in den letzten Jahrzehnten bereits große Fortschritte bezüglich der Nutzung von (photo-)elektrochemischer Wasserspaltung gemacht wurden, sind beide Technologien noch nicht auf dem nötigen Technologiereifegrad für eine flächendeckende Anwendung. Eine Schwäche beider Technologien ist ihre Betriebsstabilität.
Die vielversprechendste Technologie für elektrochemische Wasserspaltung, Protonaustauschmembranwasserelektrolyse (PEMWE), bedarf großen Mengen Iridiums, eines raren Edelmetalls, auf der Anodenseite, an der die Sauerstoffentwicklungsreaktion (OER) stattfindet. Untersuchungen in wässrigen Modellsystemen (AMS) zeigen hierbei hohe Iridiumdegradationsraten unter OER-Bedingungen. Allerdings stellen kürzlich veröffentlichte Resultate die Anwendbarkeit auf PEMWE Systeme in Frage.
In der photoelektrochemischen Forschung wird die Betriebsstabilität hingegen immer noch weitgehend ignoriert. Stabilität wird hier meistens thermodynamisch abgeschätzt oder mit einfachen photoelektrochemischen Methoden, die keinen tieferen Einblick in die zugrundeliegenden Degradationsmechanismen gewähren, ermittelt.
Diese Arbeit zielt darauf ab, das Verständnis über die Degradationsmechanismen von Anodenkatalysatoren in der (photo-)elektrochemischen Wasserspaltung zu erweitern. Die Diskrepanz in der Degradation von iridiumbasierten Katalysatoren in AMS sowie Membranelektrodeneinheiten (MEA), wie in der PEMWE verwendet, wird durch den Vergleich der Iridiumauflösung in einer Rasterflusszelle gekoppelt an ein induktiv gekoppeltes Plasmamassenspektrometer (SFC-ICP-MS) und einer speziell entwickelten MEA bestätigt. In einer detaillierten Parameterstudie werden eine überschätzte Azidität sowie eine Stabilisierung über die Betriebsdauer in der MEA als Hauptverursacher für die Diskrepanz ermittelt.
Um auch die Auflösungsraten von Photoelektrokatalysatoren in Echtzeit bestimmen zu können, wird das SFC-ICP-MS System durch Einbauen einer Lichtquelle modifiziert. Der erweiterte Teststand ermöglicht es die Auflösungsraten von WO_3, einem mutmaßlich stabilen Photoanodenmaterial, als Machbarkeitsnachweis zu bestimmen.
In weiteren Studien wird die Auflösungsstabilität von WO_3 in verschiedenen Elektrolyten bestimmt. Hierbei zeigt sich, dass verschiedene Reaktionskinetiken auf der Oberfläche der Photoelektrode ursächlich für divergierene Stablität zwischen

den Elektrolyten sind. Die finale Studie, in der Iridium als Co-Katalysator auf der WO_3 Oberfläche aufgetragen wird gibt Einblicke in die Stabilität von Photoanoden unter veränderten katalytischen Bedingungen und die bestmögliche Nutzung von Iridium.

Acknowledgements

Writing this dissertation would not have been possible without all the scientific exchange and support from my supervisors, collaborators, and fellow teammates. Thus, I would like to express my gratitude to those who assisted in the process one way or another.
First, I would like to thank Prof. Dr. Karl Mayrhofer for giving me the opportunity to conduct my research in his department in the newly founded Helmholtz-Institute Erlangen-Nuremberg and taking on the review of this thesis. Furthermore, I would like to thank Prof. Mayrhofers former students and team members from the Max-Planck Institute for Iron research, for developing the remarkable SFC-ICP-MS system. Without this seminal work, the results shown in this thesis would not have been possible.
Second I would like to thank Prof. Dr. Markus Valtiner for taking the time and consideration to evaluate this thesis as second reviewer.
I deeply thank Dr. Serhiy Cherevko for chosing me as a PhD student and for his guidance and supervision throughout the last years. He always understood to find a balance between demand and encouragement that allowed me to grow as a researcher and a person.
As our team group grew substantially during my stay and always had fruitful discussions, it is impossible to highlight every individual contribution. Nevertheless, special thanks go to Dr. Florian Speck and Dr. Daniel Sandbeck for introducing me to the laboratory techniques and helping with accidents that I caused as an inexperienced newbie. Furthermore, I would like to highlight my thanks to Dr. Daniel Escalera and Dr. Attila Kormányos for their support and corrections during the writing process of the papers, which make up a large part of this thesis.
In addition, I would like to thank my collaborators for their contributions to this work. I want to thank Maximilian Möckl from the ZAE Garching for developing the precipitation-free MEA cell, performing measurements, and collecting liquid samples, Markus Bierling for providing SEM and STEM micrographs, Dr. Thomas Böhm for preparing samples for STEM measurements, Kevin Stojanovski for assisting with H-cell measurements, Britta Mayerhöfer for spray-coating photoelectrodes, and André Hofer for performing ALD, UV-vis, and XRD measurements. For programming the LabView software controlling the LED of the PEC-ICP-MS, programming I thank Jonas Möller.
Furthermore, I would like to thank my collaborators from within the Kopernikus P2X project for broadening my view on the topic of electrochemical water splitting and constructive discussions.
Also, the people who did not contribute scientifically but in the background should

not be forgotten. I want to thank Dr. Susanne Spörler, Dr. Sabine Popp, Dr. Carolin Meyer, Anja Kraus and Magdalena Mikulaschek for their administrative support and Achim Mannke, Stephan Borlein and Stephan Fiegl from the Workshop.
Furthermore, I would like to thank my group, the electrochemical energy conversion team, formerly known as the stability group, as well as the electrocatalysis department and the whole institute for the excellent working atmosphere. Before the hardships of Corona, we always managed to keep a healthy work-life balance.
Last but not least, I would like to thank my close friends and family for their ongoing support and for providing the necessary balance counterpart to the demanding work during my PhD time.

Contents

Glossary

$\mathbf{e}^-$	electron.
$\mathbf{h}^+$	hole.
AEM	anion exchange membrane.
ALD	atomic layer deposition.
AMS	aqueous model system.
AST	accelerated stress test.
aSTEM	annular scanning transmission electron microscopy.
CB	conduction band.
CE	counter electrode.
CV	cyclic voltammetry.
DART	differential analysis in real-time.
DEMS	differential electrochemical mass spectrometry.
DI	deionized.
EDX	energy-dispersive X-ray spectroscopy.
EOL	end-of-life.
EQCM	electrochemical quartz crystal microbalance.
FIB-SEM	focused ion beam scanning electron microscope.
FTO	fluorine-doped tin oxide.
GC	glassy carbon.
GDE	gas diffusion electrode.
GR	galvanic replacement.

HAADF High-angle annular dark-field.

HER hydrogen evolution reaction.

ICP-MS inductively coupled plasma mass spectrometer.

IPA isopropyl alcohol.

IS internal standard.

LED light-emitting diode.

LSV linear sweep voltammogram.

MEA membrane electrode assembly.

OCP open circuit potential.

OER oxygen evolution reaction.

ORR oxygen reduction reaction.

PC polycarbonate.

PEC photoelectrochemical.

PEC-ICP-MS photoelectrochemical scanning flow cell coupled to an ICP-MS.

PEC-SFC photoelectrochemical scanning flow cell.

PEEK polyether ether ketone.

PEM polymer electrolyte membrane.

PEMWE proton exchange membrane water electrolyzer.

PP polypropylene.

PTFE polytetrafluorethylene.

PTL porous transport layer.

PVD physical vapor deposition.

RDE rotating disc electrode.

RE reference electrode.

RHE reversible hydrogen electrode.

SEM scanning electron microscopy.

SFC scanning flow cell.

SFC-ICP-MS scanning flow cell coupled to an inductively coupled plasma mass spectrometer.

SHE standard hydrogen electrode.

STEM scanning transmission electron microscopy.

UV-vis Ultraviolet-visible.

VB valence band.

WE working electrode.

XPS X-ray photoemission spectroscopy.

XRD X-ray diffraction.

1 Introduction

1.1 The Climate Crisis - Transition to a new energy economy

The growing energy demand of an increasing world population and the man-made climate change due to greenhouse gasses in the atmosphere, and its consequences, are the biggest challenge of our time. While the first theoretical considerations of potential rising temperatures in the atmosphere due to increasing CO_2 concentrations were published over a century ago [1], the records from the last decades confirm these considerations. An alarming correlation between CO_2 concentrations in the atmosphere from burning fossil fuels on the one hand, and rising temperatures, on the other hand, is observed. However, our energy mix is still dominated by fossil fuels [2–5].

In order to decrease CO_2 emissions and limit global warming to a non-threatening degree, the united nations ratified the Kyoto protocol in 1997 and subsequently the Paris climate change agreement in 2015 [6, 7]. With the Paris agreement, the ratifying states committed to the goal of limiting global warming until the year 2100 to 1.5 °C to 2 °C. To meet these goals, a substantial change in how mankind generates and consumes green energy is necessary [8, 9].

The increasing CO_2 emissions of greenhouse gasses are driven by a continuously growing energy demand of the increasing world population. Fossil fuels are the primary energy source used to satisfy the energy demand. As shown in Figure 1.1 a), the gross energy production relies mostly on coal, natural gas, and oil. The increasing need for energy in the last 30 years resulted mainly in the increasing use of fossil fuels. Renewable energy sources, such as wind energy and solar energy, only play a marginal role in the current energy scenario.
While renewable energies are only utilized scarce in today's energy mix, their potential is enormous. All renewable energies, like wind, water, solar, and biomass, are, depending on local circumstances, applicable to produce vast amounts of electric energy. Nevertheless, the renewable energy source with the highest potential is solar energy [10]. Solar energy has the technical potential to produce as much energy as 15 000 PWh/yr and surpasses the technical potential of all other renewables combined [11, 12]. As the current average energy consumption rate was

15 TW in 2010 and was expected to rise to 27 TW in 2050, coverage of only 2 % of the world's land mass with solar modules would be sufficient to meet the world's energy demand [11, 13–16]. However, not all of the world's energy demand can be

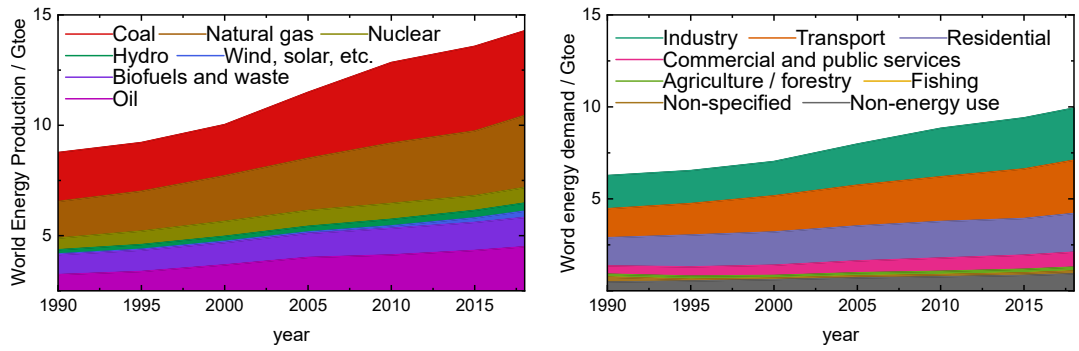

Figure 1.1: Representation of the world's total energy production and energy consumption a) *Total energy production by energy source.* ***b)*** *Total energy consumption by sector. Own representation with data from the international energy agency [17].*

met in electrical energy. If the total energy consumption by sector, as depicted in Figure 1.1 b) is taken into account, it is evident that the transportation sector, as one of the strongest drivers of energy consumption in a globalized world, can not be powered by electrical energy directly from the grid. Cars, ships, and aviation will always depend on energy sources, independent from the power grid. Furthermore, the intermittency of solar energy provides another obstacle on the way to a solar-powered future. Thus, to become independent from external influences, such as the day-night cycle and cloudy weather, energy storage and distribution capacities must be upscaled alongside renewable energy production.
One of the most promising technologies to provide energy storage and distribution is electrochemical energy conversion. Chemical reactions, driven by electrical energy, produce chemicals that can be, later on, converted back to electrical energy or, in the case of CO_2 reduction, be utilized like fossil fuels [18–20]. The reaction, which can provide these functions on the smallest time-scale, is electrochemical hydrogen production.

1.2 The Hydrogen Economy

One of the pillars that a sustainable energy economy could be built on is the hydrogen economy. When Jules Verne envisioned it in his 1874 novel the mysterious island, the hydrogen economy was considered science fiction, but science caught up over the last century [21, 22].
An early concept was sketched by John Bockris in 1972 [23]. Nuclear power plants are built on platforms floating in the oceans to enable better heat dissipation in this scenario. The energy produced in these power plants is not distributed via high

voltage lines but converted to hydrogen via water electrolysis. The so produced hydrogen is used as an energy distribution vector. In a fuel cell reaction, where hydrogen recombines with oxygen, it can produce electrical energy.
Due to catastrophic events such as Chernobyl 1986 and Fukushima 2011, nuclear power plants are no longer considered a solution for energy production in several parts of the world. However, in the light of the transition to a more sustainable energy economy, the idea of hydrogen as an energy distribution vector is more relevant than ever [22]. The amount of research funding is increasing steadily. On the international level, the European Union launched flagship projects as EnergyX [24] and Sunrise [25] to support research on increasing utilization of renewable energies, and specifically sunlight, to produce green hydrogen. Furthermore, individual states have launched initiatives to support the utilization of renewables, as Germany with the Kopernikus P2X project [26] and a national hydrogen strategy [27], the UK with the H2Fsupergen project [28], and the Joint Center for Artificial Photosynthesis in the US [29]. Also the Desertec project, which was supposed to produce energy in the Sahara, to be transported to Europe by a power grid, is planning to shift its focus to green hydrogen production [30].
Several technologies can drive the conversion of solar energy to hydrogen. Two of the most promising are water electrolysis and photoelectrochemical water splitting. Water electrolysis, as depicted schematically in Figure 1.2 a), converts electrical energy from solar energy to hydrogen. Photoelectrochemical water splitting, as depicted in Figure 1.2, b), includes both, the solar cell and the water electrolyzer in one device. Sunlight is here converted to hydrogen, directly driven by semiconducting photoelectrodes.

Water electrolysis is the more mature technology. Alkaline water electrolyzers,

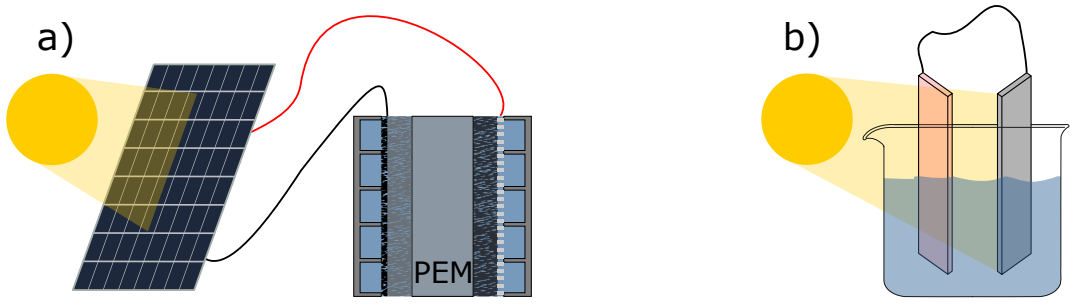

Figure 1.2: Schematic representations of solar to hydrogen technologies. a) *Proton exchange membrane water electrolyzer (PEMWE) coupled to a solar cell. The current generated from the solar cell is used to produce hydrogen in the PEMWE.* ***b)*** *Photoelectrochemical system. The semiconducting photoelectrodes integrate the functionality of both, the solar cell and PEMWE in one device.*

where electrodes are immersed in a KOH bath, have been around for a century on the industrial scale [31, 32]. While they are reliable and cheap, as their electrodes are made from abundant materials, their dynamicity is limited, providing a problem for the storage of intermittent solar energy. Higher dynamicity is provided by pro-

ton exchange membrane water electrolyzer (PEMWE), where the aqueous electrolyte is exchanged by a polymer electrolyte membrane (PEM) between the electrodes [33]. Recent studies show that the production of hydrogen by PEMWE provides the potential of reducing CO_2 emissions of the hydrogen sector by 75% if electrolysis is run exclusively on renewable energies [34]. However, the catalysts used in the porous electrodes of PEMWE depend on scarce and expensive noble metals. Especially iridium, used as an anode catalyst in high loadings, already increased significantly in price shortly after upscaling of electrochemical hydrogen production in 2020, as shown in Figure 1.3 [35]. When PEMWE is upscaled to the GW scale further increasing market prices are expectable [36].

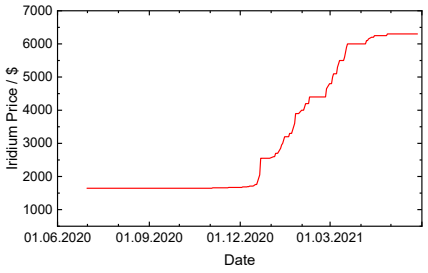

Figure 1.3: Iridium market prices between July 01st, 2020 and May 28th, 2021 [35].

While PEMWE as a technology is already used on an industrial scale, photoelectrochemical water splitting is considered a technology for a more distant future [37], although semiconducting photoelectrodes are made from more abundant metals and metal oxides. Before a broad application is possible, however, the photoelectrodes have to increase in technology readiness, such as efficiency and durability.

1.3 About the Scope of this Work

The lifetime of (photo-)electrochemical hydrogen production systems is a crucial factor in the transition to the new energy system, as it is one building block in economical operation. Thus, one of the critical challenges for the commercialization of these systems is to achieve a broad understanding of the underlying degradation mechanisms to find successful mitigation strategies.
However, the understanding of degradation mechanisms in both systems is yet, still in the early stages. In electrochemical systems, great success in understanding the degradation mechanisms of iridium, the state-of-the-art electrocatalyst for the oxygen evolution reaction (OER), has been made in aqueous model systems. Several *in-situ* techniques were developed and allowed a direct connection between electrochemical operation and degradation. However, several recent studies indicated that the knowledge gained in aqueous systems does not translate to the industrial level, where PEM are used as electrolytes [38–40].
The understanding of stability in photoelectrochemical systems, on the other hand,

is at an even earlier stage. Thermodynamic considerations dominate the discussion, and kinetic effects are widely ignored [41, 42]. Pre/post analysis micrographs of photoelectrodes, which show significant signs of degradation after just several hours, are sometimes buried in supplementary information [43]. Most of the works, however, do not cover stability at all.
However, in the broader picture, stability is getting in the focus of research interest for both systems. A Scopus search with boolean operators, as shown in Figure 1.4 a) shows exponentially growing research interest in the stability of electrocatalyts in the last 10 years. The results of a similar search for research interest about stability of photoanodes, as shown in Figure 1.4 b) shows an increase as well, but at a slower rate.

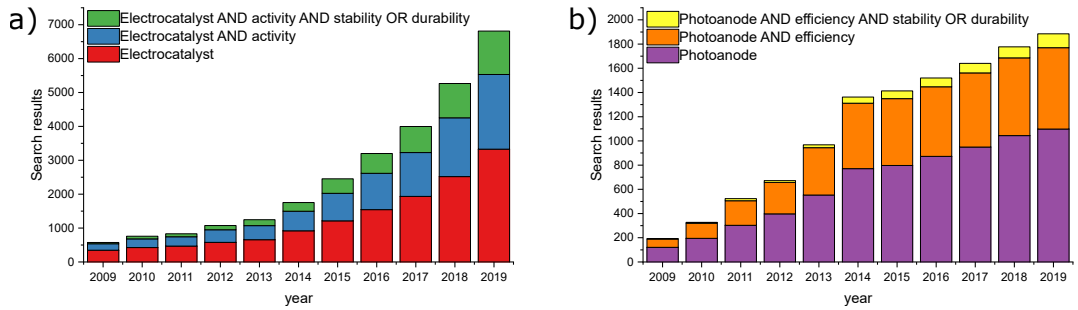

Figure 1.4: Comparison of research interest in electrocatalyst stability and photoelectrocatalyst stability, measured in scopus search results. ***a)*** *Scopus search results of boolean operator connected search terms Electrocatalyst, Electrocatalst AND activity, and Electrocatalyst AND activity AND stability OR durability.* ***b)*** *Scopus search results of boolean operator connected search terms Photoanode, Photoanode AND activity, and Photoanode AND activity AND stability OR durability*

This work aims at deepening the understanding of degradation mechanisms in both electrochemical and photoelectrochemical systems. In the field of PEMWE, a newly developed membrane electrode assembly (MEA) setup developed and operated in collaboration with ZAE Garching is used to determine the dissolution of OER catalysts in systems, which resemble electrolyzers on the industrial level. These results are supported by detailed parameter studies on the origin of the differences between the MEA system and the aqueous model system (AMS), performed in the AMS.
In the field of photoelectrochemistry, the aim of this work is a transfer of the techniques and knowledge, which was gathered within the previous decade towards photoelectrochemical systems. Thus, the scanning flow cell coupled to an inductively coupled plasma mass spectrometer (SFC-ICP-MS), which has been successfully used to determine the stability of electrocatalysts and their degradation mechanisms, is modified to allow stability determination of photoelectrodes. For this purpose, a UV-light source with power calibration is introduced to the cell. This newly developed system is used for three studies on WO_3, currently highly considered as photoanode, as a model system:

1. A proof of concept in which photocorrosion of WO_3 is studied. This study aims at establishing simple relations between applied potential, incident light and electrode dissolution.
2. A study, which observes the effect of different electrolytes on the photostability of WO_3. This study aims to determine the degradation kinetics of photoanodes in different electrolytes.
3. A model study on the effect of iridium as co-catalyst on the stability of WO_3 photoanodes. In this study the common mitigation strategy to overcome limited stability of WO_3 photoanodes is tested utilizing the novel system.

The choice of iridium as co-catalyst in the third case study is also aimed at looking at the bigger picture. As described before, iridium is a scarce noble metal. Thus, the utilization of iridium should be emphasized in areas with the largest return of investment. A comparison of iridium in electrochemical and photoelectrochemical systems with the recently introduced S-number metric will be used to answer this question.

2 Theory

This chapter covers the theoretical background information needed to understand the scientific contribution made in this work. If not stated differently, the information was taken from the electrochemical [44–47] and photoelectrochemical [48] base literature.

2.1 Thermodynamics of electrochemical water splitting

A view on thermodynamical equilibrium potentials of the electrochemical water splitting reaction is required to evaluate the energy consumption and get a hold of efficiency. Thermodynamically every electrochemical reaction in an electrochemical half-cell has an equilibrium potential $E^0(\mathrm{Ox/Red})$ of the oxidated and reduced states at given conditions. A given equilibrium potential can not be viewed separately but only compared to a known half-cell equilibrium potential.
Electrochemical water splitting refers to the reaction

$$2\,H_2O \quad \longrightarrow \quad 2\,H_2 + O_2 \tag{2.1}$$

This RedOx reaction can take place in acidic and basic conditions. The acid balanced half-cell reactions are

$$2\,H_2O \quad \longrightarrow O_2 + 4\,H^+ + 4\,e^- \quad \text{(Anode)} \tag{2.2}$$
$$2\,H^+ + 2\,e^- \quad \longrightarrow H_2 \quad \text{(Cathode)} \tag{2.3}$$

Thus, water is oxidized at the anode side. The emerging protons are transported to the cathode side to be reduced on the cathode side. In a basic system, the half cell reactions are

$$4\,OH^- \quad \longrightarrow O_2 + 2\,H_2O + 4\,e^- \quad \text{(Anode)} \tag{2.4}$$
$$4\,H_2O + 4\,e^- \quad \longrightarrow 2\,H_2 + 4\,OH^- \quad \text{(Cathode)} \tag{2.5}$$

The RedOx couple $E^0(H^+/H_2)$ at standard conditions (pH = 0) is defined as

standard hydrogen electrode (SHE) with an electrode potential of $E^0(H^+/H_2) = 0\,V$. At pH values diverging from standard conditions, the same RedOx couple is used as reference electrode and named reversible hydrogen electrode (RHE). The relation between RHE and SHE is given by the Nernst-equation

$$E(H^+/H_2) = E^0(H^+/H_2) + \frac{RT}{zF}\ln\left(\frac{a_{Ox}}{a_{Red}}\right) = -\frac{RT}{zF}\cdot \mathrm{pH} \tag{2.6}$$

F is the Faradaic constant, z the number of transferred electrons in the reaction, and a_{Ox}/a_{Red} the respective activities of oxidated/reduced species in the electrolyte. Electrode potentials with respect to the SHE or RHE are denoted by V_{SHE} or V_{RHE}. The electrode potential of an electrochemical cell at standard conditions can be calculated with

$$E^0 = \frac{\Delta G^0}{zF} \tag{2.7}$$

The Gibbs free energy ΔG^0 is defined as the difference between the free enthalpy ΔH and the product of the temperature T with the entropy ΔS^0.

$$\Delta G^0 = \Delta H^0 - T\Delta S^0 \tag{2.8}$$

Using literature values for enthalpy and entropy changes [49], the standard potential $E^0(O_2/H_2O)$ of the water oxygen half-cell can be calculated

$$E^0(O_2/H_2O) = \frac{\Delta H^0 - T\Delta S^0}{zF} = 1.23\,V \tag{2.9}$$

As the half-cell potential of the cathode reaction is 0 V by definition, thermodynamically, a cell potential of at least 1.23 V is necessary for electrochemical water splitting.

2.2 Reaction kinetics of the gas evolution half cell reactions

Thermodynamical considerations are always calculated for equilibrium values. In an overpotential is applied and leads to gas evolution, this equilibrium is disturbed [50]. Thus, in a scenario in which gas evolution reactions take place, kinetic considerations have to be taken into account. For a half cell reaction, the current density j for a given RedOx couple is given by the Butler-Volmer equation.

$$j = j_0 \cdot \left\{\exp\left[\frac{\alpha_a zF}{RT}(\eta)\right] - \exp\left[-\frac{\alpha_c zF}{RT}(\eta)\right]\right\} \tag{2.10}$$

j_0 denotes the exchange current density, an intrinsic material factor of the electrode, to which not only catalytic activity but physical parameters contribute. The overpotential $\eta = E - E_{eq}$ is the difference between the actual potential of the system and its equilibrium potential. The dimensionless anodic and cathodic charge transfer coefficients α_a and α_c are defined as [51, 52]

$$\alpha_a = \left(\frac{RT}{F}\right)\left(\frac{\mathrm{d}\ln(j_a)}{\mathrm{d}E}\right) \tag{2.11}$$

$$\alpha_c = \left(\frac{RT}{F}\right)\left(\frac{\mathrm{d}\ln(j_c)}{\mathrm{d}E}\right) \tag{2.12}$$

The charge transfer coefficients depend on the rate-determining step of the reaction and are determined experimentally.
A comparison of the overpotentials η of the individual half-cell reactions, OER and hydrogen evolution reaction (HER) shows that the OER is the less efficient reaction. As depicted schematically in Figure 2.1, its kinetic overpotential is significantly larger than the overpotential of the HER. A much higher overpotential η is needed to drive the reaction in the OER half-cell than in the HER half-cell. The reasons

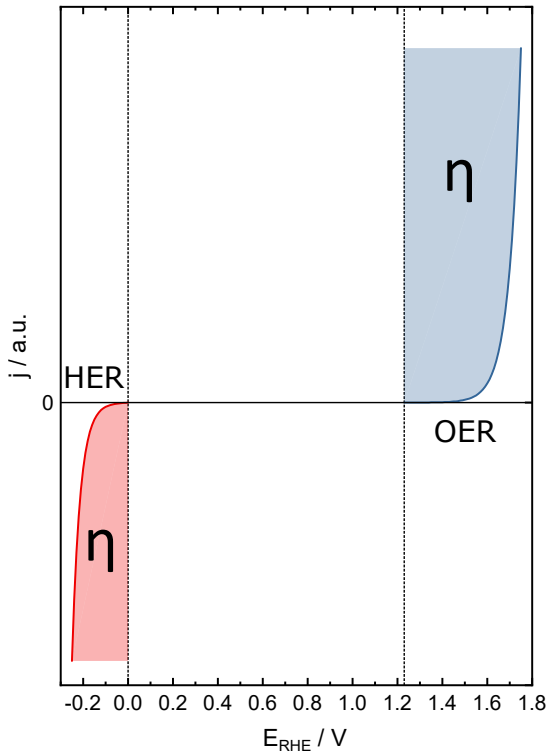

Figure 2.1: Schematic display of the overpotentials required for currents in the OER and HER from the Butler-Volmer equation. *The regions η mark the overpotentials of the HER and OER.*

for this different kinetic behavior lie in the nature of the reaction. While for the formation of H_2 in the HER, only $2\,e^-$ have to be transferred, the OER is a $4\,e^-$ reaction. As the transfer of more than one e^- at the same time is highly improbable, all proposed OER reaction mechanisms from the early works of Bockris to current

microkinetic modeling are based on four individual charge transfer steps [51, 53–56].

For OER to take place, the free Energy ΔG has to decrease for every step of the reaction at a given potential. This is exemplified in Figure 2.2 for the mechanism calculated by Rossmeisl et al. on a RuO_2 surface.

$$2\,H_2O \tag{2.13}$$
$$\longleftrightarrow \quad HO^* + H_2O + H^+ + e^- \tag{2.14}$$
$$\longleftrightarrow \quad O^* + H_2O + 2\,H^+ + 2\,e^- \tag{2.15}$$
$$\longleftrightarrow \quad HOO^* + 3\,H^+ + 3\,e^- \tag{2.16}$$
$$\longleftrightarrow \quad O_2 + 4\,H^+ + 4\,e^- \tag{2.17}$$

At a potential of $E = 0\,\mathrm{V}$, all the reaction steps show a positive ΔG. Thus,

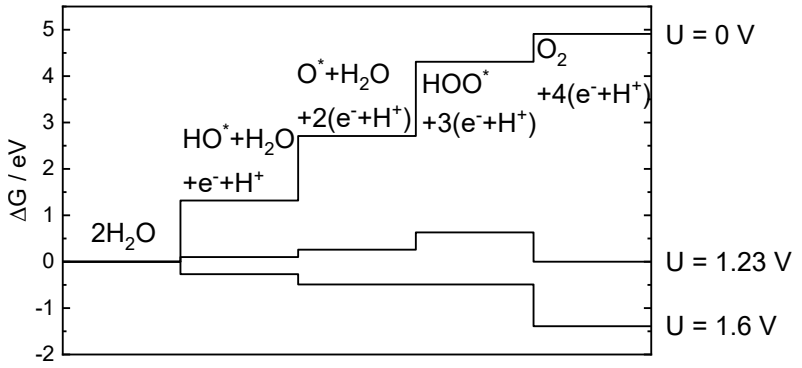

Figure 2.2: ***ΔG of all steps of the proposed OER reaction mechanism on a RuO_2 surface for three different potentials.*** *Adapted from [57].*

the thermodynamically favorable reaction is the oxygen reduction reaction (ORR), the counter-reaction of the OER. At $E = 1.23\,\mathrm{V}$, the thermodynamic equilibrium potential of the (H_2O/O_2) couple, the free energy curve is flattened out. However, only the last step, the detachment of the O_2 molecule from the catalyst surface, goes along with a negative free energy change. Thus, the reaction does not take place, although it would be thermodynamically possible. Only at a potential of $E = 1.60\,\mathrm{V}$, all steps of the proposed reaction mechanism exhibit a negative free energy change and the reaction is thermodynamically and kinetically favorable.
As shown before, the free energy differences for each intermediate step vary. Furthermore, each anode material has different binding affinities for the individual intermediates. Thus, the OER activities - currents produced at a fixed potential - vary as well [58].

2.3 Photoelectrochemical water splitting

The idea of photoelectrochemical water splitting is to directly drive the water splitting reaction with the energy provided by the sunlight. For this purpose, semiconducting photoelectrodes are immersed in liquid electrolytes. A semiconductor has two energy levels to consider. The valence band (VB) is the ground state energy level of electrons in the semiconductor. These electrons can be excited thermally or optically and move to the conduction band (CB). The energy difference between VB and CB is called the bandgap with the energy E_G. Before a semiconductor is brought in contact with an electrolyte, containing an equilibrium between oxidized (Ox) and reduced (Red) states, both have their own Fermi energy levels E_F, as sketched in Figure 2.3 a). When both are brought into contact, electrons are exchanged between the semiconductor and the electrolyte until their respective Fermi energy levels align. As displayed in Figure 2.3 b), this alignment of the Fermi energy levels causes the VB and CB of the semiconductor to bend at the semiconductor/electrolyte interface.

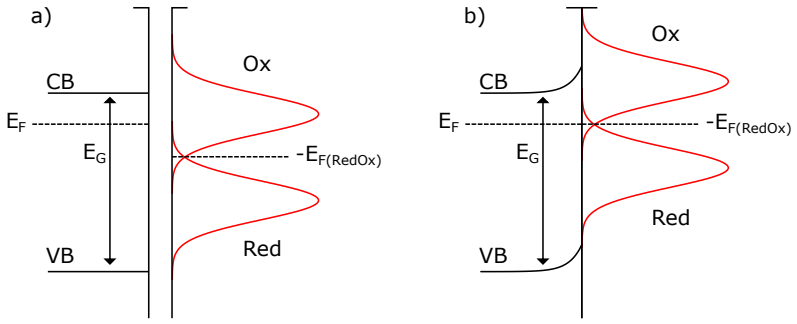

Figure 2.3: Schematic display of the band bending in an n-type semiconductor in contact with an electrolyte. ***a)*** *Semiconductor (left) with its valence band (VB), conduction band (CB), bandgap (E_G)), and the resulting Fermi energy level (E_F) separated from the electrolyte with its oxidated and reduced species and the resulting Fermi energy level.* ***b)*** *Semiconductor in contact with the electrolyte. The semiconductor transfers electrons to the solution, and the Fermi energy levels align. The depletion of electrons leads to a bending of the VB and CB. Adapted from [59].*

If an electron (e^-) in the valence band of the semiconductor is excited by a photon with an energy of $E_\lambda > E_G$, an e^- is excited from the VB to the CB and leaves a hole (h^+) in the VB. An e^- in the excited state can reduce an oxidized state, such as H^+, and an h^+ in the VB can oxidize a reduced state, such as H_2O. The requirement for a semiconductor to perform water oxidation and reduction reactions are the right bandgaps and band positions.
A semiconductor that has a bandgap of $1.23\,V + \eta$ is only able of overall water splitting if the Fermi energy levels of VB and CB have suitable Fermi energy levels. As sketched in Figure 2.4 a), the VB edge has to be located well below the thermodynamic water oxidation potential and the CB has to be located above the thermodynamic water reduction potential (note: in photoelectrochemical literature, potentials

are displayed from positive to negative, as this corresponds to a display of Fermi energy levels from negative to positive).

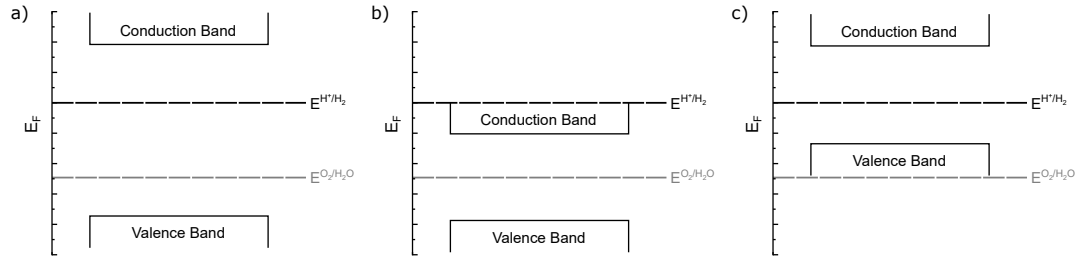

Figure 2.4: Schematic display of the effects of different VB and CB energy levels on the water-splitting capabilities of a photoelectrode. ***a)*** *The VB lies below the thermodynamic water oxidation potential, and the CB lies above the thermodynamic water reduction potential. This photoelectrode is capable of overall water splitting.* ***b)*** *The VB lies below the thermodynamic water oxidation potential, and the CB lies below the thermodynamic water reduction potential. This photoelectrode can oxidize water.* ***c)*** *The VB lies above the thermodynamic water oxidation potential, and the CB lies above the thermodynamic water reduction potential. This photoelectrode can reduce water.*

However, materials with bandgaps large enough to perform overall photoelectrochemical water splitting have the disadvantage of a low quantum yield. The fraction of the solar spectrum that is utilized for water splitting decreases. Thus, semiconductors with different bandgaps and band edges are coupled to reach higher quantum yields. Semiconductors with a VB edge below the thermodynamic water splitting potential and a CB edge below the water reduction potential, as shown in Figure 2.4 b), can oxidize water. However, the HER with the electrons in the CB is thermodynamically unfavorable. Similar in the opposite case, as displayed in Figure 2.4 c). The VB edge is situated above the thermodynamic OER potential, and the CB edge is situated above the HER potential. This semiconductor can perform HER but not OER. For a working device, this problem would be solved by choosing two semiconductors. One to perform OER, and one to perform HER. When both are connected the electrons from the semiconductor with lower band edges can move after excitation from the CB to the VB of the other semiconductor. If the semiconductor is connected to a counter electrode and a potentiostat, current-potential curves similar to electrocatalysis can be recorded under illumination. These current-potential curves deviate strongly from those of a classical electrocatalyst, as shown in the last section. As only excited states can participate in the reaction at the semiconductor/electrolyte interface, the current-potential function does not follow the Butler-Volmer equation. Instead, the intensity of incident photons of a suitable wavelength for excitation determines the limiting photocurrents. Thus, a typical current-potential curve, as shown in Figure 2.5, looks in the onset like an electrochemical onset, but as a turning point with an asymptotic behavior at higher potentials.

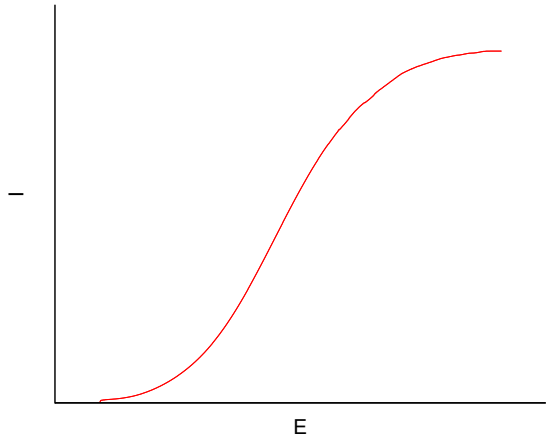

Figure 2.5: Schematic drawing of the current-potential curve of a semiconductor for photoelectrochemical application under illumination. *After an onset similar to onsets in a classical electrochemical system, the currents reach a limiting photocurrent, governed by the intensity of incident light.*

2.4 Basics of corrosion science

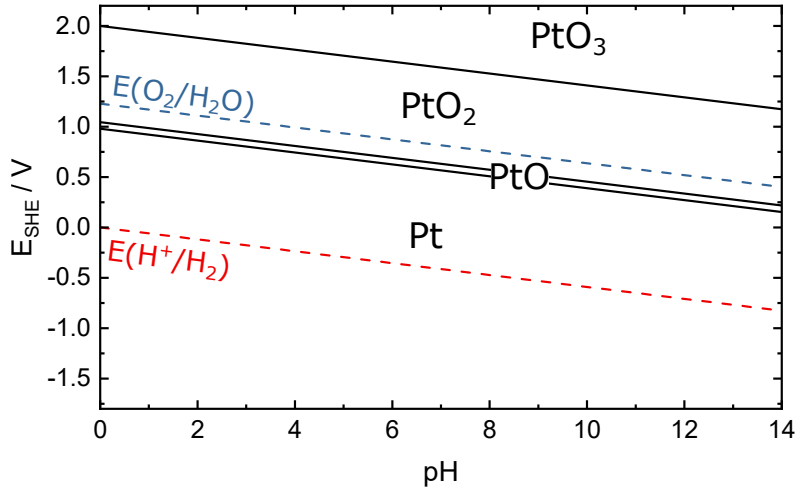

Figure 2.6: Simplified Pourbaix diagram of Pt. *Solid lines denote transitions between solid phases. The thermodynamic potentials of the H^+/H_2 couple and the H_2O/O_2 couples as a function of pH are shown as dashed red ad blue lines. Adapted from [60].*

The fundamentals of corrosion science were laid at the end of the 18th century. The elements have been sorted in the galvanic series according to the electrochemical potential at standard conditions E^0. If two half cells of the series are brought in contact with each other, the element with the higher standard potential reduces and the element with the lower standard potential is oxidized, leading to precipitation of the reduced material and dissolution of the oxidized material until the standard potential equilibrate according to the Nernst-equation (equation 2.6).
A more detailed concept of the changes of oxidation states of materials dependent on the electrochemical potential of the half-cell and the pH value in the solution was published by Marcel Pourbaix in 1966 [60]. In the Atlas of Electrochemical Equilibria in Aqueous Solutions, all electrochemical transitions of materials known

at that time were collected. From the equations in Marcel Pourbaix's work, the Pourbaix diagrams with pH on the x-axis and electrochemical potential against the SHE on the y-axis can be constructed [60].
Pt, a noble metal, displays an example of an easily accessible Pourbaix-diagram. It oxidizes to PtO around $1\,V_{RHE}$ and subsequently to PtO_2. A simplified Pourbaix diagram including the transitions is shown in Figure 2.6.
While Pourbaix concept works, as the title of his book suggests, well for equilibrated systems with H_2O, H^+, OH^-, and without electrolyte ions, dynamic potentials or oxidizing and reducing agents in the electrolyte call for a more precise theory. These effects can be described by mixed potential theory [47]. According to mixed potential theory, the electrode potential is always a combination of all half cell reactions, present on the surface. The open circuit potential (OCP) of the system is hereby determined by plotting the Tafel analysis of both reactions. The intersection is the potential, as cathodic and anodic currents equilibrate. A diagram constructed this way is called Evans diagram. If the emerging potential from the distinct potentials displays an overpotential for one of the half-cells and a current flows between them, corrosion occurs from the half-cell current.
Similar, corrosion phenomena can occur when an overpotential is applied to the electrode. If this induces an oxidative or reductive transition in the electrode material, this subjects the electrode to currents, which induce corrosion. For example, if Pt oxidizes, Oxygen is included in the lattice and released when Pt is reduced. These structural changes lead to dissolution of parts of the top surface layer. This phenomenon is known as transient dissolution [61].

3 Current State of Research

This chapter describes the current state of the research necessary to understand the experimental work, shown in the subsequent chapters of this thesis. First, the working principle of PEMWE is introduced, and especially the previous works about anode catalysts are discussed. Second, the current state of research in Photoelectrochemistry, especially the stability of photoelectrode catalysts, is discussed.

3.1 Proton Exchange Membrane Water Electrolyzers

PEMWE is considered the upcoming state-of-the-art-technology for electrochemical hydrogen production [33, 37, 62]. It facilitates the acidic water-splitting reactions, shown in equations 2.2 and 2.3, with high efficiencies at high power densities. With a low ohmic resistance in all components, they are well suited for dynamic operation.
PEMWE is based on MEA technology. Proton transport from the anode side, where the OER takes place, to the cathode side, where the HER takes place, is facilitated through a PEM in these devices. The porous electrodes, the anode, and the cathode are on opposite sides of the membrane. Each electrode is contacted by a porous transport layer (PTL) which is electronically conductive and serves as transport layer for water as the reactant and gaseous products. Furthermore, it is a conductor, facilitating charge transport through the bipolar plates and the power source.
A schematic drawing of an MEA is shown in figure 3.1.

The water as reactant is introduced through an inlet at the anode side. Here the OER takes place, and H_2O is split into O_2, H^+, and e^- in the anode catalyst layer. The reaction products leave the reaction site through different pathways. O_2 is solved in the water and transported away from the reaction site through the anode water feed. H^+, on the other hand, is transported through the PEM.
The PEM, currently usually made from Nafion®, was developed by DuPont. It consists of a fluorinated carbon polymer backbone with attached sulfonic acid groups. [63]. Protons, generated in the water oxidation reaction, attach to the acidic groups and are transported through the membrane by the potential of the electric field to the cathode side, where the HER takes place. On the way to the cathode catalyst layer, every proton drags 3 to 4 H_2O molecules with it through electroosmotic drag [64, 65]. The H_2 molecules formed in the HER reaction leave

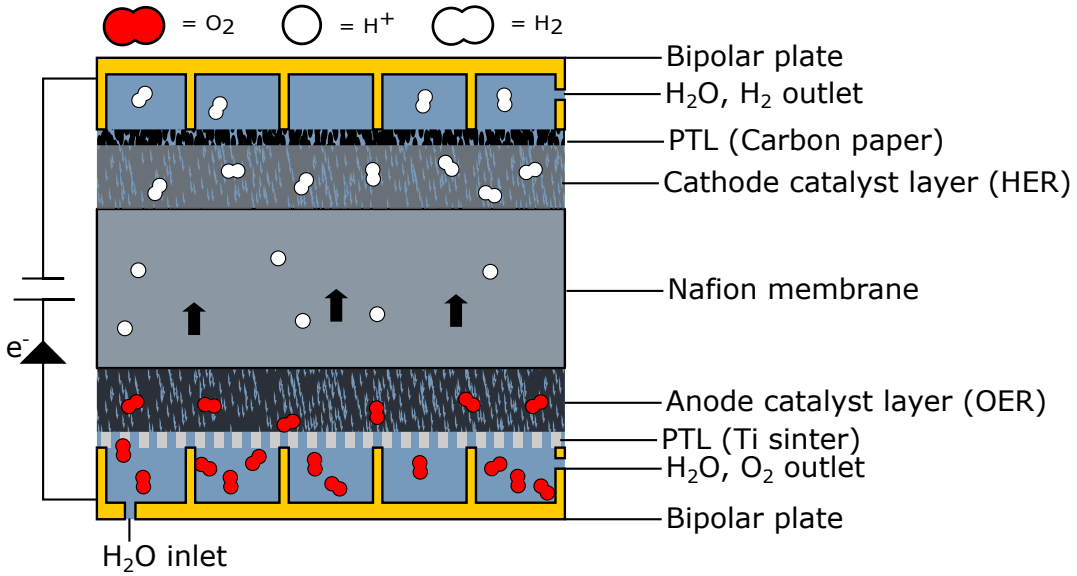

Figure 3.1: Schematic drawing of an MEA as used in PEMWE

the system at the cathode outlet.
According to the literature, the Nafion® membrane is highly acidic [33, 66, 67]. Furthermore, the local pH at the anode side is lowered by protons generated in the OER. Thus, catalytic materials and components should withstand low pH and high oxidative potentials at the anode side.
The bipolar plates serve two functions: electronic conduction and transport of deionized (DI) water, the reactant, through serpentine channels as flow field. They are usually made of titanium, which has the advantage that it does not dissolve upon corrosion at high potentials but instead forms a thin, passivating layer of TiO_2 [60]. The bipolar plates connect to the PTL. These layers, usually made from corrosion-resistant Ti sinter plates at the anode side and carbon paper at the cathode side, enable electric contact to the respective catalyst layers. Furthermore, their porosity allows water to diffuse to the catalyst layers. In some cases, they are coated with corrosion resistant noble metals, such as Au or Pt, to hinder passivation on the surface of the PTL and reduce the contact resistance between PTL and anode catalyst layer.

3.1.1 Aqueous Model Systems

PEMWE is a complex system with several interdependencies between single components. Performance relies not only on the utilization of the catalyst but contact resistances between the catalyst layer and PTL or PTL and bipolar plates as well. The anode and cathode catalyst layers can not be studied individually but only as a full cell. Thus, it is hard to single out the effect of a newly developed catalyst on

MEA performance. Furthermore, the fabrication of MEAs requires high amounts of catalysts, which might be cost-intensive or complex to fabricate in these amounts. Therefore, model systems based on aqueous electrolytes are commonly employed for initial research on newly developed catalysts. These AMS are based on diluted strong acids, such as H_2SO_4 or $HClO_4$ [68–73]. They are classical electrochemical three-electrode cells, as depicted in figure 3.2 [44]. Catalyst studies in AMS are

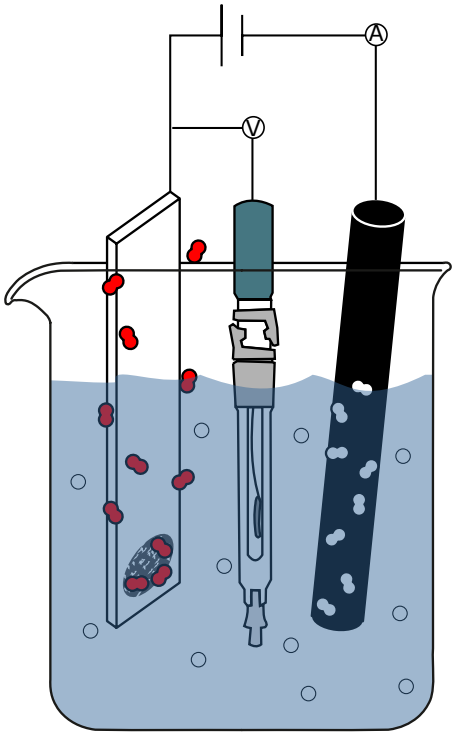

Figure 3.2: Schematic drawing of a three-electrode AMS as used in acidic water splitting research.

carried out by dispersing the catalyst powder in H_2O or isopropyl alcohol (IPA) and dropcast the resulting ink to a rotating disc electrode (RDE) electrode. In some cases, Nafion® is added to the ink to serve as a binder in the resulting catalyst layer. To evaluate the activity of catalysts, current-potential profiles are recorded and analyzed. These experiments in AMS provide similar information on achievable gravimetric current densities of catalysts, as observed in full-cell experiments [74]. Furthermore, catalyst stability is determined in AMS. The simplest way to perform stability measurements in AMS are chronopotentiometric measurements. The catalyst is operated at constant current density, and the resulting potential curve is recorded. After extended continuous operation, the potential jumps to a higher value. At this point, the catalyst is considered to be fully degraded [68, 69].
However, this method is unreliable as backing electrode materials and their contact with the electrocatalyst might influence the results [75]. Later on, more sophisticated methods to determine catalyst stability have arisen. Not only were dissolution products in liquid aliquots taken during the measurements and analyzed but post-analysis of catalyst layers was performed [75–77]. Furthermore, *in-situ* methods, as the electrochemical quartz crystal microbalance (EQCM) [78] and the SFC-ICP-MS were developed to connect catalyst degradation to electrochemical operation

in real-time.

3.1.2 The anode catalyst layer

The catalyst layers are made of porous, nanostructured electrocatalysts, with Nafion® as binder. Due to the acidic nature of the Nafion® membrane, only a few materials are stable enough in the conditions of the PEM electrolyzer. On the cathode side, where the catalysts are subjected to reductive potentials, high surface area Pt/C is the state-of-the-art electrocatalyst [33, 79]. As Pt is highly dispersed on C, and corrosion can be prevented, low Pt loadings are sufficient for achieving high current densities of PEMWE.
On the other hand, at the anode side highly oxidative potentials are required to drive the OER. According to thermodynamical calculations and experimental data, only a few materials are catalytically active towards the OER and thermodynamically stable in acidic oxidative conditions [60]. The material with the highest activity towards OER is Ru [58, 80]. However, limited stability of Ru-based electrodes is limiting their applicability in industrial PEMWE. Fundamental studies [81–84], and tests on the industrial scale PEMWE [85] show severe degradation of Ru-based electrodes. Although many research efforts are put into developing mitigation strategies [86], there has been no demonstration of a durable electrolyzer based on Ru-based electrocatalysts so far.
The state-of-the-art material used as electrocatalyst on the anode side of PEMWE is iridium. It is slightly less catalytically active towards the OER than Ru but shows significantly enhanced operational stability. In the anode catalyst layer of state-of-the-art PEMWE, iridium is employed in loadings as high as $2\,\mathrm{mg_{Ir}\,cm^{-2}}$. The high catalyst loadings on the anode side are problematic for upscaling of PEMWE to the GW scale. As iridium is the noble metal with the lowest annual production yields [87, 88], it is expected that catalyst costs, although not a significant cost factor currently [89], will be a large cost driver upon PEMWE upscaling, as the demand is expected to exceed production [62, 90, 91]. Thus, for more efficient utilization of iridium, significant research efforts are focused on maximizing the utilization of iridium by increasing the gravimetric activity of iridium-based electrocatalysts [92]. Research Projects like the german funded Kopernikus P2X [26] or the European funded EnergyX [24] aim to significantly decrease the anode catalyst loading.
Progress towards this target has been made by synthesizing highly active perovskites [93–98], multimetallic materials [86, 99–101], or dispersing iridium on high surface supports [74, 91, 102–105]. However, in industrial application, activity alone as a descriptor is insufficient. As PEMWEs are supposed to operate for several years, catalyst stability as a second descriptor must be considered.

Properties and Stability of OER electrocatalysts

The component in all state of the art OER electrocatalysts, which is active towards OER is iridium. It can withstand the harsh oxidative conditions present on the anode of a water electrolyzer. To get a first impression about the stability of iridium OER operating conditions, it is helpful to look at the Pourbaix diagram of iridium [60], which is shown in a simplified version in figure 3.3.

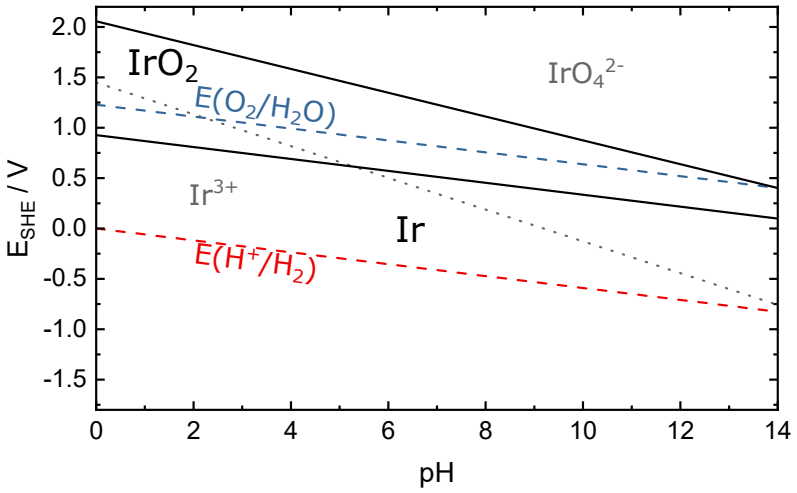

Figure 3.3: Simplified Pourbaix diagram of Ir. *Transitions between solid species are denoted by solid lines. Transitions between species in aqueous solution are denoted by grey dotted lines. The Thermodynamic potentials of the H^+/H_2 couple and the H_2O/O_2 couples as function of pH are shown as dashed red ad blue lines. Adapted from [60].*

Above a potential of $0.926\,V_{RHE}$, Ir is present in its oxidized form, IrO_2. Thus, it is the dominant form during OER electrocatalysis. If iridium is, at estimated operating pH 1 of a water electrolyzer anode, subjected to potentials above $1.8\,V_{RHE}$, it oxidizes to $IrO_4{}^{2-}$, an ionic species, which disperses into the aqueous medium. Furthermore, above $1.8\,V_{RHE}$, gaseous IrO_3, which is an intermediate in the reaction towards $IrO_4{}^{-}$, was detected as a side product to the OER [106]. Thus, the threshold of $1.8\,V_{RHE}$ should not be exceeded to avoid degradation.
The display in the Pourbaix diagram, however, is insufficient. Oxidized iridium can exist in two different forms: the hydrous form (IrO_x), which has an amorphous structure, and the rutile form (IrO_2) [107, 108]. Hydrous iridium oxide is the predominant form if iridium is oxidized electrochemically [70, 109, 110]. If potential cycling is performed on an iridium electrode, around the iridium oxidation threshold of $0.926\,V_{RHE}$, one monolayer of hydrous iridium oxide forms for each cycle [70, 110]. If long-term electrochemical OER is performed on a metallic iridium electrode, it might transition to the rutile form [76]. The other method to oxidize iridium is thermal annealing. At low annealing temperatures of around 300 °C, the formed oxide is amorphous. With increasing temperatures, the formed oxide exhibits a more crystalline structure [111, 112].

Amorphous iridium oxide is a highly active electrocatalyst towards OER [70, 110]. However, the stability of materials based on amorphous iridium oxides is limited [38, 110, 112]. With increasing crystallinity, the activity of iridium oxide decreases while stability increases [111, 112].
This change in material properties between iridium oxides of different crystallinity can be explained by different OER reaction mechanisms taking place on the different materials [38, 113]. In amorphous iridium oxides, a lattice participation mechanism is the predominant OER mechanism. In this reaction mechanism, the water molecules adsorb to the oxygen atoms in the iridium oxide lattice. Thus, the lattice oxygen atoms can participate in the OER and leave the lattice in the form of O_2 molecules, leading to destabilization of the lattice and iridium dissolution. Thermodynamically, this lattice OER mechanism is not possible without catalyst dissolution [50].
Rutile IrO_2, on the other hand, catalyzes the OER predominantly over an adsorbate evolution mechanism. In this mechanism, the water molecules and reaction intermediates adsorb to the iridium atoms in the lattice. As no lattice oxygen is involved in this reaction, the probability of iridium escaping the lattice is much lower than in the lattice participation mechanism.
Thus, anode catalysts for electrochemical water splitting applications diverge vastly in activity and stability. This hinders valid comparisons between different catalysts, as stable catalysts might be less active than unstable catalysts. One of the most essential catalyst descriptors for economical industrial application is the amount of oxygen a catalyst can produce before it fully degrades. A recently introduced concept, the stability number (S-number), simplifies such comparisons [38].

The S-number The S-number is the fraction of the amount of produced O_2 molecules divided by the amount of dissolved catalyst atoms.

$$\text{S-number} = \frac{n(O_2)}{n(\text{Ir})} \tag{3.1}$$

As the amount of produced oxygen molecules is a descriptor that is hard to measure, the transferred charge during the reaction is used as a proxy. With an estimated Faradaic efficiency of 100 % towards OER, the amount of oxygen evolved is calculated with the Faraday equation.

$$n(O_2) = \frac{Q}{zF} \tag{3.2}$$

Q is the transferred charge, z is the number of transferred electrons in the reaction, and F is the the Faradaic constant. The S-number is calculated by dividing the amount of oxygen evolved by the amount of iridium dissolved.
The amount of dissolved iridium can be determined by real-time measurements with mass-spectrometers coupled to electrochemical application, as shown in section

4.1.1.
S-numbers of iridium-based catalysts appear to be an intrinsic material property of OER electrocatalysts with the same lattice structure. Only minor differences appeared with different sample preparation methods, powdered and solid samples, and different electrochemical testing protocols [38]. In the original study, metallic iridium reveals S-numbers around 10^3, hydrous iridium oxide (IrO_x) reveals S-numbers between 10^4 to 10^5 and crystalline iridium oxide (IrO_2) reveals S-numbers around 10^7. The discrepancy in stability of different iridium oxides can be explained by the different reaction mechanisms, as mentioned above.
However, all of these results regarding the stability of OER electrocatalysts have in common that they were obtained in AMS. In MEA, on the other hand, the catalyst lifetimes exceed those estimated from AMS measurements by far. Thus, it has been part of the scientific discussion for a while if AMS measurements are representative of the conditions present in MEA [38, 75, 114–117]. With end-of-life (EOL) data of an electrolyzer with a Ru anode and stability measurements of a Ru-based catalyst in the SFC-ICP-MS [38, 85], the stability discrepancy between both systems was estimated to be several orders of magnitude.
As water electrolyzers are more complex systems than AMS, and system failure might originate somewhere besides the catalyst layer, catalyst dissolution measurements in MEA systems would help improve the understanding of water electrolyzer degradation. However, such direct measurement of catalyst dissolution in MEA devices appears to be complicated. Babic et al. determined the iridium concentration in the water circulation of an MEA from liquid samples [118]. However, the results were not reproducible and inconclusive. The iridium concentration in the anode water cycle decreased steadily in one measurement and stayed constant in another. The authors indicated that galvanic precipitation of dissolved iridium on the stainless steel tubes of the electrolyzer might be the reason for this behavior. Although in a system not fully comparable, similar results were shown by Regmi et al. in a regenerative fuel cell [119]. Thus, further efforts have to be undertaken to unravel the degradation mechanisms in PEM electrolyzers.

3.1.3 Alternatives to the PEM technology

While the acidic PEM electrolyzer is currently expected to offer the best compromise between operational costs, durability, and compatibility with the intermittency of renewable energy sources. However, it is important to discuss alternative technologies for the sake of completeness.

Alkaline electrolysis Alkaline electrolysis is a technology that has been used commercially for the last century. The first alkaline electrolyzers were aqueous systems consisting of electrodes immersed in a KOH bath [120]. While the alkaline environment allows for the use of abundant catalytic materials, such as Ni, Co, or

Fe. However, the use of aqueous, alkaline electrolyte produces high resistivity and low efficiency of alkaline electrolyzers.
Current developments in anion exchange membrane (AEM) technology try to overcome this problem by substituting the aqueous electrolyte with an OH^- conducting membrane. Efficient AEMs that enable ion transport with low resistivity in an alkaline environment would make alkaline electrolysis the easier upscalable technology, as no scarce noble metals are part of the system [121–123]. Furthermore, it is expected that electrolyzers based on AEM might be able to use non-purified water as the reactant, eliminating the need for the water purification step before the electrolysis process [124]. Thus, alkaline electrolysis is a technology that has to be considered in the future, although it is on a lower technology readiness level than PEM water electrolysis.

Bipolar electrolysis Bipolar systems are supposed to feature the best of two worlds, PEM and AEM water electrolysis. In these systems, both kinds of membranes are used, an AEM for the anode side and an PEM for the cathode side [125–127]. They allow the combination of highly active Pt catalysts at the cathode side, which are unsurpassed by abundant materials, with the superior stability of Ni based OER electrocatalysts in alkaline milieu. Furthermore, the thermodynamic activation energy of these systems is lowered, as the thermodynamic potential of the anode side reaction, which takes place in alkaline, is lowered substantially according to equation 2.9. Thus, the water-splitting process is, in these systems, expected to be catalyzed by the pH difference in the AEM-PEM-junction [127].
However, although these systems show promising efficiencies in studies, it is still unclear if the pH-related effects take place as postulated [126]. Thus, a deeper understanding of these systems is required to determine their potential for future application.

Solid oxide electrolysis In solid oxide electrolyzers, the membrane is substituted by proton conducting ceramics that become conductive at high temperatures of $> 500\,°C$. According to equation 2.9, the enhanced temperature lowers the amount of electronic energy for water splitting [128].
However, the water-splitting process might be energetically favored in these systems, but a substantial amount of energy is needed to heat these electrolyzers to operational temperatures. Therefore, utilization is only favorable over PEMWE in processes where much excess heat is produced as a side product. Thus, solid oxide electrolyzers are a promising technique for the steel industry, where substantial amounts of hydrogen are needed, and heat is produced, but it is not applicable for large scale hydrogen production.

3.2 Photoelectrochemical Water Splitting

Successful photoelectrochemical water splitting was initially demonstrated by Akira Fujishima and Kenichi Honda in 1972 [129]. TiO_2 was irradiated with light of wavelengths below $\lambda = 415\,\mathrm{nm}$ resulting in the formation of oxygen and hydrogen from water. Since that early success, research has come a long way. The light source used in the first experiment, far too strong to resemble realistic conditions, was exchanged for the AM1.5G spectrum. The AM1.5G spectrum is light emitted by a Xe light source and shaped with a filter to resemble the radiation spectrum of the sun [130]. For the purpose of comparing results from different labs regarding photoactivity of photoelectrochemical materials, the intensity of these solar simulators is calibrated to $100\,\mathrm{mW\,cm^{-2}}$.
The first monolithic device (no wired contact) for photoelectrochemical water splitting was shown in 1998 [131]. In the last decade, tremendous advances have been made towards an application of a photoelectrochemical device. Solar to hydrogen efficiencies of up to 20 % for a monolithic device been reported recently [132]. Also, functional devices with up to $200\,\mathrm{cm^2}$ active area [133, 134] and efforts towards devices working with concentrated solar irradiance, allowing higher current densities [135], have been reported.
The advantage of photoelectrochemical water splitting over PEMWE is that no scarce noble metals are needed. Photoelectrodes consist of abundant transition metals or transition metal oxides [136]. For the photoanode, for example, materials with a large bandgap such as TiO_2, WO_3, Fe_2O_3, or $BiVO_4$ are considered [136]. However, in contrast to PEMWE, no commercial photoelectrochemical water splitting device has seen the light of day so far.
One of the most pressing but also most overlooked issues towards a commercial photoelectrochemical device is operational stability.

3.2.1 Photoelectrode stability in photoelectrochemical water splitting

Similar to PEMWE, stability would be one of the crucial points of a potential photoelectrochemical water splitting device. This issue was already present in the early stages of photoelectrochemical research. In 1984, Bruce Parkinson wrote *"Lifetime consideration must also be a factor in the realistic reporting of device efficiency."* [137]. In his work he asked, how stable a system has to be before an efficiency measurement would be justified. As many academics would not want to spend months, accelerated testing was proposed. However, another statement by Parkinson said, *"An exact criterion for stability has not been proposed, and I cannot offer any."* [137].
Since this work was published, almost 40 years have passed, and the understanding of degradation mechanisms has increased substantially. As mentioned in the introduction of this work, there has been increasing research interest in the stability

of photoelectrochemical device components. Besides degradation in other components of photoelectrochemical devices, semiconductor corrosion is one of the least understood degradation phenomena in photoelectrochemistry [138]. Works that include stability considerations for photoelectrocatalysts mainly rely on potentiostatic measurements without detailed analysis of the underlying degradation mechanisms [132, 133, 139–141]. While lifetimes of several 100 hours up to several weeks were demonstrated with these methods, the lifetimes of potential commercial devices should be similar to those of PEMWE. Thus, an understanding of the underlying degradation mechanisms would be helpful to design meaningful accelerated stress test (AST)s.

From a theoretical perspective, the considerations made towards the stability of photoelectrode are mostly thermodynamic. How this affects the assessment of photoanode stability will be elucidated on the example of WO_3, which is used as a model system for several studies in this work. WO_3 is a semiconductor that has been a candidate since the early days of photoelectrochemical research [142]. It is a yellow substrate with a bandgap of around 2.7 eV, which is in the visible spectrum. Also, its conduction band is slightly above $0\,V_{SHE}$ [143–145]. It can be easily synthesized by various means from peroxotungstic acid precursors, such as electrodeposition [146, 147], dip coating [148], spin coating [149], and inkjet printing of sol-gel derived WO_3 inks [150].

The Pourbaix diagram of W is shown in Figure 3.4. From a pure electrocatalytic

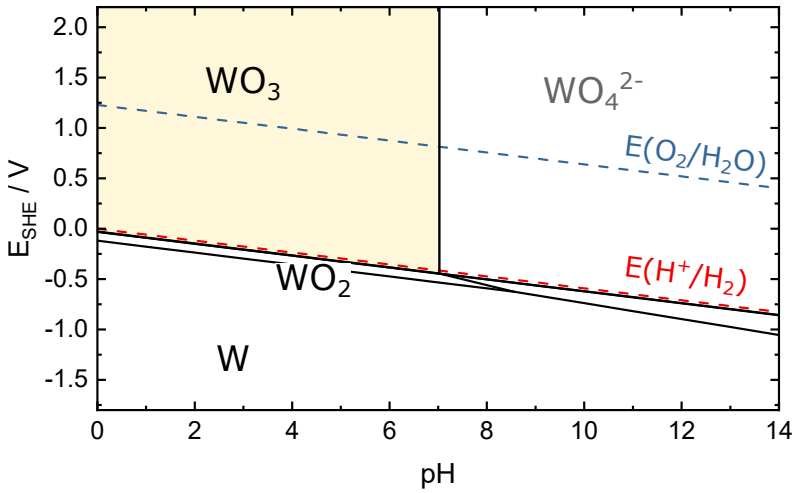

Figure 3.4: Simplified Pourbaix diagram of W. *The area of stability for WO_3 is highlighted in yellow. Liquid phases are denoted in grey. Adapted from [60].*

perspective, WO_3 should be stable in electrolytes with pH$<$ 4 at potentials above $0\,V_{SHE}$.

But WO_3 is not a conducting material but a semiconductor, where excited states are induced by photons. Thus, besides pH and potential, there are more degrees of freedom to consider. Figure 3.5 shows schematically the processes expected

in an n-type semiconductor in contact with an electrolyte that gets excited by a photon. In this drawing, besides VB and CB, the thermodynamic water oxidation and reduction potentials, E^{O_2/H_2O} and E^{H^+/H_2}, and the self-oxidation and self-reduction potentials of the semiconductor combined with the used electrolyte, E^{Ox} and E^{Red} are denoted [151]. The self-oxidation and self-reduction potentials are not intrinsic material propertis but always an interplay between the semiconductor and the used electrolyte. If an electron from the VB is excited by a photon, as shown in Figure 3.5 a), it leaves a hole in the VB. In general, there are two ways to relax to the ground state: water oxidation and electrode decomposition as depicted in Figure 3.5 b).

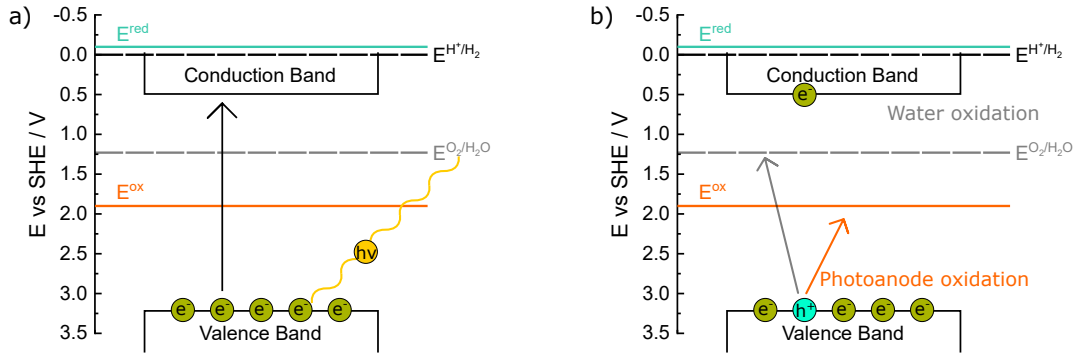

Figure 3.5: Schematic drawing of the processes occurring in an n-type semiconductor in contact with an electrolyte. ***a)*** *An incident photon excites an electron from the valence band to the conduction band.* ***b)*** *Two ways of annihilation for the excited hole are thermodynamically possible: water oxidation or photoanode oxidation.*

Thermodynamically, there are three different scenarios regarding the location of the energy levels in the semiconductor. In the first scenario, as depicted in Figure 3.6 a), the self-oxidation potential is located below the VB edge. Thus, an excited state can not oxidize the semiconductor, and the system is stable. In the second scenario, as depicted in Figure3.6 b), the self-oxidation potential is located between the VB edge and the thermodynamic water oxidation potential. Thermodynamically, water oxidation is more favorable than self-oxidation of the semiconductor. Thus, such systems are generally perceived as stable. In the third scenario, as depicted in Figure 3.6 c), the self-oxidation potential is located above the thermodynamic water oxidation potential. Such a semiconductor is thermodynamically unstable.

However, the situation in the second and third scenarios is not as clear as the thermodynamic view suggests. As recently brought into the discussion, kinetic considerations have to be taken into account [41]. According to these considerations, in scenarios two and three, a kinetic competition arises. Depending on kinetic limitations, both water oxidation and semiconductor self-oxidation are possible.

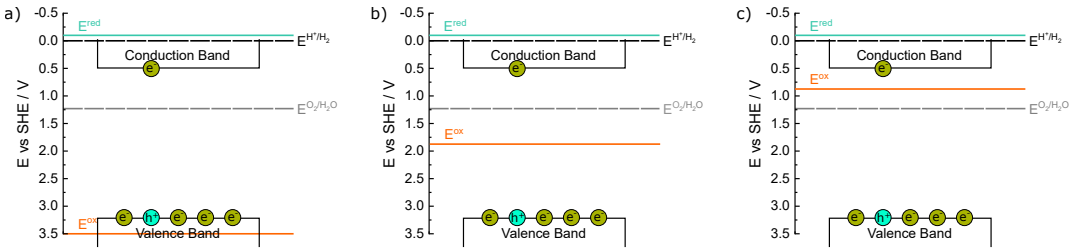

Figure 3.6: Schematic drawing of the reactions driven by an excited state in an n-type semiconductor. ***a)*** *The self-oxidation potential of the semiconductor is on a Fermi-level below the valence band Fermi-energy level. The semiconductor is thermodynamically stable.* ***b)*** *The self-oxidation potential of the semiconductor is on a Fermi-level between the Fermi-level of the valence band and the thermodynamic water oxidation potential. A kinetic competition between water splitting and self-oxidation is the result.* ***c)*** *The self-oxidation potential of the semiconductor is on a Fermi-level above the thermodynamic water oxidation potential. A kinetic competition between water splitting and self-oxidation is the result.*

4 Materials and Methods

4.1 Electrochemical Cells

In this section, the electrochemical cells used for the experiments, presented in this thesis are described in more detail. Electrochemical AMS, such as the scanning flow cell (SFC), are operated as three-electrode cells, while the MEA based cell is operated as a two-electrode cell.

4.1.1 Scanning Flow Cell

The electrochemical SFC is an electrochemical three-electrode cell with V-shaped channels designed for high-throughput electrochemical screening and product analysis. It was developed in the Max-Planck Institute for iron research and introduced in 2010 [152] and has since then continuously developed to serve multiple purposes. The first version of the SFC was coupled to an inductively coupled plasma mass spectrometer (ICP-MS) (see section 4.2) for elemental analysis of degradation mechanisms of electrocatalysts during electrochemical operation, such as platinum, gold, or non-noble metals [153–155].
Later on, it was optimized for gas evolution reactions [38, 75, 114], coupled with different analytics such as differential electrochemical mass spectrometry (DEMS) and differential analysis in real-time (DART) [156–160] to enable product analysis and also optimized for degradation studies in organic electrochemistry [161, 162] as well as battery materials [163].
In this work, two different types of SFCs are used. Chapter 5 features the gas evolution optimized SFC as introduced by Simon Geiger [38] and shown in figure 4.1 as part of the setup for studying OER catalysts. A novel version of the SFC, developed for monitoring activity and degradation of photoelectrocatalysts, is introduced in chapter 6.
A scheme of the SFC setup is shown in figure 4.1. Electrochemical measurements with the SFC are carried out with an electrolyte flow through the cell. The electrolyte is stored in a 50 ml polypropylene (PP) tube. It is transported by a peristaltic pump to a 15 ml PP tube, with four openings at the top, serving as a purge vial. The first opening allows the electrolyte to enter the purge vial. Through the second opening, the electrolyte is purged with various gases (5.0, Air Liquide). Overpressure can escape the purge vial through the third opening. The fourth opening is connected to the SFC with Tygon tubing. The electrolyte is dragged by a peristaltic

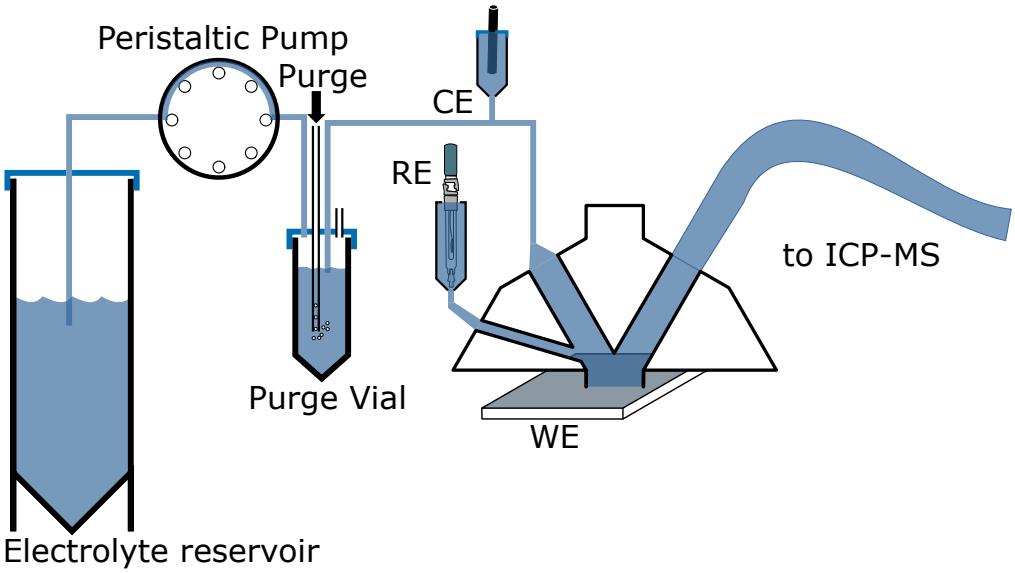

Figure 4.1: Schematic drawing of the SFC setup *The electrolyte is drawn from the reservoir by a peristaltic pump to the purge vial. The purge vial is put under overpressure with a gas of choice, mostly Ar. A second peristaltic pump draws the electrolyte from the purge vial through the cell. The counter electrode (CE) is placed with a T-connector in the flow from the purge vial to the SFC. The reference electrode (RE) is connected through an extra channel in the cell. Contact to the working electrode is made with the opening of the cell.*

pump through the SFC either to the waste or the ICP-MS. In between the purge vial and SFC a T-connector, connecting the compartment with the CE (graphite rod) is used. The RE (Metrohm Ag/AgCl, 3 M) is connected to the electrolyte by a separate drilled hole with 0.4 mm to the cell. The working electrode (WE) is placed on an xyz-translation stage (Physical Instruments) to contact the SFC, which is mounted on a force sensor () to control the contact pressure. A silicone ring on the cell opening ~(2 mm) prevents spillage. Argon purging around the cell is employed to avoid contamination with air.
Electrochemical measurements are carried out using a Gamry 600 potentiostat. Potentiostat, purge, xyz-translation stage, and pump are controlled by a customized LabView software. A more detailed description with a scheme including the ICP-MS system is available in the literature [155].

4.1.2 H-Cell

The H-cell, as shown in figure 4.2, is a three-electrode cell in two compartments, separated by a porous frit or a membrane, that enables the collection of liquid samples for later product analysis. WE and RE are placed in one compartment, while the CE is placed in the other compartment. This configuration hinders

cationic dissolution products from crossing over to the other compartment and depositing on the CE.

H-cell measurements were performed in a homemade H-cell. The compartments were filled with 28 ml 0.1 M H_2SO_4 (Merck Milli-Q diluted Merck suprapur) each. WE and RE (Basi, 3 M Ag/AgCl) was placed in one compartment, and the CE (glassy carbon (GC) rod, SIGRADUR G, HTW GmbH) was placed in the other compartment. Parafilm was used to cover the compartments to avoid evaporation of the electrolyte. Convection in the WE compartment for evenly distributed products was induced by continuous Ar flow in the compartment. An automated liquid handler (Gilson GX-271) was used to take liquid samples. A Potentiostat (Gamry Interface1000 B) controlled the electrochemical protocol. The electrochemical protocol was started after the extraction of the first sample. At all times, the electrolyte volume in the compartments was kept at the same level between 24 ml to 28 ml.

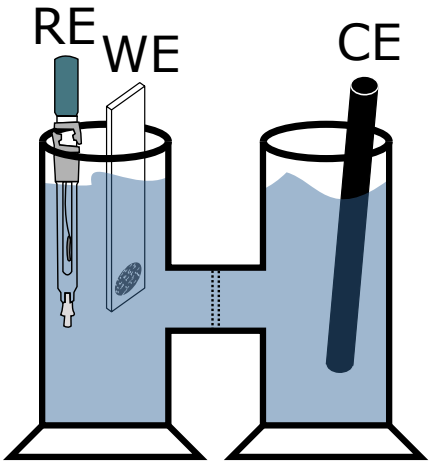

Figure 4.2: Schematic drawing of the H-cell *WE and RE are immersed in one compartment whereas the CE is immersed in the other compartment. Both compartments are separated by a porous frit to minimize deposition of ions on the CE.*

Water balance and dissolution rate calculation in H-cell

To compare dissolution rates from H-cell measurements with dissolution rates from online SFC-ICP-MS studies, the dissolution rates have to be calculated from discrete measurements of liquid samples. Thus, it is essential to know the amount of liquid present in the system at any time and account for the amount of dissolved material taken out in liquid samples. Not only sample collection and refilling have to be considered, but also water lost from the system by electrochemical water splitting. The H-cell, in the experiments shown in this work, is operated at 0.56 mA. With the Faraday equation, the amount O_2 evolved in the course of a 48 h experiment with constant current is

$$m(O_2) = \frac{MIt}{zF} = 0.008\,\mathrm{g} \qquad (4.1)$$

Compared to the volume of electrolyte in the H-cell of 24 ml to 28 ml, the mass loss is negligible and can be ignored in the calculation of dissolution rates.

The total mass loss of anode catalyst in the n^{th} time interval, $m(t_n)$, is given by

$$m(t_n) = c_m(t_n) \cdot V_0(t_n) + c_c(t_{n-1}) \cdot V_S \quad (4.2)$$

In this equation, V_0 denotes the initial volume of the respective compartment, and V_S denotes the sample volume. The concentration of dissolved anode catalyst measured in the samples is denoted by c_m, whereas the concentration calculated by taking into account the collection of samples, c_c is calculated with

$$c_c(t_n) = m(t_n) * V_0(t_n) \quad (4.3)$$

The dissolution rate in a given time interval $\Delta t = t_n - t_{n-1}$ is calculated from the mass given by equation 4.2

$$\frac{\mathrm{d}m}{\mathrm{d}t_n} = \frac{m(t_n) - m(t_{n-1})}{\Delta t} \quad (4.4)$$

4.1.3 Galvanic Replacement Free MEA setup

For the MEA measurements shown in chapter 5, a specific MEA setup was designed to prevent as much galvanic replacement (GR) as possible. Hence, all parts that do not have to be conductive are made from non-metallic materials. All parts that have to be conductive are coated, with higher oxidation potential than the anode catalyst, iridium. The parts of the setup are as follows:

Cell

The cell body is made from polytetrafluorethylene (PTFE). A grade 2 titanium sheet with 2 mm thickness was used to manufacture the flowfields with a laser-cut serpentine channel with 1 mm land and 1 mm channel spacing. The flow fields were coated with a 0.5 µm gold layer by physical vapor deposition (PVD) and subsequently by a 5 µm layer of gold by galvanic coating. The flowfields were fitted in the PTFE cell body. The inlet and outlet fittings were made from PP. The PTL between MEA and flowfield was exchanged by a 250 µm thick expanded titanium metal sheet with a 5 µm platinum coating. A carbon fiber paper (TGP-H-120, Toray) with 370 µm thickness served as PTL on the cathode side. A picture of the cell is shown in figure 4.3 a).

Test station

The measurements were carried out with a fully automated test rig (E40, Greenlight Innovation). A Gamry reference 3000 with 30 A booster was used as potentiostat. Borosilicate glass bottles with volumes between 0.5 l to 1 l served as metal-free water reservoirs for the setup. The water feed of ~300 ml min^{-1} was controlled by a NF30 membrane pump (KNF). The water reservoir temperature was kept between 55 °C to 60 °C by a heater plate (IKA) throughout the measurement. Before the cell is connected to the water flow, ionic impurities in the setup are removed by a deionizer cartridge (Leycopure mixed bed resin, Leyco), which can be bypassed in the circulation. The samples on the anode side were taken directly after the cell. Cathode water samples were taken at the collector bottle at the cathode outlet of the cell. The flow chart of the setup is shown in figure 4.3 b).

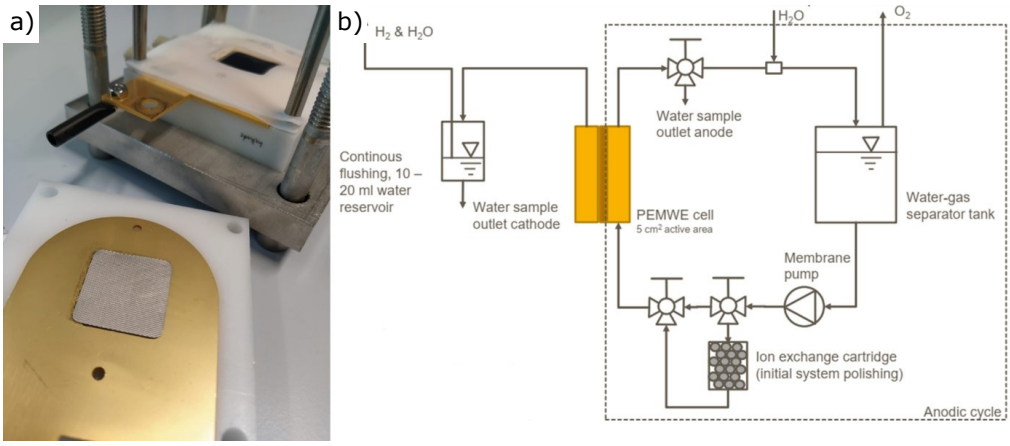

Figure 4.3: GR-free MEA setup. a) *Image of the cell body made from PTFE, gold plated titanium flow fields, and platinized titanium expanded metal as PTL.* ***b)*** *Flow scheme of GR free MEA setup. Before the measurement the setup is cleaned by short-cutting cell inlet and cell outlet and bypassing water through the deionizer cartridge. (© M. Möckl) [164]*

Measurement Procedure

Before each experiment, the setup was cleaned by circulating water at an elevated temperature for 12 h through the deionizer cartridge. The water in the circulation was processed by an ULTRA CLEAR® TP ultrapure water system (Evoqua). After cleaning, the ion exchange cartridge is removed from the circulation, and the first 10 ml sample is taken without contact to the cell. The second sample is taken after 10 min of water circulation through the cell without current. After another 10 min circulation, now at 0.2 A cm^{-2}, the third sample is taken. Afterward, the current is set to 2 A cm^{-2} for the rest of the experiment. Further samples are taken

after 10 min, 30 min, 1 h, 1 h, and afterward after every 24 h of measurement, except for weekends. Cathode samples are taken after 3 h and afterward every 24 h. The water in the anode side circulation, lost through electrolysis and electroosmotic drag, was replaced continuously by the ultra-pure water feed in aqueous experiments. Water taken through samples was replaced after taking the sample. In the test, 0.1 M H_2SO_4 replaced water. Only the sample collection volume is refilled after sample collection. The initial volume is reduced throughout the experiment by electrolysis and electroosmotic pressure. A separate test with water without refeeding was performed to check the differences. After the acidic/ultrapure tests without refeeding, polarization curves and electrical impedance spectroscopy were performed to reveal the EOL performance of the aged MEAs.

Water Balance and Dissolution rate calculation in MEA Experiments

Similar to the procedure described in section 4.1.2, the dissolution rates in the GR free MEA setup are calculated by taking the water balance into account. As the constant current used in this protocol is $2\,\mathrm{A\,cm^{-2}}$ with an MEA area of $5\,\mathrm{cm^2}$ the amount of oxygen produced during one hour of measurement is

$$m(\mathrm{O_2}) = \frac{MIt}{zF} = 6\,\mathrm{g} \tag{4.5}$$

Hence, the volume loss in the water reservoir from initially 0.5 l to 1 l is substantial. Additionally, for every hydrogen atom going from the anode side to the cathode side, around four H_2O molecules are transported as well, through electroosmotic drag [64, 65]. In experiments where water is continuously replaced, the volume loss is not taken into account. The total mass loss at the anode side at time t_n at which the n^{th} sample is taken is calculated by

$$m(t_n)_A = c_m(t_n)_A \cdot V_0 + c_c(t_{n-1})_A V_S \tag{4.6}$$

V_0 denotes the water volume in the anode cycle, and V_S denotes the sample volume, $c_m(t)_A$ denotes the concentration in the anode water cycle, and $c_c(t)_A$ is the calculated concentration in the anode water cycle, taking the mass loss through sample collection into account.
In experiments where the liquid in the anode cycle is not continuously refilled, the water loss through electrolysis, $\left(\frac{\mathrm{d}V_A}{\mathrm{d}t}\right)_E$ and the volume loss through electroosmotic drag, $\left(\frac{\mathrm{d}V_A}{\mathrm{d}t}\right)_D$ have to be taken into account. In these experiments, the total mass loss at the anode at time t_n is calculated by

$$m\left(t_n\right)_A = c_m\left(t_n\right)_A \left(V_0 - \left[\left(\frac{\mathrm{d}V}{\mathrm{d}t}\right)_D + \left(\frac{\mathrm{d}V}{\mathrm{d}t}\right)_E\right]\left(t_n\right)\right) + c_c\left(t_{n-1}\right)_A V_S \tag{4.7}$$

The water outlet at the cathode side is taken as sample completely after each time interval. Thus, the mass loss of catalyst, measured at the cathode outlet for a time interval $\Delta t_n = t_n - t_{n-1}$ is calculated with the concentration measured at the anode side, $c_m(t_n)_C$ as

$$m(t_n)_C = \left(\frac{\mathrm{d}V}{\mathrm{d}t}\right) \cdot (t_n - t_{n-q}) \cdot c_m(t_n)_C \tag{4.8}$$

The mass losses are used to calculate the dissolution rates in the interval $\Delta t_n = t_n - t_{n-1}$.

$$\frac{\mathrm{d}m}{\mathrm{d}t_n} = \frac{m(t_n)_A - m(t_{n-1})_A + m(t_n)_C}{\Delta t} \tag{4.9}$$

4.2 Inductively coupled plasma mass spectrometry (ICP-MS)

Product analysis was performed with ICP-MS (PerkinElmer NexIon 300 and NexIon 350). The ICP-MS is a mass spectrometer designed for the analysis of trace elements. The sample is introduced to the system by a peristaltic pump. Before entering the nebulizer, the samples are mixed with an internal standard (IS). The IS are elements with a similar mass and ionization energy to the analytes. It is used to divide the signal of the analyte by for a relative reference with constant input concentration. This ensures accurate measurement values even if the instrument drifts throughout the day. The nebulizer disperses the sample into a spray chamber. From here on, it is directed to an Ar-Plasma, that disintegrates and ionizes the samples. After filtering by an ion deflector, a quadrupole mass filter, a detector measures each analytes' counts. A more thorough description of the ICP-MS principle can be found in the literature [61]
Working clean is one of the critical principles of ICP-MS, as even small amounts of contaminants can influence the results. The instrument must be calibrated daily with freshly mixed calibration standards, prepared in the same electrolyte composition used in the samples. Typically a four-point calibration with concentrations of $0\,\mu g\,l^{-1}$, $0.5\,\mu g\,l^{-1}$, $1\,\mu g\,l^{-1}$, and $5\,\mu g\,l^{-1}$ was used. If sample concentrations were not in the calibration line range, the samples were diluted (liquid samples), or the calibration line extended with a $50\,\mu g\,l^{-1}$ standard. The IS was mixed in the same electrolyte matrix as the samples. A list of the used IS and their concentrations for each analyte measured is given in appendix 1.

4.2.1 Online ICP-MS

When using the instrument in the online SFC-ICP-MS configuration, a few things besides working clean have to be considered. As the instrument's data files do not contain absolute timestamps, a thorough log with start times in relation to electrochemical measurements has to be kept. Furthermore, the flow rate through the SFC (typically ~200 µl min^{-1}) must be measured regularly to ensure the correct calculation of total dissolution rates from the concentration measured in the ICP-MS. Bubbles accumulating somewhere in the microfluidic system have to be monitored closely, as they can affect the flow rate.

4.2.2 Measurement of pre-dissolved Ir in the electrolyte

For SFC measurements with pre-dissolved Ir in the electrolyte, iridium was electrochemically dissolved in 0.1 M H_2SO_4 by cycling the potential 1000 times in the potential range from 0.05 V_{RHE} to 1.5 V_{RHE} [70, 110].The iridium concentration after potential cycling was determined by ICP-MS. Electrolytes and calibration standards were prepared from the electrolyte with pre-dissolved iridium. A baseline measurement was taken before cell contact.

4.3 Electrode Preparation

4.3.1 Dropcasting

Drop casting is a technique used for easy and convenient fabrication of electrodes used in fundamental studies. An ink of either suspended catalyst particles or dissolved precursors is applied in a controlled amount with a pipette to the backing electrode material (i.e., GC, fluorine-doped tin oxide (FTO) coated glass). For further reading regarding this technique, the reader is referred to the literature [165].

IrO_x on GC IrO_x electrodes were drop-casted for SFC measurements in chapter 5. The inks were prepared by suspending $IrO_x{\cdot}2H_2O$ catalyst powder (AlfaAesar, Premion), in a solution of 87.5% ultrapure water (Merck Milli-Q), 12.5% IPA and Nafion® perfluorinated resin solution (Sigma Aldrich, 5 wt%) in variable amounts, depending on the catalyst concentration. The iridium concentration in standard inks was 663 µg l^{-1} with a corresponding Nafion® concentration of 332 µg l^{-1}. The inks were suspended as ~1 ml in an Eppendorf tube with a volume of 1.5 ml. After sonication for 10 min (4 s pulse, 2 s pause)) with a sonication horn, the inks were drop-casted as 0.2 µl to a freshly polished GC plate (SIGRADUR G, HTW). A Keyence VK-X250 profilometer was employed to screen the quality and

the diameter (∅~1.3 mm) of the drop-casted spots. Exemplary spots for different loadings from 10 $\mu g_{Ir}\,cm^{-2}$ to 250 $\mu g_{Ir}\,cm^{-2}$ are shown in figure 4.4. The spot with the highest loading of 250 $\mu g_{Ir}\,cm^{-2}$, shown in figure 4.4, deviates slightly in size from the other spots. The increased size can be explained by a higher IPA content of the catalyst ink. As the Nafion® solution contains IPA as well, and the Nafion® fraction in the ink is kept constant, a higher content of IPA in the catalyst ink unavoidable. Thus, the higher IPA content leads to a higher diameter of the spots.

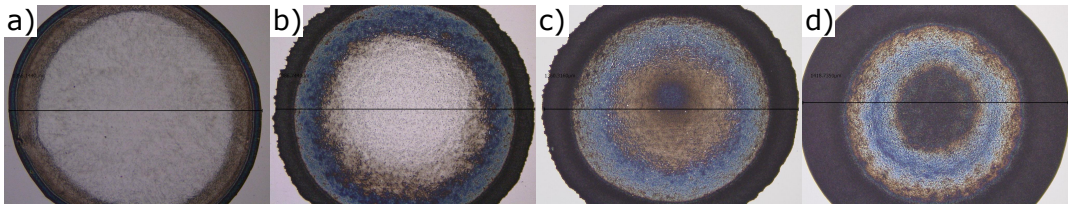

Figure 4.4: Examplary microscope images of IrO_x catalyst spots with varied loading. a) *10 $\mu g_{Ir}\,cm^{-2}$.* ***b)*** *50 $\mu g_{Ir}\,cm^{-2}$.* ***c)*** *100 $\mu g_{Ir}\,cm^{-2}$.* ***d)*** *250 $\mu g_{Ir}\,cm^{-2}$.*

IrO_x on FTO IrO_x were drop-casted on FTO coated glass slides (Sigma Aldrich) for H-cell measurements in chapter 5. The ink was prepared by suspending $IrO_x{\cdot}2H_2O$ (AlfaAesar, Premion) powder in ultrapure water (Merck, Milli-Q). The iridium concentration in the ink was 283 $\mu g\,l^{-1}$. The volume of the ink was ~1 ml, prepared in a 1.5 ml Eppendorf tube. After sonication for 15 minutes (4 s pulse, 2 s pause)), 10 µl of the ink are drop-casted on an FTO coated glass slide. The glass slide is cleaned before drop-casting by sonicating subsequently in 2% Hellmanex III solution, H_2O and IPA, 10 min each [166].

WO_3 on Au WO_3 electrodes were prepared on Au backing electrodes for the measurements shown in chapter 7. The ink was prepared by suspending 99.445 mg commercial WO_3 nanoparticles (Sigma Aldrich, <100 nm (TEM)) in 2.9 ml H_2O (Merck, Milli-Q). 252 µl Nafion® perfluorinated resin (Sigma Aldrich, 5 wt%) solution was added to the suspension. After 40 min (4 s pulse, 2 s pause) sonication, the ink was drop-cast as spots of 0.3 µl on a freshly polished gold foil (Alfa Aesar, 99.95% metals basis). After drying, the electrodes were annealed at 600 °C for 3 h with a ramp of 3 $K\,min^{-1}$.

4.3.2 MEA fabrication

MEAs used in chapter 5 were prepared by a decal transfer method. $IrO_x{\cdot}2H_2O$ catalyst powder (AlfaAesar, Premion) was used as anode catalyst. The anode catalyst loading was ~1 $mg_{Ir}\,cm^{-2}$ for all experiments. The cathode catalyst was carbon

supported (Vulcan XC72) platinum nanoparticles (45.8 wt% Pt/C; TEC10V50E from Tanaka, Japan) with loadings of ~0.3 $mg_{Pt}\,cm^{-2}$. The catalyst inks were prepared by mixing catalyst powders IPA ($\geq$ 99.9 %, Sigma Aldrich) and Nafion® ionomer solution (20 wt% ionomer, D2021, IonPower) for 24 h with a roller mill and 5 mm zirconia grinding balls. A Mayer-rod coating machine was used to coat the decals on 50 µm PTFE foil (Angst+Pfister). The decals were hot-pressed to Nafion® type 117 membranes (thickness 180 µm) for 3 min at 155 °C with a pressure of 2.5 MPa. Catalyst loadings were calculated from weighing the samples before and after hot-pressing with an XPE105DR microbalance (Mettler Toledo). The anodes all had an ionomer content of 9 wt%, and the cathodes had an ionomer to carbon mass ratio of 0.6/1.

4.3.3 Spray-coating

Spray-coating was used to prepare WO_3 on FTO samples used for photoelectrochemical measurements in chapters 8 and 9. The peroxotungstic acid precursor was prepared by dissolving 5 g W powder (fine powder 99+, Merck) in 25 ml H_2O_2 (30%, Merck) [146, 147, 150, 167]. After complete dissolution of the tungsten powder, H_2O (Merck, Milli-Q) was added to the solution. To remove excess H_2O_2, the solution was heated under continuous stirring and reduced to 20 ml. Afterward, it was diluted with IPA to 200 ml.
The precursor solution was spray-coated with an ExactaCoat device (SonoTek) in 24 cycles. The hot plate's temperature was set to 80 °C. A flow rate of 0.33 $ml\,min^{-1}$ was used to spray the ink with an ultrasonication power of 5 W, a nozzle height of 37 mm and a traverse speed of 140 $mm\,s^{-1}$. The used pattern was meander-shaped with a 1.5 mm pitch size.
The samples were calcinated at 500 °C for 1 h with a ramp of 2 $K\,min^{-1}$ after spray-coating.

4.3.4 Atomic Layer Deposition

For measurements in chapter 9, the electrodes from section 4.3.3 were coated with Ir by atomic layer deposition (ALD). The films were deposited with a commercial Gemstar-6 ALD reactor (Arradiance). Ozone, generated by a BMT 803N ozone generator and Ethylcyclopentadienyl-1,3-cyclohexadiene-iridium(I) (abcr), heated to 90 °C were used as precursors. The reaction chamber was held at 220 °C. Spray-coated WO_3 films before and after the ALD treatment are shown in figure 4.5. As visible in the figure, the transmittance of light decreases with increasing iridium layer thickness.

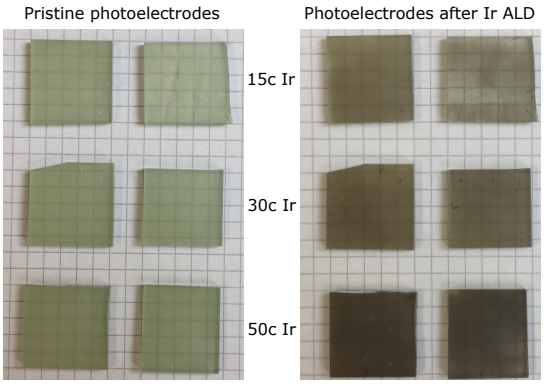

Figure 4.5: Spraycoated WO_3 thin films before and after ALD with Ir. *The samples are shown pristine on the left side and after the treatment on the right side. The quad paper is used to display the transmittance of the samples.*

4.4 Characterization

4.4.1 Scanning (Transmission) Electron Microscopy

Scanning electron microscpy measurements A Zeiss Crossbeam 540 focused ion beam scanning electron microscope (FIB-SEM) with Gemini II column was used to perform scanning electron microscopy (SEM) measurements. The WO_3 samples (synthesis described in section 4.3.3) were attached to an aluminum SEM specimen stub with double-sided adhesive copper tape before the measurements. To ensure better conductivity, the samples were additionally coated with a carbon sputter coater (balzers Union, MED 010). To further increase the conductivity of the region of interest, the WO_3 surface was directly electrically connected to the FTO surface by the deposition of a small conductive Pt layer via ion beam deposition, which was performed with a gas injection system (Orsay Physics, MonoGIS). SEM micrographs were obtained with 3 kV acceleration voltage and a current of 750 pA.
To determine the thickness of WO_3 layers, FIB cross-sections were taken. A protective Pt layer was deposited via ion beam deposition above the region of interest. Trenches were milled with an ion beam current of 3 nA and an acceleration voltage of 30 kV. SEM micrographs were obtained afterward with 3 kV acceleration voltage and a current of 750 pA.

Scanning Transmission Electron microscopy measurements To acquire scanning transmission electron microscopy (STEM) micrographs used samples from MEA measurements (see section 4.1.3) were embedded in Araldite 502 epoxy resin and stored overnight at 60 °C. An RMC Boeckeler PowerTome using Diatome ultra 45° diamond knife was used to cut ultrathin sections with a nominal thickness of 100 nm. The sections were placed onto copper grids for imaging with STEM.
A Zeiss Crossbeam 540 FIB-SEM with annular scanning transmission electron microscopy (aSTEM) was used to acquire STEM micrographs. A detector voltage of 20 kV and a probe current of 300 pA were used. For a higher contrast between atoms with low atomic number Z (membrane: F, C, ·..) and high atomic

number (Ir, Au, Ti), the imaging mode High-angle annular dark-field (HAADF) was chosen. energy-dispersive X-ray spectroscopy (EDX) (X-ray detector: X-Max 105 silicon drift detector, Oxford Instruments; Software: Aztec Version 3.3, Oxford Instruments) was used to analyze the chemical composition. An accelerating voltage of 20 kV was used as well as a probe current of 300 pA.
After acquisition, the micrographs were post-processed with *ImageJ*. As the ion beam's penetrating depth is deeper than the nominal thickness of the sample, some background noise might appear from the copper TEM grid. The displayed elements are narrowed down to the elements of interest in post-processing.

4.4.2 X-ray Photoemission Spectroscopy (XPS)

X-ray photoemission spectroscopy (XPS) was performed to determine the surface composition of WO_3 samples covered by ALD with Ir (see section 4.3.4). The spectra were recorded using a PHI Quantera II scanning X-ray microprobe with Al K_α radiation froma 200 µm spot at 50 W and 15 kV with a dwell time of 200 ms per step. High-resolution scans were recorded with a step size of 0.125 eV at 140 eV pass energy, whereas survey scans were performed with a step size of 0.5 eV at 280 eV pass energy. The recorded spectra were analyzed in *CasaXPS* (v.2.3.18) using the instrument-specific relative sensitivity factors. The binding energy scale was calibrated to the adventitious carbon peak at 284.8 eV.

4.4.3 Ellipsometry

The thickness of the iridium layers applied by ALD was determined by spectroscopic Ellipsometry on SI(100) wafers that were present in the chamber during the coating process. To perform measurements, a SENPro from SENTECH was used. Measurements were performed in a spectral range from 370 nm to 1050 nm with an incident angle of 70°. The data was processed and fitted with *SpectraRay/3* applying an optical model, in which layer thickness, as well as optical constants (refraction index, Psi, and Delta) are used.

4.4.4 UV-Vis Spectroscopy

Ultraviolet-visible (UV-vis) spectroscopy was performed with an optical spectrophotometer (OceanOptics) with a deuterium-halogen light source (DH-2000-L) and a HR4000spectrometer. The transmitted intensities were subtracted from the incident intensity to acquire absorption spectra.

4.4.5 X-ray Diffraction (XRD)

X-ray diffraction (XRD) was used to determine the crystal structure of the electrodes in Bragg-Brentano geometry. A Bruker D8 Advance with a CuK_α source and a LynxEye XE detector were used to perform measurements.

4.4.6 Laser Microscopy

The diameters and profiles of drop-cast spots (compare section 4.3.1) were determined with a Keyence VK-X250 laser microscope. Imaging was performed with 20x magnification and slow scan speed in manual mode. Images were stitched and processed with the software from the microscope.

5 Iridium dissolution in MEA devices

Parts of the following study were published under the title: "On the limitations in assessing stability of oxygen evolution catalysts using aqueous model electrochemical cells" [164].
Julius Knöppel, as the first author, designed the experiments, prepared and measured electrodes in SFC-ICP-MS and H-cell studies performed liquid sample analysis of MEA and H-cell samples by ICP-MS, data analysis, and wrote the original draft of the manuscript.

5.1 Introduction

As discussed in section 3.1.2, a severe discrepancy was observed in OER catalyst stability between AMS and MEA. The work shown in this chapter deals with resolving this dissolution discrepancy. Parameters known to diverge in both systems, such as catalyst loading, mass transport conditions, Nafion binder content, and electrolyte pH, are varied separately in the AMS. The dissolution rates in the AMS are compared with accurate dissolution rates measured in a specifically designed MEA system (see section 4.1.3 for further details). An overestimation of the membrane acidity and a catalyst stabilization with long operating time in the MEA are identified as the main contributors to the discrepancy.

5.2 Results and discussion

5.2.1 Iridium based OER catalyst dissolution: AMS versus MEA

As discussed in section 3.1.2, the dissolution behavior of OER catalysts in AMS is already well studied. With online dissolution measurements, utilizing flow cells coupled to analytics, the dissolution behavior of OER catalysts in various operational conditions has been revealed. Degradation studies in MEA, on the other hand, are always based on indirect measurements such as cell voltage. Therefore it is essential to highlight the commonalities and differences of both systems to put the later shown results into context. In AMS, schematically shown in figure 5.1 a), the acid or base, employed as electrolyte, is diluted by DI water. The reaction products, O_2 at the anode side and H_2 at the cathode side, diffuse into the bulk as well as

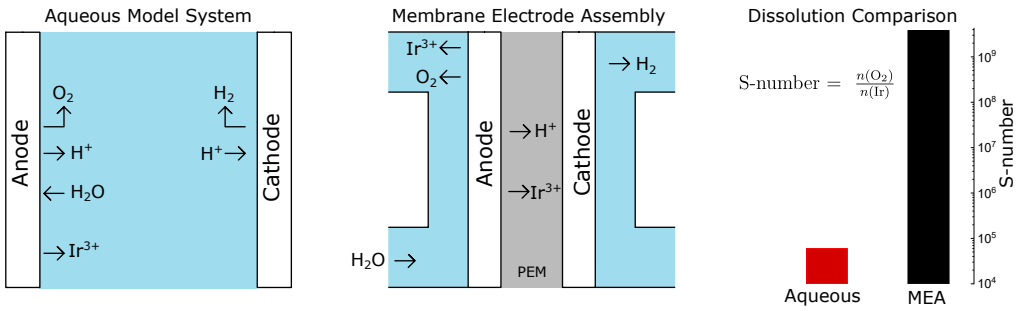

Figure 5.1: Degradation processes of OER catalysts in aqueous and polymer electrolyte a) *Schematic drawing of degradation processes in a classical AMS.* ***b)*** *Schematic drawing of degradation processes in MEA.* ***c)*** *Dissolution stability of IrO_x under OER conditions in aqueous electrolyte, measured in SFC-ICP-MS, and polymer electrolyte measured in the GR-free MEA, expressed in the S-number metric. Measurements were carried out with a 5 min chronopotentiometric hold in AMS and over several days in MEA. The timescales are typical for the respective systems.*

dissolution products from the electrodes catalysts (e.g. $Ir_3{}^+$).
To measure dissolution of anode catalyst materials, it is sufficient to perform sample analysis of liquid samples taken from the bulk. With utilization of flow cells, that enable direct transport of electrolyte, containing dissolution products, from the reaction site to downstream analytics, such as ICP-MS, dissolution behavior can directly be correlated to electrochemical operation [38, 168, 169].

The studies of degradation in MEA, on the other hand, are limited by the higher degree of complexity in comparison to AMS. Long-term measurements and EOL studies have been used so far. However, due to the long lifetimes of PEMWE, this data is scarce. Furthermore, measurement of dissolution products in MEA is not as straightforward in comparison to AMS. The pathways of educts products and dissolution products in MEA are schematically shown in figure 5.1. Here, the polymer electrolyte and the reactant are decoupled. DI water as the reactant circulates at the backside of the anode. The PEM is sandwiched between the electrodes. Reaction products, O_2 and H_2, escape through PTLs at the back sides of the respective electrodes. H^+ as anode reaction product is transported through the PEM towards the cathode side. Dissolution products from OER catalysts at the anode side can escape the anode catalyst layer along two pathways: with the DI water in the anode cycle or through the PEM towards the cathode side. Especially in the anode water cycle, GR of dissolution products with stainless steel, used for the tubing of MEA setups, is a problem that can lead to an underestimation of dissolution [118].

Therefore, several factors have to be taken into account to determine catalyst dissolution in MEA reliably. Not only iridium concentrations but water levels

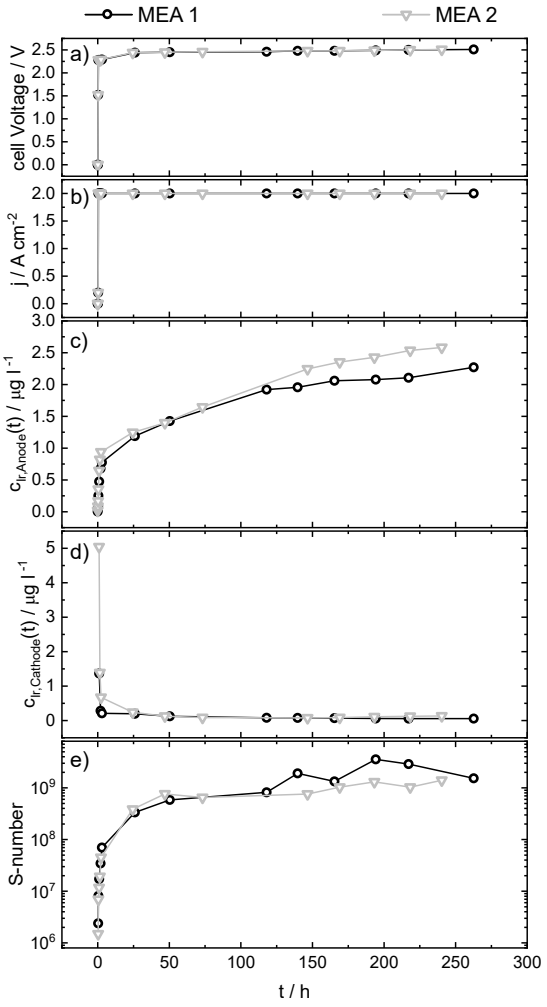

Figure 5.2: Electrochemical and stability parameters of IrO_x in an MEA as functions of time. ***a)*** *Cell voltage.* ***b)*** *Current density.* ***c)*** *Iridium concentration in the anode water cycle.* ***d)*** *Iridium concentration at the cathode outlet.* ***e)*** *S-number, calculated from the amounts of dissolved iridium. The black and grey data refers to two independent experiments with the same catalyst.*

that decrease through the reaction and electroosmotic drag [64, 65], have to be constantly monitored. Another factor that might lead to an underestimation of Ir dissolution in MEA might be iridium depositing in the membrane. Thus, the amount of iridium in the membrane has to be estimated after the experiment.
The MEA experiments shown in this chapter, were carried out with a setup developed explicitly for this purpose. Every part of the cell involved in electronic conduction was platinized (PTL) or gold-coated (bipolar plates). All other parts of the cell were made from non-metallic parts. Samples were taken from the anode water cycle and the cathode outlet and separately analyzed by ICP-MS. A detailed description of the setup and water balance calculations are available in section 4.1.3.
For a comparison of dissolution rates in both systems, the same commercially IrO_x catalyst (AlfaAesar) was studied in both AMS and MEA. The S-numbers of both systems from constant current measurements at typical timescales and currents for both systems (AMS: 5 min, 100 mA mg_{Ir}^{-1}; MEA: 14 days, 2 A cm^{-2}) are displayed in figure 5.1 c). Electrochemical data and dissolution data for MEA is shown in figure 5.2. Dissolution data and electrochemical data for SFC measurements is

shown and discussed in section 5.2.2.
Typical S-numbers for IrO_x in aqueous electrolyte are between 10^4 to 10^5 [38]. This is in line with the observed value of 6×10^4. As expected from previous results, the S-number in the MEA is 10^9, exceeding the S-number observed in the AMS by almost five orders of magnitude. In the following sections, further experiments are performed in both systems to unravel the difference in behavior.

5.2.2 Evaluation of AMS stability parameters

To determine the underlying reasons for the diverging dissolution behavior in AMS and MEA, five parameters known to differ in both systems were individually varied in experiments with SFC-ICP-MS. The parameters were: (a) catalyst loading; (b) electrolyte flow rate; (c) presence of electrochemically pre-dissolved iridium species; (d) Nafion content in the catalyst layer; and (e) pH. The same IrO_x powder as for MEA experiments was used.
The full electrochemical protocol that was used for all SFC-ICP-MS measurements is shown in figure 5.3. The applied potential is shown in figure 5.3 a), the resulting current and iridium dissolution are shown in figure 5.3 b) and c). The sample is contacted at OCP. After a waiting period of 3 min the contact dissolution peak relaxes to the baseline. Afterward, three fast cyclic voltammetry (CV)s with a scan rate of 500 $mV\,s^{-1}$ from 0.05 V_{RHE} to 1.4 V_{RHE} follow to evaluate the electrode quality. After the dissolution peak from the CVs has relaxed to the baseline, a linear sweep voltammogram (LSV) with a scan rate of 5 $mV\,s^{-1}$ from 1.1 V_{RHE} to 1.65 V_{RHE} is performed to measure electrochemical activity of the electrodes. Also, it shows a first impression of the stability of the electrode. The S-numbers of the respective electrodes are measured in a 30 s interval towards the end of a 5 min chronopotentiometric hold at 100 $mA\,mg_{Ir}$, as suggested in the literature [38].

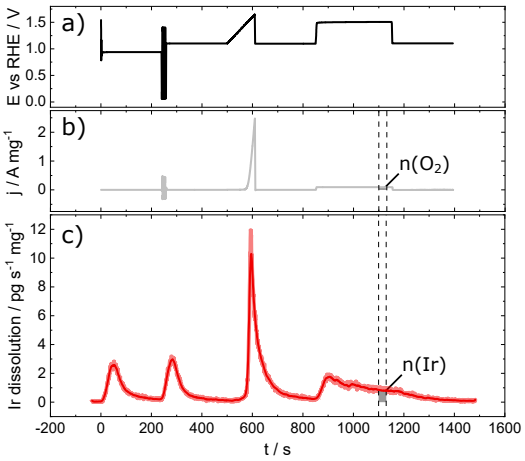

Figure 5.3: Electrochemical protocol used for SFC-ICP-MS measurements in this study. ***a)*** *Potential versus RHE.* ***b)*** *Current density normalized to spot loading.* ***c)*** *dissolution profile of an IrO_x catalyst spot at standard conditions ($10\,\mu g_{Ir}\,cm^{-2}$ catalyst loading, $200\,\mu l\,min^{-1}$ flow rate, fresh electrolyte, 33 wt% Nafion in the catalyst layer, and 0.1 M H_2SO_4 (pH=1)). The dashed lines and grey areas in* ***b)*** *and* ***c)*** *mark the integration area for the calculation of S-numbers.*

The dissolution profiles of the variations (a), (b), and (c) are shown in figure 5.4. Dissolution profiles of the variations (d) and (e) are shown in figure 5.5. S-numbers,

calculated for all measurements with error bars from at least three independent measurements are shown in figure 5.6.
The first study focused on stability differences arising due to differences in catalyst loading. The loading of iridium-based electrodes in AMS experiments usually is around $10\,mg_{Ir}\,cm^{-2}$. The loading in a typical MEA, on the other hand, is around $1\,mg_{Ir}\,cm^{-2}$ to $2\,mg_{Ir}\,cm^{-2}$ [170]. The loading in SFC-ICP-MS experiments was varied between $10\,mg_{Ir}\,cm^{-2}$ to $250\,mg_{Ir}\,cm^{-2}$. Representative dissolution profiles are shown in figure 5.4 b). The dissolution profiles show only slight variations within each other. No significant difference, especially in the chronopotentiometric hold, was observed. Calculation of S-numbers for these measurements, as shown in figure 5.6 b) confirms the first impression. The S-number values are all comparable. Therefore an influence of loading on the dissolution discrepancy is unlikely.

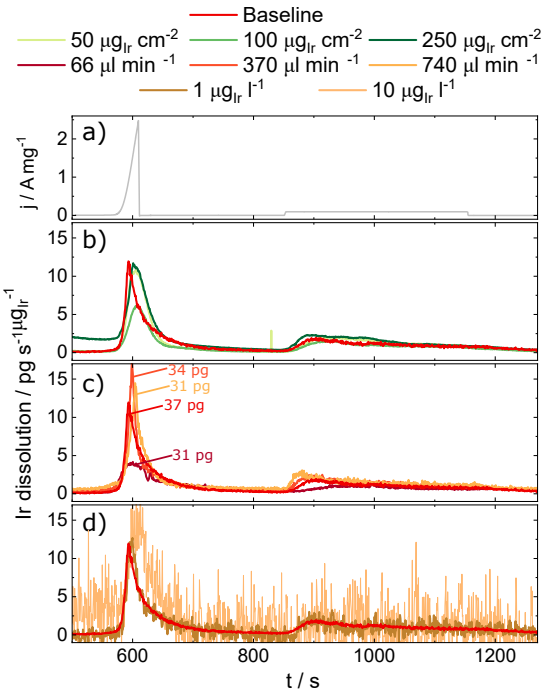

Figure 5.4: Dissolution of IrO_x catalysts spots with varied loading, flow rate and pre-dissolved Ir in electrolyte in comparison to a measurement at standard conditions.a) *Mass normalized current of the baseline measurement* ***b)*** *Dissolution profiles of catalyst spots with variation of surface normalized catalyst loading.* ***c)*** *Dissolution profiles of catalyst spots with variation of mass transport conditions (flow rate).* ***d)*** *Dissolution profile of a catalyst spot measured in electrolytes containing electrochemically pre-dissolved Ir.*

The second study focused on stability differences that might arise through different mass transport velocities of dissolved species from the reaction site. Thus, the flow rate of the electrolyte was varied between $66\,\mu l\,min^{-1}$ to $740\,\mu l\,min^{-1}$. Representative dissolution profiles at different flow rates are shown in figure 5.4 c). As mass transport properties of dissolved catalyst species from the catalyst surface to the ICP-MS are changing with the flow rate of electrolyte through the cell, a different tailing behavior is expected at different flow rates [171]. Hence, the dissolution profiles deviate, especially at the beginning and the end of the current step.
As expected, the dissolution profiles during the LSV deviate. However, the integration of the peaks shows no significant difference in dissolution between flow rates. After reaching a quasi-steady state towards the end of the applied galvanostatic hold, the iridium dissolution rate of all four flow rates is virtually equivalent.

The S-numbers, as shown in figure 5.6 c) confirm this impression. No significant difference is observed. As the flow rate dictates the mass transport of dissolved species from the electrode interface to the bulk electrolyte, it should interact with a potential iridium redeposition mechanism. Based on the results obtained, these mass transport phenomena do not seem to play a critical role in the observed stability differences.
In the AMS, usually, fresh electrolyte and clean conditions are used. On the other hand, dissolved species might circulate in the MEA system and contribute to a potential dissolution-redeposition equilibrium. To measure the dissolution with electrochemically pre-dissolved iridium species, Ir is dissolved from polycrystalline iridium [70, 110] as described in section 4.2.2 and then incorporated in the acidic electrolyte used. The iridium concentration in the electrolyte was determined by ICP-MS and the standards were adjusted accordingly. Figure 5.4 d) shows dissolution profiles of iridium concentrations of $1\,\mu g_{Ir}\,l^{-1}$ and $10\,\mu g_{Ir}\,l^{-1}$ in contrast to the baseline measurement. The iridium concentrations are in the same order of magnitude as those found in this and other studies [118, 119]. As observed with the previous variations, the measurement with $1\,\mu g_{Ir}\,l^{-1}$ does not diverge significantly from the baseline measurement. Only the signal-to-noise ratio worsens. As shown in figure 5.6 d), the stability does not change in the contaminated electrolyte, either. Only the error bars increase. In the measurement, where $10\,\mu g_{Ir}\,l^{-1}$ were incorporated into the electrolyte, the noise becomes so strong that integrating the dissolution peak is virtually impossible. However, the dissolution profile from the LSV is of the same form and in the same order of magnitude as the one of the baseline measurement. Hence, a redeposition mechanism unlikely contributes to the differences between AMS and MEA.

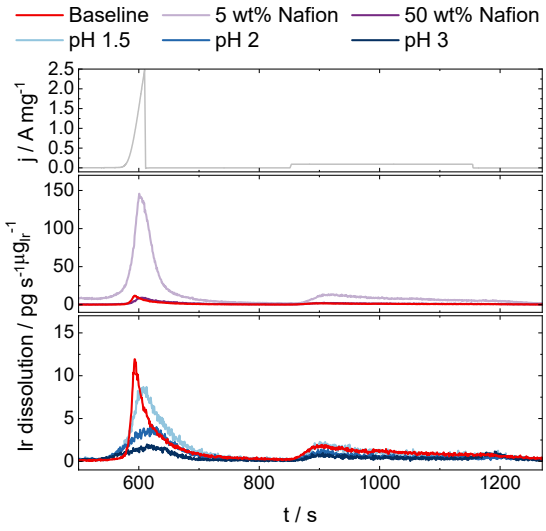

Figure 5.5: Dissolution of IrO_x catalysts spots with varied Nafion content in the catalyst layer and varied electrolyte pH. a) *Mass normalized current of the baseline measurement* ***b)*** *Dissolution profiles of catalyst spots with variation of Nafion content in the catalyst layer.* ***c)*** *Dissolution profiles of catalyst spots with varied electrolyte pH.*

The fourth parameter evaluated in this study is the influence of the Nafion® content in the catalyst layer on the dissolution behavior of iridium-based OER catalysts. In typical RDE experiments, no Nafion® is used. In electrodes, prepared for measurements with the SFC-ICP-MS system, and in MEA, it serves as binder in the catalyst layer to avoid particle detachment. The dissolution curves, shown in figure 5.5 b)

were measured on IrO_x spots, where the Nafion® content of the catalyst spots was varied between 5 wt% to 50 wt%. Interestingly, dissolution rates, measured on electrodes containing only 5 wt% Nafion®, are drastically increased against the other two Nafion® contents tested. Upon comparing the S-numbers, shown in figure 5.6 e), one sees that electrodes with reduced Nafion® content have an S-number of 8×10^3, almost an order of magnitude lower than the baseline measurement. As mass transport conditions at the electrode bulk electrolyte interface were excluded as the reason for different dissolution behavior due to the catalyst layer thickness and flow rate studies. Thus, a possible reason for the observed behavior might be a more efficient mass transport of dissolved iridium species from within the catalyst layer to the interface. A local saturation in catalyst layers with higher Nafion® content might inhibit dissolution. The baseline AMS measurements have a Nafion® content of 33 wt%, while MEA electrodes are produced with a 9 wt% Nafion® content. Thus, an influence on the results in this study can not be excluded. However, as aligning the Nafion® content, employed in this study would instead open the gap between MEA and AMS more, instead of contributing to close it, this error rather leads to underestimating the size of the stability discrepancy gap.

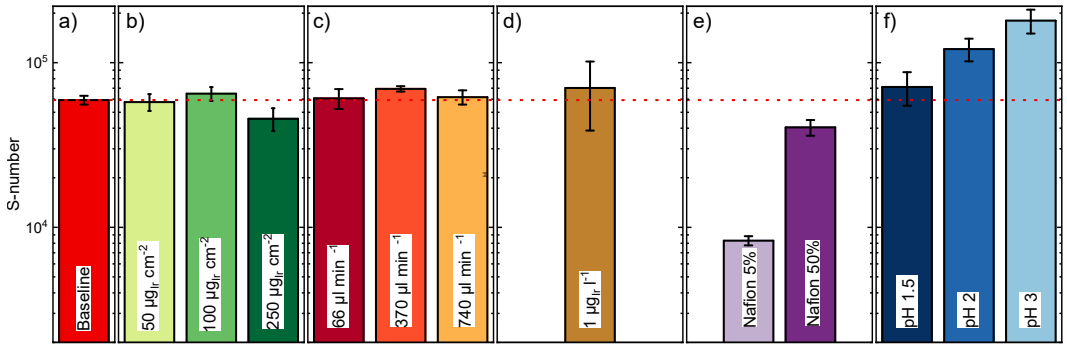

Figure 5.6: S-numbers of IrO_x catalyst spots with varied conditions. ***a)*** *Measurement at standard conditions ($10\,\mu g_{Ir}\,cm^{-2}$ catalyst loading, $200\,\mu l\,min^{-1}$ flow rate, fresh electrolyte, 33 wt% Nafion in the catalyst layer and 0.1 M H_2SO_4 (pH=1)).* ***b)*** *Variation of surface-normalized catalyst loading.* ***c)*** *Variation of electrolyte flow rate.* ***d)*** *Addition of electrochemically pre-dissolved iridium to the electrolyte.* ***e)*** *Variation of Nafion content in the catalyst layer.* ***f)*** *Variation of electrolyte pH. The red dashed line indicates the value of the baseline measurement.*

The fifth parameter studied was a variation of the electrolyte pH. It was varied between 1 to 3. To ensure a similar ionic strength between the different electrolytes, a sulfate salt was added to electrolytes with pH > 1. The experimental dissolution profiles are shown in figure 5.5 c). They significantly differ from each other. When comparing S-numbers of electrodes at different pH values, shown in figure 5.6 f), one observes significant differences. The S-number for pH 1.5 is still similar to the reference measurement at pH 1. A factor of three lies between the S-numbers of the lowest pH 1(S-number=6×10^4) and the highest pH 3 (S-

number= 1.8×10^5). It is noteworthy that electrolytes with higher pH might have a lower pH under OER conditions than in preparation due to worsened buffer capacitance [172]. In the literature, Nafion®is assumed to operate at highly acidic conditions [66, 67]. The results shown here indicate that the acidity present in the anode catalyst layers of MEA might have been overestimated in previous studies. Further experiments in MEA have to be conducted for confirmation or disproval of these indications.

5.2.3 Impact of operating timescale on catalyst stability in AMS and MEA

A sixth diverging factor between AMS and MEA is the different operating timescale. The results, shown in section 5.2.1, for example, were generated with a 5 min measurement in AMS and several days in MEA. While measurements in AMS last maximally hours to days, MEA systems in PEMWE have proven to be stable for thousands of hours on the lab scale [173] and the industrial scale [174]. Therefore it was investigated if the short experimental timescale in AMS can be extrapolated to MEA or if stabilization effects in either of the systems take place.

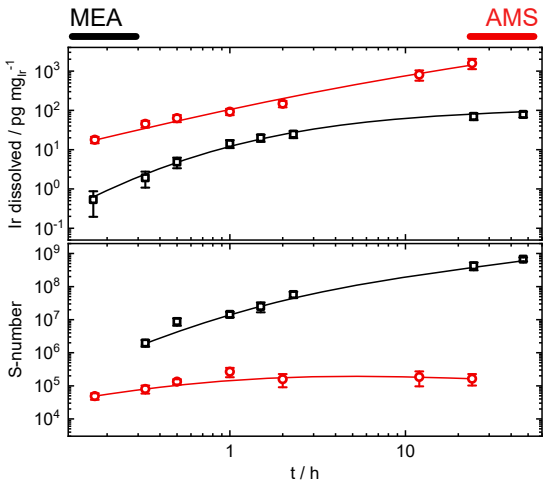

Figure 5.7: Long term stability of IrO_x in AMS and MEA environment. ***a)*** *Amount of total dissolved iridium as a function of time normalized by the electrode loading.* ***b)*** *S-numbers calculated from the amounts of dissolved iridium. The lines are added for ease of interpretation.*

Due to the microfluidic nature of the SFC-ICP-MS system, which facilitates bubble accumulation, electrochemical measurements, representative for the AMS, were carried out in an H-cell configuration with automated sample collection. 0.1 M H_2SO_4 was used as electrolyte. To directly compare the results, samples from MEA were taken from the anode water cycle and the cathode outlet. The total dissolved iridium mass loss for both systems was calculated according to the methods described in the Materials and Methods section.
H-cell measurements were carried out with electrode loadings of $10\,\mu g_{Ir}\,cm^{-2}$ at a current density of $0.2\,A\,mg_{Ir}^{-1}$. MEA measurements were carried out with anode loadings of $1\,mg_{Ir}\,cm^{-2}$ at a current density of $2\,A\,mg_{Ir}^{-1}$. Loading normalized

dissolution as a function of time is displayed for both systems in figure 5.7 a). The amount of dissolved iridium rose in the AMS almost constantly throughout the experiment, after a slight stabilization at the beginning. This negligible stabilization is confirmed when S-numbers are calculated. S-numbers for both systems are shown in figure 5.7 b). The S-number of IrO_x in the AMS stabilizes only marginally from 7×10^4 to 2×10^5.
In contrast to the results in the AMS, the amount of total dissolved iridium stabilizes after a few hours to an almost constant level. From an initial value of 10^7 they stabilized rapidly to a level of 10^8 and, in the later course of the experiment, even to 10^9.
The results obtained with the GR-free MEA system are in heavy contrast to the results shown by Babic et al. [118]. In their experiments, the authors observed fluctuating or even decreasing concentrations of iridium in the water cycle. The authors speculated that GR might have been the cause for the observations. Similar results were obtained by Regmi et al. [119], although their protocol is not directly comparable to the one used in this study. The results obtained with the GR-free MEA setup show a clear advantage in dissolution studies compared to conventional setups. Therefore, in studies covering catalyst dissolution in MEA devices, GR should always be excluded. Otherwise, the conclusions drawn from the experiments might be misleading.
Stabilization of iridium-based catalysts under long-term operation due to cristallization of the catalyst was suggested in previous research [76]. If this effect were causal for the stabilization, its observation would be expected in both AMS and MEA. The fact that a significant stabilization is only observed in MEA might be related to the higher gravimetric current density of $2\,\mathrm{A\,mg_{Ir}^{-1}}$ in comparison to $0.2\,\mathrm{A\,mg_{Ir}^{-1}}$ in the AMS. As the current density in AMS is subject to mass transport limitations, such an effect can not entirely be excluded in the aqueous system. Methods to circumvent this limitation, for example, on the foundation of existing gas diffusion electrode (GDE) setups might become a method to circumvent this limitation [175–179].

5.2.4 Impact of pH on MEA operational stability

As shown in section 5.2.2, a higher pH seems to stabilize IrO_x in AMS. It was the only parameter with a significant and unambiguous impact on closing the gap between the two systems. To test the impact of a lowered pH environment in MEA, DI water in the anode water cycle was exchanged for 0.1 M H_2SO_4. A short schematic display of the principles is shown in figure 5.8 a) for the MEA operated with DI water and in figure 5.8 and b) for the MEA operated with sulfuric acid. S-numbers were calculated for both systems from samples taken after 2 h of continuous operation at $2\,\mathrm{A\,mg_{Ir}^{-1}}$ and are displayed in figure 5.8 c).

The S-number of IrO_x in the MEA operated with acid diverges considerably from the S-number of IrO_x in the conventional MEA. It decreases by more than two

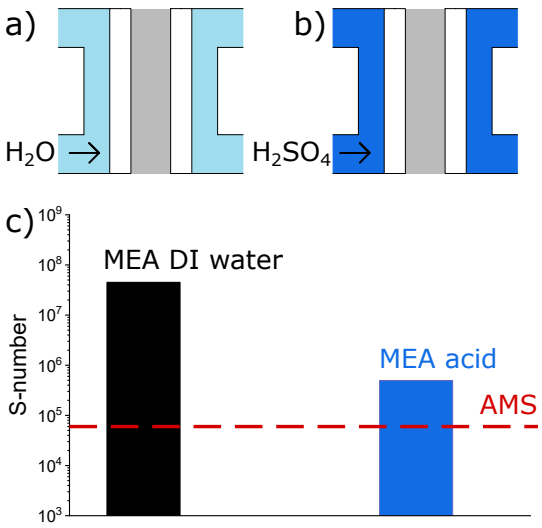

Figure 5.8: Comparison of MEA stability operated conventionally with H_2O and with 0.1 M H_2SO_4. *a) Working principle of the MEA operated with DI water.* ***b)*** *Working principle of an MEA operated with 0.1 M H_2SO_4.* ***c)*** *S-numbers of MEAs operated with DI water and 0.1 M H_2SO_4 after two hours of measurement. The red dashed line in* ***c)*** *is added for comparison to the AMS system.*

orders of magnitude, closing the gap toward the AMS, which operates with S-numbers of 6×10^4 to less than an order of magnitude. The difference between AMS and MEA virtually vanishes when the latter is operated with acid. The impact of an S-number decrease by two orders of magnitude can be exepmlified if the resulting half-life of the system is calculated from them [38]. The lifetime of the conventional MEA is around 150 years, whereas the lifetime of the acidified MEA is only several days.
On a longer timescale than two hours, more destructive effects in the acidified MEA are observed. The analysis of metallic elements present in the system is shown in figure 5.9 as a function of time.

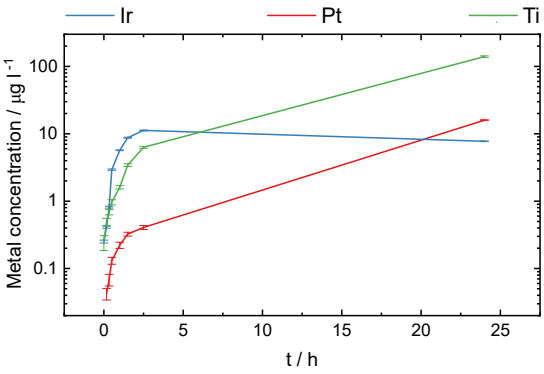

Figure 5.9: Concentrations of the elements Ir, Pt, and Ti in the MEA operated with 0.1 M H_2SO_4 as a function of time.

While the measured iridium concentration in the first hours of the experiment resembles the curve from the conventional system, although the absolute values are higher, it decreases in the measurement after 24 h. This decrease resembles the results shown by Babic et al. [118]. On the other hand, the concentrations of platinum and titanium, the elements from the stretched metal that serves as PTL, begin to rise strongly. It appears that the lowered pH in the system, as well as the electrolytic contact to the PTL, causes it to participate in the OER. Nevertheless, it is highly likely, that the main proportion of OER activity still takes place on the catalytically more active anode catalyst layer. However, it appears that dissolution

of the Pt protective layer on the PTL causes the Ti body of the PTL to be exposed to the electrolyte. The exposition of Ti to the electrolyte explains the decrease of Ir in the anode water cycle at later times. As titanium is a less noble metal than iridium GR is most likely the cause.

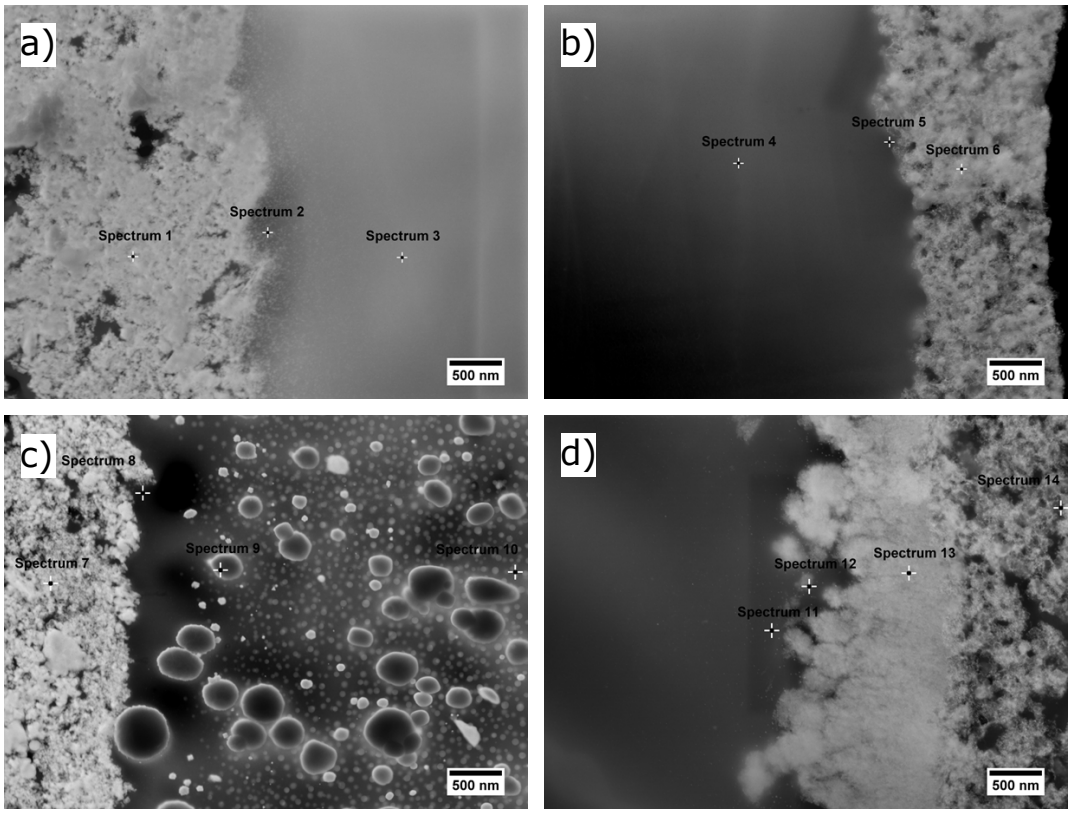

Figure 5.10: STEM micrographs of the anode (a,c) and cathode (b,d) sides of an MEA operated with DI water (a,b) and 0.1 M H_2SO_4. a) *Anode catalyst layer of an MEA operated with DI water.* ***b)*** *Cathode catalyst layer of an MEA operated with DI water.* ***c)*** *Anode catalyst layer of an MEA operated with 0.1 M H_2SO_4.* ***d)*** *Cathode catalyst layer of an MEA operated with 0.1 M H_2SO_4.*

After an operation time of 48 h at 2 A mg_{Ir}^{-1} the differences between both systems become even more evident. Figure 5.10 shows *post mortem* STEM cross-section micrographs of both systems. The corresponding SEM-EDX analyses of the marked spectra are shown in table 5.1. The anode catalyst layer of the DI water operated system, shown in figure 5.10 a), after two days, is virtually intact. No migration of particles is visible in the micrograph. On the other hand, the anode catalyst layer of the acidified system, as shown in figure 5.10 c), displays stark signs of degradation. Not only have Au particles from the bipolar plates migrated into the membrane close to the anode side, but the anode catalyst layer itself appears to have lost parts of its structure.

On the cathode sides, a discrepancy is observed as well. The cathode side of the conventional MEA contains only carbon and platinum as a pristine cathode. The cathode of the acidified MEA, on the other hand, shows significant amounts of iridium, and in the vicinities of the cathode catalyst layer, even large amounts of titanium have deposited.

Another evidence that the acidification of the MEA indeed leads to a pH shift in the OER at the anode side are the polarization curves of the MEA system. Polarization curves of both the conventional and the acidified MEA are displayed in figure 5.11 a). According to the Nernst-Equation 2.6, the potential of an electrode at which the OER takes place shifts by 0.059 × pH against the SHE. At a given current density, the water flow proton concentration and hydrogen pressure in an MEA system can be assumed as constant, shown in experiments as well [79]. Therefore the changes in the onset potential between both systems can be related to a pH change in the catalyst layer. The onset of the acidified MEA is shifted by around 120 mV, which would correspond to a pH shift of 2. Although the difference at higher current densities is significantly higher, it has to be noted that OER can take place at other parts of the system when electrolytic contact is made. Therefore these measurements can only serve as indication.

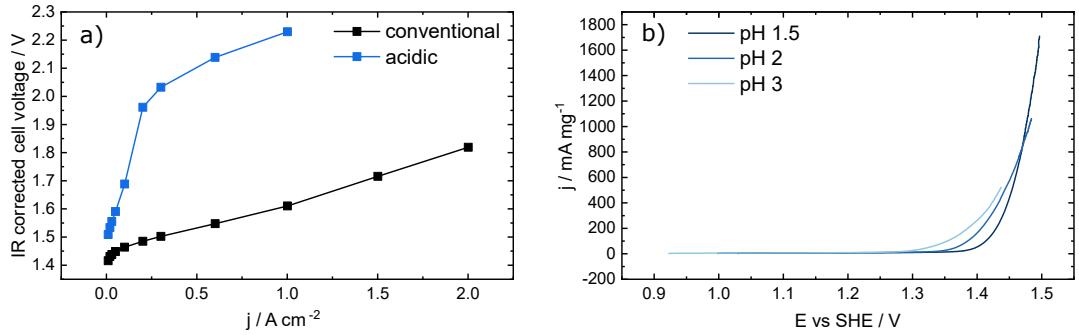

Figure 5.11: Changes in activity with changed pH in AMS and MEA. a) *post-mortem iR-drop corrected polarization curves in the GR-free MEA setup with anode catalyst loadings of* $1\,\mu g_{Ir}\,cm^{-2}$ *operated with DI water and 0.1 M* H_2SO_4*, respectively.* ***b)*** *iR-drop corrected LSV with* $5\,mV\,s^{-1}$ *of* IrO_x *catalysts spots in varying electrolyte pH.*

For further reference, iR-drop corrected polarization curves of IrO_x in SFC are shown in figure 5.11 b). According to the difference between MEAs, a potential shift against the SHE is visible.

5.2.5 System breakdown of the dissolution discrepancy between AMS and MEA

A breakdown of the shown results into single factors reveals the differences between AMS and MEA. As shown in figure 5.12, the discrepancy between both systems

	Ir		Au		Pt		Ti		C		F		O	
	wt%	σ	wt%	σ	wt%	σ	wt%	σ	wt%	σ	wt%	σ	wt%	σ
Spectrum 1	52.6	1.1							25.2	0.9	8.7	0.5	13.5	0.6
Spectrum 2	10.9	1.5							52.4	1.4	32.8	1.2	3.9	0.7
Spectrum 3	1.9	0.7							55.0	1.0	42.1	0.9	1.0	0.5
Spectrum 4	0.8	1.5			0.0	0.4			47.1	1.2	39.6	1.1	12.5	0.9
Spectrum 5	1.8	1.3			0.0	0.5			51.0	1.0	34.4	0.9	12.7	0.8
Spectrum 6	0.0	1.1			7.5	0.5			67.1	0.9	13.9	0.6	11.5	0.7
Spectrum 7	41.3	1.9	8.1	1.6	0.9	1.3	0.1	0.1	31.3	1.5	1.6	0.6	16.6	1.1
Spectrum 8	1.7	1.5	0.0	0.9	0.1	0.8	0.0	0.1	63.8	2.3	30.5	1.9	3.8	1.5
Spectrum 9	0.0	0.6	58.1	0.5	0.0	0.5	0.0	0.6	29.9	0.5	8.8	0.3	3.3	0.3
Spectrum 10	0.6	0.8	9.0	0.8	0.0	0.1	0.0	0.6	60.0	1.3	27.6	1.0	2.4	0.7
Spectrum 11	15.8	2.0	1.0	1.0	0.2	0.8	0.2	0.2	54.6	2.0	26.7	1.4	1.6	1.0
Spectrum 12	6.7	1.4	0.0	0.7	0.1	0.6	5.4	0.3	45.1	1.5	35.4	1.3	7.3	1.1
Spectrum 13	7.5	1.2	0.0	0.6	0.3	0.5	17.3	0.6	15.3	1.1	20.4	1.2	39.2	1.3
Spectrum 14	11.2	1.2	0.0	0.9	13.6	0.7	1.4	0.2	55.7	1.2	8.8	0.6	9.2	0.8

Table 5.1: *STEM-EDX results for the spectra marked in figure 5.10*

decreases to less than an order of magnitude if DI water in the anode water cycle is exchanged by 0.1 M H_2SO_4 (1), (2). The still existing difference can not be related to a single factor. Differences in loading, mass transport conditions, and dissolved species in the electrolyte might play a small role here, which can neither be proven nor disproven by the experimental design. The different degree of complexity of both systems hinders conclusions on a main contributor. The S-number of an MEA, operated with DI water, exceeds the S-number of the MEA operated with diluted acid on the same timescale of 2 h by two orders of magnitude (3). This finding indicates that a pH shift between AMS and MEA under standard conditions is one of the main contributors to the dissolution discrepancy. After a longer timescale of two weeks of operation, the S-number of the MEA increases by another order of magnitude (4). At this larger timescale, lifetime calculations from S-numbers in the AMS suggest that the same catalyst would have already fully degraded in an aqueous acidic environment. Therefore, a stabilization on a larger timescale can be seen as a second large contributor to the dissolution discrepancy.

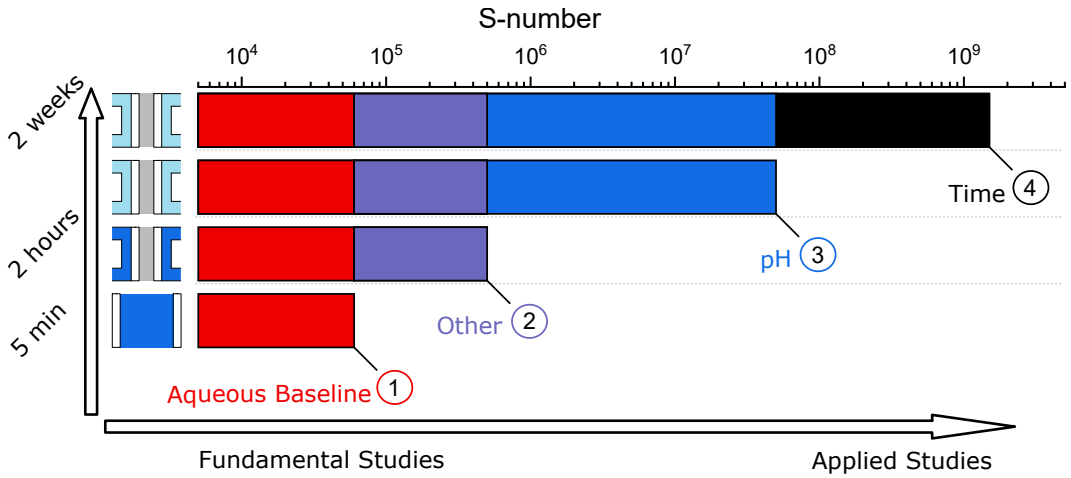

Figure 5.12: Breakdown of the factors contributing to the OER catalyst dissolution discrepancies between AMS and MEA. *The AMS exhibits S-numbers of 6×10^4* ***(1)****. If the MEA is operated with acidic electrolyte instead of DI water, the S-number of the PEM-system decreases to 4×10^5. The remaining difference can not be related to single factors in this study* ***(2)****. Various factors like flow rate, Nafion content, and timescale could be responsible. The S-number of an MEA operated with DI water in the same timeframe of 2 h, however, increases by almost two orders of magnitude* ***(3)****. This difference can be accounted to a shift in pH in the system. On a longer operation timescale of two weeks, a further increased dissolution stability of iridium in the MEA is observed* ***(4)****.*

As STEM-EDX detects only tiny amounts of iridium in the membrane in close proximity to the anode catalyst layer, it is unlikely that the difference in dissolution

deposes in the membrane instead.

In the bigger picture, the aforementioned results indicate inconsistencies regarding local pH in MEA operation. It is generally accepted that the anode catalyst layer of an MEA operates under highly acidic conditions due to the protons, which are formed in the OER. On the other hand, actual data on proton activity in MEA is scarce. In a review from 2013, Carmo et al. estimated that MEA operation takes place around pH 2 [33]. Later published results from measurements of pH in the anode water cycle of an MEA system report values in a range of pH 5.6 to pH 3.5 [180].
Although the pH in the anode water cycle is not representative of the local pH in the anode catalyst layer, as local pH decreases due to proton generation in the OER, these results indicate that pH values in the literature might have been gravely underestimated up to this point.
Therefore, future research should focus more on two points two water splitting devices: the actual conditions in the anode catalyst layer and effects in the catalyst/membrane interface, which might lead to some stabilization.

5.2.6 Comparison of dissolution stability in AMS and MEA of different OER catalysts

Given the previous results, it is comprehensible that stability measurements in AMS can not reflect on stability estimations in MEA. However, due to the fast degradation of OER catalysts in AMS, the aqueous system might serve as the ideal system for ASTs of OER catalysts.
Four different OER catalysts, namely, the already used IrO_x, Umicore Elyst (IrO_2 on TiO_2), Heraeus iridium black (metallic Ir powder) and RuO_2 were tested in both AMS and MEA with the same protocols as other measurements in this chapter. The S-numbers of the 30 s interval toward the end of a 5 min hold at $100\,\mathrm{mA\,mg_{Ir}^{-1}}$ in AMS and after 1 h of $2\,\mathrm{A\,cm^{-2}}$ are displayed in figure 5.13.

Although the S-numbers in AMS are significantly lower than the S-numbers of their MEA counterparts, the results are qualitatively identical in both systems. In both systems, the Umicore Elyst catalyst appears to be the most stable, followed by IrO_x, Ir black, and RuO_2 in the end. Based on these results, a utilization of AMS as AST for catalyst stability in MEA would be highly recommendable.
However, on a longer timescale, the differences virtually vanish. Figure 5.14 shows S-numbers of the two more stable catalysts, IrO_x and Umicore Elyst, as a function of time. A similar experiment with Ir black showed a similar trend but lacks data quality due to power failures.

While the S-numbers of the more crystalline Umicore Elyst catalyst rise to a level of 10^9 very fast at the beginning of the experiment, the S-numbers of the IrO_x catalyst rise slower, but reach, after several hours of measurement, the same value

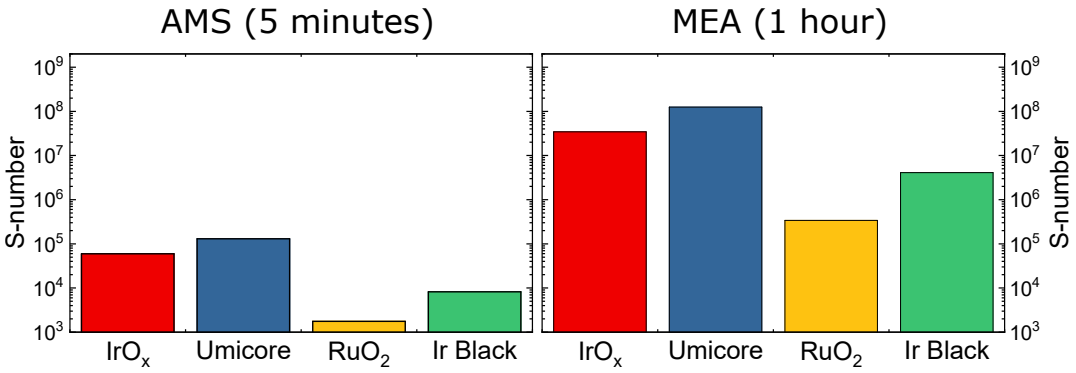

Figure 5.13: Comparison of S-numbers of different OER catalysts in AMS and MEA.

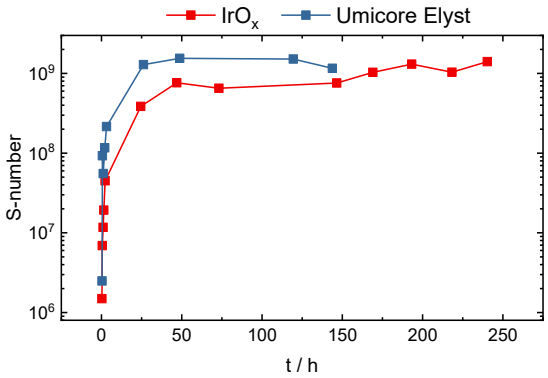

Figure 5.14: S-numbers of two catalysts, IrO_x and Umicore Elyst, in MEA as a function of time.

of 10^9.
The S-number of different OER catalysts suggests that iridium-based catalysts of similar crystallinity exhibit similar S-numbers [38]. Furthermore, it was shown that iridium crystallizes under extended time in OER conditions [76].
Extrapolated to the results of different catalysts in MEA, it appears that the oxidative conditions at a current density of $2\,\mathrm{A\,cm^{-2}}$ leave all iridium-based catalysts in the same oxidative state after a longer timescale. The differences measured in AMS appear to be equalized on this timescale.

5.3 Conclusions

In this chapter, the stability discrepancy between AMS and MEA was confirmed experimentally. The results show that stability measurements in AMS have to be treated very carefully regarding their relevance for stability in MEA environment. The main contributors to this discrepancy were identified to be a stabilization of OER catalysts in MEA on a longer timescale and an overestimated acidity in the MEA environment of the Nafion® membrane.
Although, results of different catalysts on a short timescale of MEA operation predict AMS to be an ideal AST for real-world application, it appears that the

oxidative potential in MEA leads to an alignment of the oxidative state in iridium-based catalysts and thus, their stability on a larger timescale.
The results in this chapter suggest that the process of testing OER catalysts for PEMWE application in aqueous model systems should be critically evaluated. Also, utilization of AMS as AST for PEMWE appears to be ineffective, as only small timescales, not relevant for real application, align between both systems.
Instead, the focus should be shifted to evaluate OER catalysts in MEA environment directly. A GR-free setup, coupled to downstream analytics such as ICP-MS, would allow more profound insights into the stability of PEMWE during dynamic operation, which is relevant for coupling it to intermittent solar energy.

6 System Development - A Photoelectrochemical Scanning Flow Cell

6.1 Initial Considerations

The SFC-ICP-MS has been proven invaluable in studies of electrocatalyst stability. Hence, to photoelectrochemical catalysts, a photoelectrochemical scanning flow cell (PEC-SFC) was developed to transfer the method for stability evaluations of photoelectrocatalysts. The main difference of the novel system is a light source introduced in the cell. To develop the photoelectrochemical scanning flow cell coupled to an ICP-MS (PEC-ICP-MS) the following design criteria had to be taken into account.

1. Easy setup and dismantling process to use within the existing SFC setups
2. Light source with a defined output intensity as well as the possibility to avoid stray light from the laboratory.
3. Closed cell design to avoid leakage
4. Option to calibrate power of the light source

The first design criterium was rather practical. As the SFC setups were shared by users, a clean and easy assembly and disassembly of the new cell and the optical parts was desired. The other criteria were based on scientific considerations.

6.2 Light Source

High-throughput flow cells for photoelectrochemical measurements have been demonstrated in the past [181–183]. Most of the earlier measurements were performed with monochromatic light-emitting diode (LED) light sources. In all cases, front light illumination by an optical fiber cable directing light from the light source to the cell was chosen. As this front light illumination setup had been proven to produce good results, a similar concept was targeted.

As a light source for the photoelectrochemical setup, a monochromatic LED with a wavelength of 385 nm (Thorlabs M385F1) was chosen. It was controlled by an LED-driver (Thorlabs DC2200) with an output current range between 0 mA to 700 mA. The light was directed from the LED to the cell by an optical fiber patch cable with a core diameter of 400 µm. A standard SMA connector was used to connect the optical fiber to the light source, whereas a ceramic ferrule with 1.25 mm diameter was connecting the other end of the optical fiber to the cell. The ceramic ferrule was used, as it has to be resistive against corrosion by electrolytes used for photoelectrochemical (PEC) measurements.

6.3 Cell design

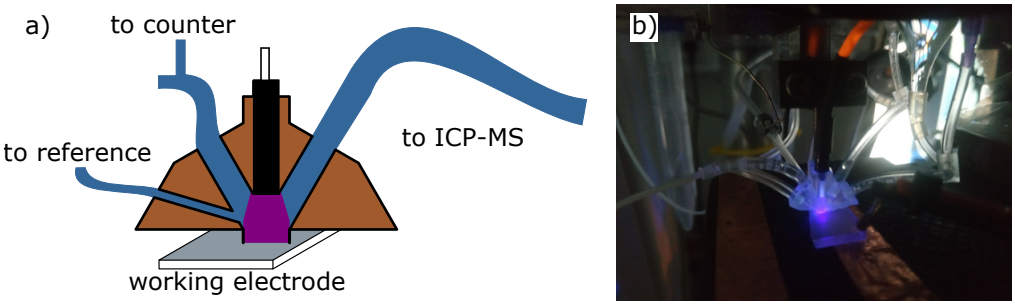

Figure 6.1: Photoelectrochemical scanning flow cell a) *Schematical drawing of the SFC* ***b)*** *Photo of the operational PEC-SFC. In contrary to the cell used for measurements, the cell in the photo was milled from a polycarbonate (PC) block for demonstrative purpose*

The cell design was adapted from the gas evolution optimized SFC, which was shown in section 4.1.1. A hole slightly larger than the diameter of the ceramic ferrule was drilled in the top. The dimension of the pocket around the hole were chosen such that the end of the ferule was as flush with the electrolyte channels as possible to provide turbulences caused by a pocket in the cell. The top of the ferrule was sealed with the cell with two-component silicone glue to prevent leakage and exchange with air from outside.
The cell was milled with a CNC milling machine from a block of non-transparent polyether ether ketone (PEEK) to block light from the laboratory. The same silicone ring as for the normal SFC was glued to the opening to prevent spillage on the working electrode A CAD drawing of the photoelectrochemical cell is shown in figure 6.1 a) and a photo of an operational cell milled from transparent PC for demonstrational purpose is shown in 6.1 b).

6.4 Calibration

To enable comparability of photoelectrochemical data, it is vital to know the light intensity, which illuminates the electrode. The light intensity in the unit W cm^{-2} is a descriptor of the power from incident light that hits a specific area. In standard AM 1.5g photoelectrochemical setups, this intensity calibration is usually performed with a solar cell, calibrated for the spectrum. This method is sufficient if the diameter of the incident light beam is substantially larger than the area of the solar cell and the electrode. For a setup like the presented, a precise measurement of both, LED power and illuminated area is mandatory to ensure precise measurements and comparability to literature values. Both, the LED power output P and the illuminated area A are determined separately. The intensity I is calculated by $I = \frac{P}{A}$.

6.4.1 LED power output

Light intensity is measured with a photodiode sensor (Thorlabs S120VC) connected to a USB power and energy meter interface (Thorlabs PM100USB). The photodiode sensor is a single-channel silicon detector. It measures the number of photons in a given time frame. For this measurement, the assumption that all photons reaching the detector have the same wavelength λ is made.
The area of the power meter is significantly larger than the opening of the cell. Thus, all photons that exit the cell will be captured by the detector. To measure the power output, the power sensor was covered with a quartz glass slide and brought into contact with the cell opening. The LED was operated subsequently at increasing input current, and the resulting power output was measured. LED

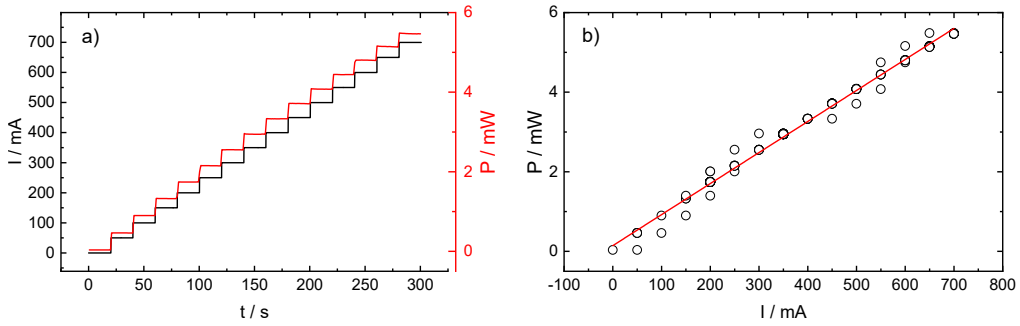

Figure 6.2: Exemplary data of the current to power calibration process of the PEC-SFC a) *LED input current (black) and measured LED power (red) as a function of time.* ***b)*** *measured LED power as a function of LED input current (black circles) and linear fit of the data (red line). Note: although the method produces visible outliers, the quality of the fit is* $R^2 > 0.99$.

input currents and resulting measured power outputs are shown in figure 6.2 a).

The measured power increases linearly alongside the LED input current. It is important to note that the power reading without light from the LED was negligible. Therefore, no correction for background illumination of the laboratory had to be performed.
To calibrate the power output to the input current, both measurements were synchronized with a python script, and the power output was treated as a function of input current. Results of this procedure are shown in figure 6.2 b). Although the analysis method produces visible outliers at the beginning and end of intensity steps, the points on the main regression line consist of around 2000 data points due to a high sampling rate. Therefore the outliers do not have a significant influence on the calibration result.

6.4.2 Illuminated Area

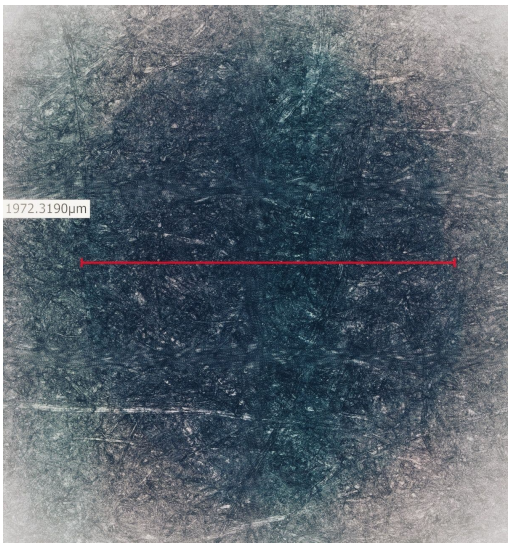

Figure 6.3: Spot of the area illuminated by the LED from the cell opening on solar photo paper. *The area is determined by a measurement with the laser microscope*

The size of the illuminated area below the cell was measured with UV-sensitive paper (Astromedia Solar-Photopapier). The cell was placed on the UV-sensitive paper separated from the electrolyte by a transparent plastic foil. The LED was afterward operated at maximal input current for 1 min. After this procedure, the paper was developed according to the manual and the size of the resulting elliptical spot (4.5 mm^2) was determined with the laser microscope. The developed photo paper is shown in figure 6.3.

7 Proof of Concept: Dissolution of WO_3 Photoanodes in Acidic Electrolyte

Parts of the following study were published under the title:
"Time-resolved analysis of dissolution phenomena in photoelectrochemistry - A case study of WO_3 photocorrosion"[184]
Julius Knöppel, as first author, developed the photoelectrochemical scanning flow cell, prepared samples, performed PEC-ICP-MS measurements and data analysis, and took part in the writing process of the manuscript.

7.1 Introduction

In the previous chapter, the development of a PEC-ICP-MS system from the previously existing SFC-ICP-MS system was shown.
To test the capabilities and limitations of the new system WO_3 photoelectrodes on an Au backing electrode are prepared as a proof of concept model system. The degradation behavior of the model system is observed under varying electrochemical potential and illumination intensity.

7.2 Results and Discussion

The synthesis of the WO_3 photoelectrodes on Au used in this study is described in section 4.3.1. The electrodes have a diameter of 1.3 mm and a thickness of 1.5 µm as determined by laser profilometry. An exemplary microscopic image is shown in figure 7.1 a). The 3D profile of the same spot is shown in figure 7.1 b).

Estimated from the nominal loading and the theoretical loading of a compact electrode with the same dimensions, the porosity of the electrode is around 30 %.

An overview of WO_3 and Au dissolution measured in the PEC-ICP-MS setup is shown in figure 7.2. Dark and illuminated (385 nm, 57 mW cm^{-2}) ramps are

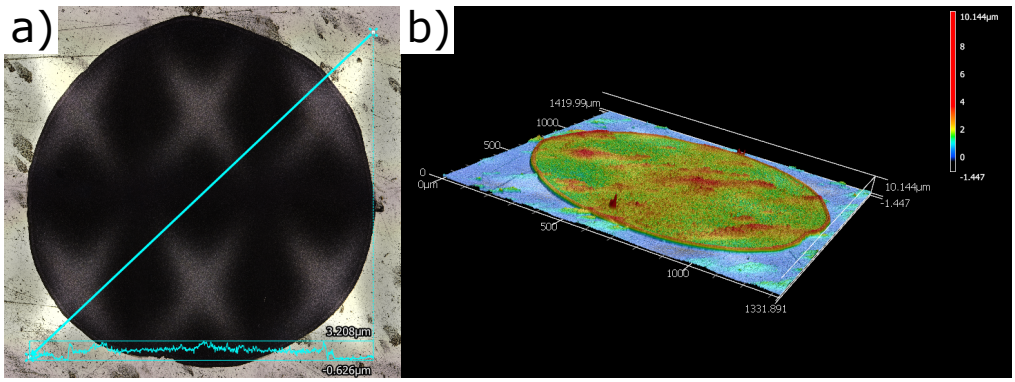

Figure 7.1: Images from laser profilometry of the WO_3 on Au photoelectrodes ***a)*** *Light microscope image with a cross-sectional profile* ***b)*** *3D image of the spot with surface profile.*

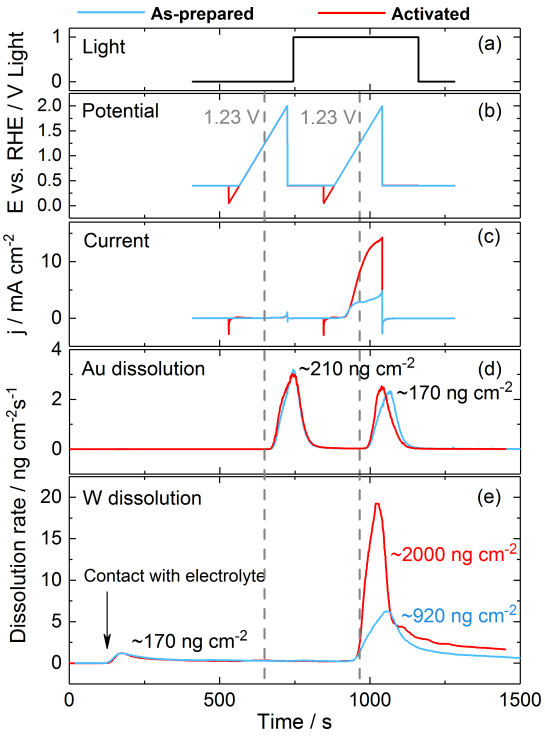

Figure 7.2: Photocurrent and dissolution of WO_3 on Au photoelectrodes during dark and illuminated ($57\,mW\,cm^{-2}$) LSVs from $0.4\,V_{RHE}$ to $2.0\,V_{RHE}$ ***a)*** *Applied light profile.* ***b)*** *Applied potential profile.* ***c)*** *Photocurrent response.* ***d),e)*** *Dissolution rates of Au and W from WO_3 as a function of incident light and potential.*

measured in a broad potential window to study the effect of potential on photocurrents and dissolution. Two kinds of ramps are used in these experiments. One is started from the contact potential of $0.4\,V_{RHE}$, where WO_3 is thermodynamically stable. The other ramp starts with a potential step from $0.4\,V_{RHE}$ to $0.05\,V_{RHE}$ to partially reduce the electrodes electrochemically. Both ramps end at $2.0\,V_{RHE}$ with a potential step back to $0.4\,V_{RHE}$. The ramps were first done light-off and afterward light-on, as shown in figure 7.2 a) and b). The photocurrent response is shown in figure 7.2 c). Photocurrents in both protocols are negligible during the dark ramp. This indicates that no faradaic processes take place. The small peaks around $2.0\,V_{RHE}$ can be attributed to OER on gold [185]. The negative cur-

rent, which can be seen in the pre-treated sample, can most likely be attributed to oxygen, reducing on the Au backing electrode surface. The OER which takes place on the backing electrode leads to severe gold dissolution, as shown in figure 7.2. During the ramp 210 ng cm^{-2} of gold dissolve, which corresponds to half a monolayer and is in line with previous works [185]. W dissolution, on the other hand, is negligible during the dark ramp. A small visible peak that is below the detection limit of the ICP-MS can most likely be attributed to dissolution of defect states on the surface.

Photocurrents of up to 15 mA cm^{-2} are observed, during a LSV under illumination - a strong contrast to the observed dark currents. Compared to previous work, the photocurrents are higher, which is plausible, as WO_3 has its bandgap in the range of 2.6 eV to 2.7 eV and thus absorbs mostly light in the UV range [186–190]. Thus only a fraction of the 100 mW cm^{-2} intensity of the AM 1.5G spectrum is absorbed and converted to photocurrent in other studies.
With increasing photocurrent, WO_3 starts to dissolve massivly. At the thermodynamic water splitting potential of 1.23 V_{RHE} dissolution rates of 1 ng cm^{-2} s^{-1} to 2 ng cm^{-2} s^{-1} are observed. Due to the strong tailing of dissolution peaks, the actual values are supposedly higher. The maximal dissolution rate of W is around 20 ng cm^{-2} s^{-1}. After the potential step back to 0.4 V_{RHE}, the dissolution rate decays. The total amount of dissolved tungsten during the linear sweep is 2000 ng cm^{-2}. Taking the electrode's total WO_3 loading of 540 µg cm^{-2} into account, one can conclude that during one LSV 0.37 % of the electrodes dissolve. The dissolution of Au, on the other hand, is virtually unchanged. The slight decrease can be accounted to electrode history. The comparison between the pristine and the pre-treated electrode shows that PEC activity and PEC WO_3 dissolution are correlated, a phenomenon well known from classical electrocatalysis [191]. In the following, the variable power output of the LED is utilized to investigate this phenomenon more closely.

The photocurrents dependency of the intensity of the light source as well as the resulting WO_3 and Au dissolution are shown in figure 7.3. The intensity was doubled step-wise from 0.0 mW cm^{-2} to 112 mW cm^{-2}. The electrode potential was pulsed from 0.4 V_{RHE} to 1.23 V_{RHE} during light-off and light-on phases, as shown in figure 7.3 a). As shown in figure 7.3 b), the increase of light intensity is accompanied by a proportional photocurrent response. At light intensities of > 100 mW cm^{-2}, photocurrent responses of $j > 10$ mA cm^{-2} are observed. The resulting dissolution profiles of W and Au are presented in figure 7.3 c). The W dissolution profile follows a trend similar to the one observed in photocurrent response. The dissolution profile of Au, on the other hand, is dominated by the tailing of the dissolution peak induced by the initial ramp to 2.0 V_{RHE}. Other than that, the dissolution of gold is negligibly small.
The amount of dissolved W as a function of total transferred charge during the individual potential and light pulses is shown in figure 7.3 d). The first is obtained

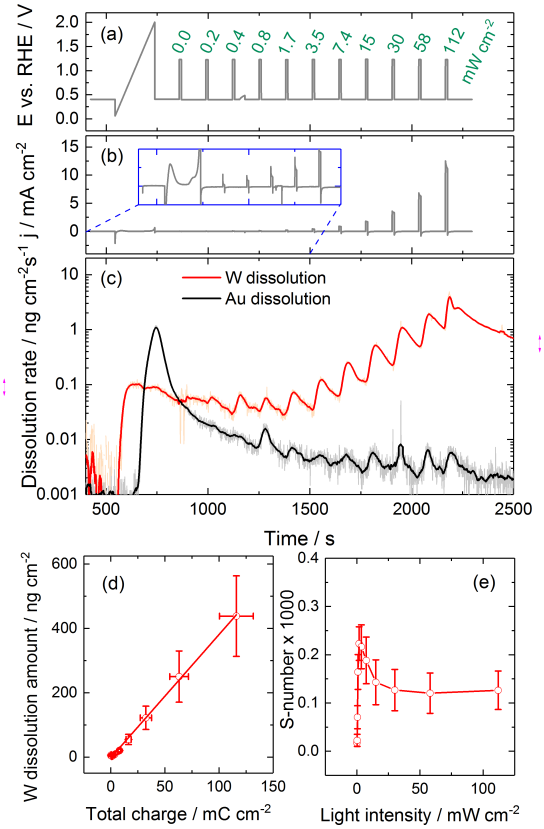

Figure 7.3: Influence of light intensity on W and Au dissolution. ***a)*** *Applied potential profile. The potential steps to 1.23 V_{RHE} are labeled with the incident light intensity in $mW\,cm^{-2}$.* ***b)*** *Resulting changes in photocurrent.* ***c)*** *Resulting W and Au dissolution. The background signal from the W signal was extracted.* ***d)*** *Dependency of dissolved W amount on the total transferred charge during the potential step.* ***e)*** *Stability numbers of WO_3 for different light intensities with dissolution and charge taken from c) and d). All error bars were calculated from 3 independent measurements.*

by integrating the dissolution peaks in figure 7.3 c), and the latter is obtained by integrating the current peaks from figure 7.3 b). The results show a linear correlation, similar to relations shown earlier in OER electrocatalysis for Au and Ir-based electrocatalysts [38, 192]. In electrocatalysis research, this relation is typically attributed to a common intermediate between OER and catalyst dissolution.
To compare WO_3 stability to other catalytic materials, S-numbers are calculated for each light pulse and displayed in figure 7.3 e). Although OER might not be the dominant reaction occurring on the photoelectrodes, it provides a useful metric to compare the stability of applied materials. Under the applied conditions, S-numbers of WO_3 are between 100 to 200. This indicates very limited stability, especially in comparison to iridium in aqueous or MEA systems as shown in chapter 5. A series of measurements with a constant light intensity of 57 $mW\,cm^{-2}$ and potential pulses from 0.4 V_{RHE} to 1.23 V_{RHE}, shown in figure 7.4, reveals almost identical dissolution behavior throughout the protocol, indicating that the high dissolution rates are not related to defect states which have dissolved after the first cycle but to dissolution of the electrode bulk.

Due to its limited stability, WO_3 photoelectrodes can not be recommended for practical applications under the investigated conditions. However, the conditions in the PEC-SFC might differ strongly from those in real devices for hydrogen production as there is a flow of electrolyte in the cell, which might enhance dissolution due to changes in the chemical equilibrium. In devices with stagnant conditions,

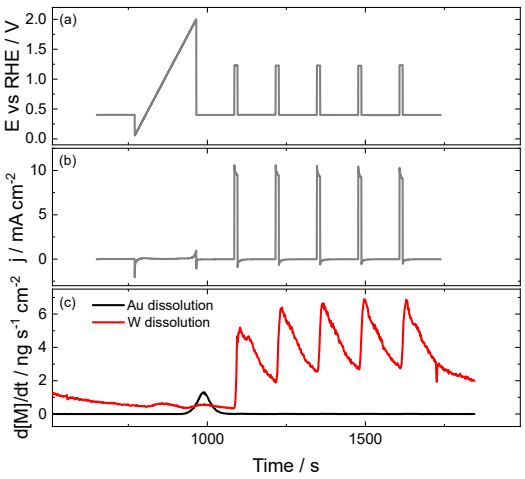

Figure 7.4: Influence of repeated light pulses ($57\,mW\,cm^{-2}$) on W and Au dissolution. ***a)*** *Applied potential profile.* ***b)*** *Resulting changes in photocurrent.* ***c)*** *Resulting W and Au dissolution.*

better stability might be acquired.
The limited stability of WO_3 photoanodes can not be explained by thermodynamics. At anodic potentials with pH$<$ 4, WO_3 is the only stable species [60]. However, thermodynamic estimations are only made in electrolytes containing H^+ or OH^- species without counterions. In reality, counterions, such as ${SO_4}^{2-}$, ${ClO_4}^-$ or Cl^- can form stable complexes with tungsten intermediate states that might be more stable than WO_3, and thus lead to measured dissolution in the ICP-MS.
As tungsten is known for its strong complexing affinity, such complexes are typically considered in theoretical works on photocorrosion thermodynamics [151, 193]. Therefore the classical view of Pourbaix diagrams for estimation of stability has to be expanded to common counterions present in photoelectrochemical systems. In the case of WO_3 in sulfuric acid, complexation of tungsten with ${SO_4}^{2-}$ or ${S_2O_8}^-$, which are known to form in PEC water splitting [194–199] have to be considered. Also, subsequently, it has to be studied if the wavelength of the incident light affects stability.

7.3 Conclusions

The results in this chapter demonstrate that degradation studies in photoelectrochemistry can be effectively supported by the newly developed PEC-ICP-MS. With this novel technique, it was shown that WO_3, a material that, according to the literature, is thermodynamically stable under operating conditions exhibits severe dissolution in acidic electrolyte under operation. Furthermore, it was shown that the amount of dissolved tungsten is proportional to the charge transferred at the electrode. This indicates that a common intermediate between WO_3 dissolution and OER exists, or other reactions at the photoanode take place. WO_3 can not be recommended as photoanode material for application in the studied conditions, based on these results. Further studies cover the effect of the used electrolyte and

the influence of iridium as co-catalyst on the WO_3 surface on ceWO3 stability, and are shown in Chapters 8 and 9.

8 WO_3 photoanode stability in different electrolytes

Parts of the following study were published under the title: "Photocorrosion of WO_3 in different electrolytes" [200].
Julius Knöppel, as the first author, designed the experiments, prepared the precursor, performed PEC-ICP-MS measurements, data analysis, and wrote the original draft of the manuscript.

8.1 Introduction

Within the thermodynamic model, shown in figure 3.6, WO_3 belongs to the second category. Its decomposition potential lies above the valence band and below the thermodynamic water splitting potential. Thus, if only thermodynamics were to be considered, it should be stable. However, as the results shown in the previous chapter verify, the thermodynamic view on stability alone is insufficient. Severe dissolution of WO_3 photoanodes was shown, demonstrating a kinetic competition between the reaction at the photoanode and photoanode decomposition [41, 151, 201].
Furthermore, the decomposition potential of the photoanode should depend on the electrolyte, especially, if there are reactions between the electrode and products of electrolyte decomposition.
In this chapter, the findings from the previous chapter are extended by investigating the influence of different electrolytes on the operational stability of WO_3 photoanodes under operation in different electrolytes that are widely used in the community. The results are discussed in light of the reported behavior of WO_3 photoanodes in these electrolytes, such as photoactivity and selectivity. It is shown that, in addition to photoelectrode materials, electrode/electrolyte combinations have to be studied to construct a stable photoelectrochemical device.

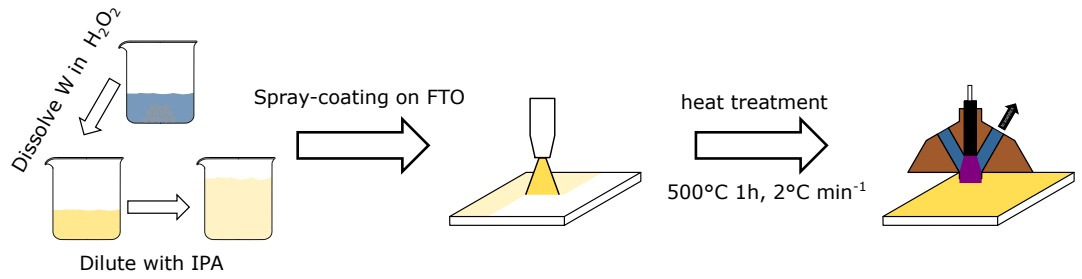

Figure 8.1: Synthesis scheme for WO_3 thin films. *For precursor synthesis, W powder is dissolved in H_2O_2 and subsequently diluted with IPA. The precursor is spray-coated on FTO-coated glass slides and calcinated. After calcination, the samples are measured in a photoelectrochemical scanning flow cell coupled to an ICP-MS.*

8.2 Results and Discussion

8.2.1 Synthesis and Charakterization of WO_3 thin films

WO_3 films were synthesized by a novel spray-coating approach from a precursor synthesized on well-established peroxotungstic acid routes [146, 150, 167]. A scheme of the synthesis process is shown in figure 8.1. First, W powder was dissolved in concentrated H_2O_2. After full dissolution of W, resulting in a light yellow solution, excess H_2O_2 was removed by heating the solution. The precursor was diluted with IPA and used as an ink in the spray-coating process. To form thin-film electrodes, the precursor was sprayed onto FTO coated glass slides and calcinated at 500 °C afterward. The photoelectrodes area was 6.25 cm^2, but the method is suitable to prepare electrodes of arbitrary size.

After calcination, the films appear to have a uniform yellow surface. Structural analysis by XRD, as shown in Figure 8.2 a), reveals a crystalline structure that matches literature values of WO_3 obtained from the crystallography open database [202]. The optoelectronic properties of the films were studied using UV-vis spectroscopy, as shown in Figure 8.2 b). For an estimation of the bandgap, Tauc analysis, shown in Figure 8.2 c), was performed on the UV-vis spectrum. It reveals an indirect transition with a bandgap of 2.65 eV. This value is in good agreement with literature data [187–190].

The morphology and thickness of the WO_3 thin films were studied with SEM and are presented in Figure 8.2. Top-view imaging, as shown in figure 8.2 d), reveals a porous structure. The average pore size is around 100 nm. SEM liftouts, as shown in Figure 8.2 e), show a film thickness between 2 µm to 3 µm.

The variety of structural features of WO_3 electrodes in the literature is wide. WO_3 electrodes, synthesized from a microwave-assisted sol-gel route, and electrodes, synthesized from commercial nanoparticles, were around 3 µm thick and showed

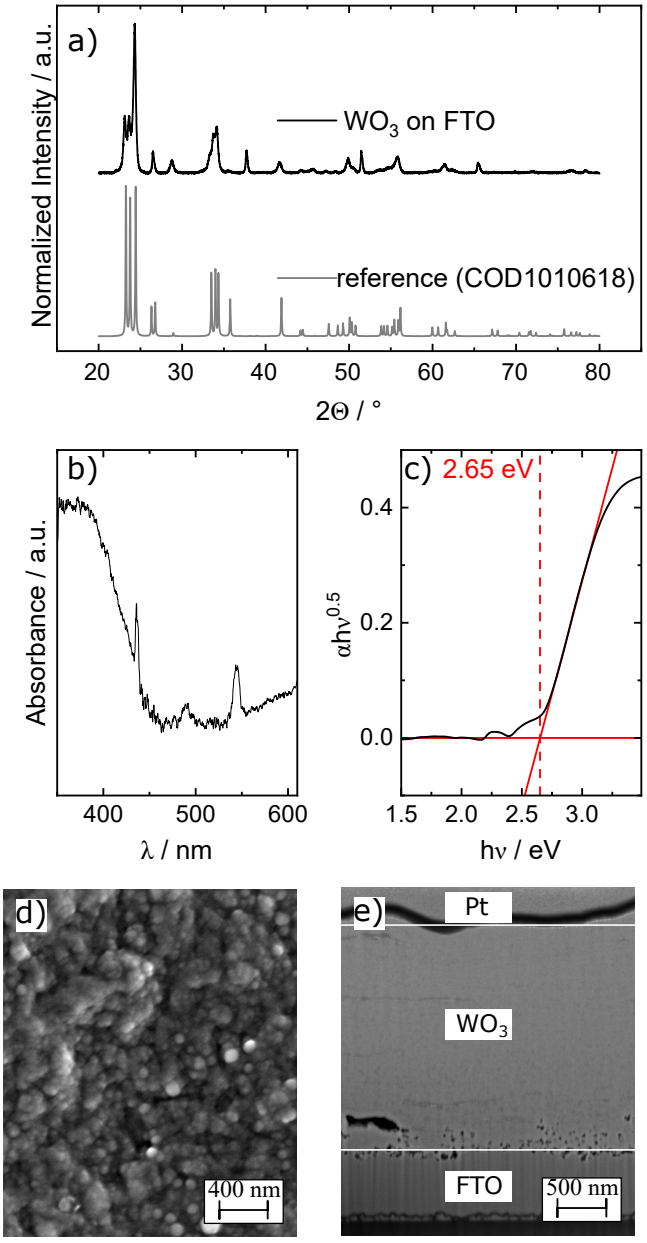

Figure 8.2: Characterization of WO_3 thin films. ***a)*** *XRD spectrum of WO_3 thin films with a reference spectrum from the open crystallography database [202].* ***b)*** *Absorption spectrum of WO_3 thin film.* ***c)*** *Baseline-corrected Tauc plot analysis. The data shows an indirect transition with a bandgap of 2.65 eV.* ***d)*** *SEM micrograph of WO_3 thin film.* ***e)*** *SEM micrograph of a WO_3 thin film liftout. The Pt layer was applied to protect the film during the liftout. The distance between the white lines is $\approx 2.3\,\mu$m.*

higher porosity [195, 203]. Nanoparticles, synthesized from an aqueous sol-gel route, show a more compact structure and an electrode thickness of around 2.5 µm [198]. Thus, the thickness and structure of the electrodes used in this study are in the same ballpark as previous reports.

8.2.2 Photoelectrochemical activity of WO_3 thin films in different electrolytes

The photoelectrochemical activity of the previously synthesized WO_3 films was measured in four different electrolytes, sulfuric acid, perchloric acid, nitric acid,

and methanesulfonic acid, at a concentration of 0.1 M in aqueous solution. To determine the photoelectrochemical activity, LSVs from 0.4 V_{RHE} to 1.5 V_{RHE} with a scan rate of 10 mV s^{-1} were recorded in the dark and under constant illumination by a UV-LED with $\lambda = 385$ nm at an intensity of 50 mW cm^{-2}. The results are presented in figure 8.3.

While the dark currents are negligible, the currents increase significantly under

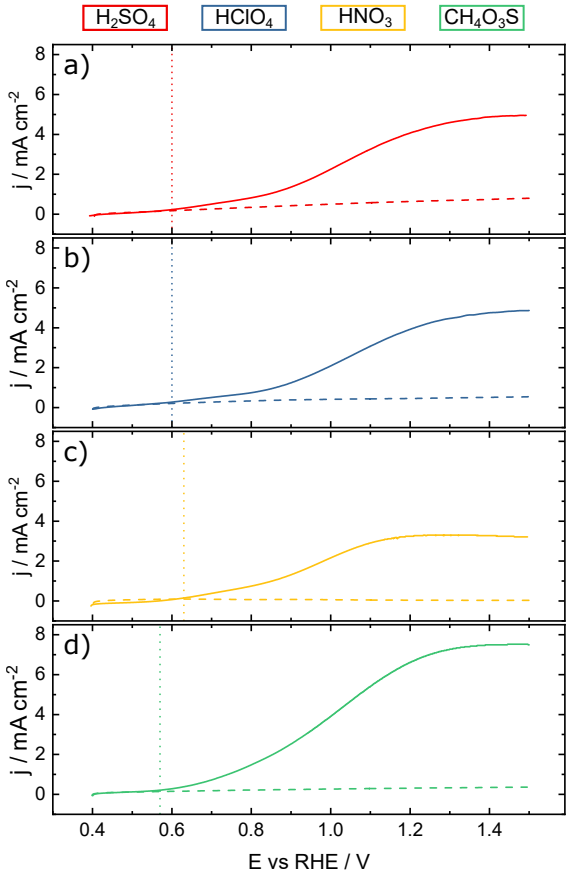

Figure 8.3: Photoelectrochemical behavior of WO_3 thin films. *Dark and illuminated (50 mW cm^{-2} at 385 nm) ramps were recorded in* ***a)*** *sulfuric acid* ***b)*** *perchloric acid* ***c)*** *nitric acid and* ***d)*** *methanesulfonic acid. The dashed vertical lines indicate the onset potential of the illuminated ramp.*

illumination. The WO_3 thin-films show here limiting photocurrents in a range from 3 mA cm^{-2} in nitric acid up to 8 mA cm^{-2} in methanesulfonic acid. These limiting photocurrents exceed those shown for WO_3 in the literature by a factor of around 2.5 [195–198, 204]. This discrepancy can be explained by the differences in the light sources. Typically, an AM1.5G solar simulator at 1 sun (100 mW cm^{-2}) illumination intensity is utilized. This work features a UV light source ($\lambda_{mean} = 385$ nm) at 50 mW cm^{-2}. As the absorption of WO_3 is strongest in the UV spectrum, as the utilized light source, the lower monochromatic intensity used in this study leads to higher limiting photocurrents.

Besides the higher activity, the films show trends similar to the literature regarding activity between electrolytes. The trend in onset potentials $E^{on}(CH_4SO_3) < E^{on}(H_2SO_4) \approx E^{on}(HClO_4) < E^{on}(HNO_3)$ is inversely proportional to the trend of limiting photocurrents. This shift in onset potential is consistent with the literature [197]. Both the shift in onset potentials and the shift in limiting photocurrent indicate that water oxidation is not the kinetically limiting charge transfer reaction at

the WO_3 surface. Indeed, previous studies have already shown that various electrolyte anions, which are typically considered inert, can decompose due to charge transfer reaction by photogenerated holes at WO_3 surfaces [197, 198]. In sulfuric acid, for example, the dominating reaction is not OER but decomposition of sulfates to persulfates [194, 197, 199, 205, 206]:

$$2\,HSO_4^- \longrightarrow S_2O_8^- + 2\,H^+ + 2\,e^-; \quad E^0(S_2O_8^-/HSO_4^-) = 2.12\,V_{RHE} \quad (8.1)$$

Furthermore, several reports already target $S_2O_8^-$ instead of O_2 as the product [196, 197, 199]. For the product formation on WO_3, the pH of the solution plays an important role. If the pH is higher than 1, OER becomes kinetically favored over the $S_2O_4^{2-}$ decomposition reaction [194].
In methanesulfonic acid, no oxygen at all is produced at the photoanode [195]. The standard potential for the methanesulfonic acid RedOx couple
$E^0 = ((CH_3SO_3)_2/CH_3SO_3^-)$ has not been reported, but is, according to previous reports, estimated to be lower than the decomposition potential of the $E^0(S_2O_8^-/HSO_4^-)$ couple [196].
In contrast to the sulfur-containing electrolytes, the standard potential of $HClO_4$ decomposition lies at a much higher level [197].

$$ClO_4^- \longrightarrow ClO_4\cdot + e^-, \quad E^0(ClO_4\cdot/ClO_4^-) = 2.75\,V_{RHE} \quad (8.2)$$

Although the degradation of ClO_4^- is thermodynamically possible on WO_3 electrodes, the main product measured experimentally is O_2. Furthermore, enhanced H_2O_2 formation rates have been reported [197, 198]. However, in contrast, to the persulfates formed in the reaction with sulfur-containing electrolytes, perchlorate radicals are not stable in aqueous environment. It has been demonstrated earlier that perchlorate radicals bond to active sites is weak, and thus, they detach easily from the WO_3 surface [197]. This leads to the conclusion that OER is catalyzed by $ClO_4\cdot$ radicals with an H_2O_2 intermediate. With this mediator, a faradaic efficiency of close to 100% was obtained for WO_3 photoelectrodes in $HClO_4$ solution [197].
There have been no reports about the dominant reactions or faradaic efficiencies on WO_3 photoelectrodes for nitric acid so far. As N in the HNO_3 complex is already in its highest oxidation state, further oxidation can be excluded at the conditions presented here. It can be speculated that oxidation of the molecule with $E^0(NO_3\cdot/NO_3^-)$ similar to $E^0(ClO_4\cdot/ClO_4^-)$ takes place. Alternatively, the primary reaction on the WO_3 photoanode might be, indeed, OER without an intermediate reaction.
W^{n+} has a strong complexing affinity, and the reaction products are highly reactive peroxides and persulfates. Thus, besides the different reaction kinetics on the surface of the electrodes, electrode degradation in the presence of the investigated electrolyte anions and reaction products must be considered [151, 193]. Therefore, the PEC-ICP-MS was utilized to detect WO_3 dissolution products *in-situ* under various photoelectrochemical protocols.

8.2.3 In-situ measurements of WO_3 photoelectrode stability

The stability of WO_3 photoanodes in different electrolytes was studied using the PEC-ICP-MS setup, as described in chapter 6. Dark and illuminated (385 nm, 50 mW cm^{-2}) CVs with a scan rate of 10 mV s^{-1} were performed consecutively in the same protocol. The potential, illumination intensity, the resulting currents, and W dissolution are shown in figure 8.4 for all electrolytes. While the electrodes are virtually stable during dark CVs, the electrodes dissolve in all electrolytes at high maximal rates between 0.5 ng s^{-1} cm^{-2} to 1.5 ng s^{-1} cm^{-2}. At these rates, a compact WO_3 electrode with a thickness of 2 µm would fully degrade within a few weeks. The total dissolved amount of W during the illuminated CVs is displayed in figure 8.4 c) for all electrolytes alongside the dissolution data. The photocorrosion is strongest in electrolytes, where the highest photocurrents are measured.

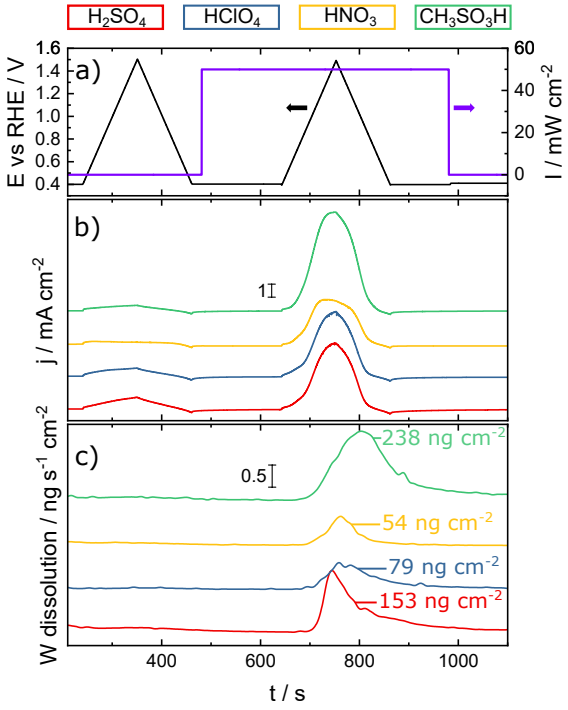

Figure 8.4: Photoelectrochemical stability of WO_3 thin films measured in different electrolytes. ***a)*** *Applied potential against the reversible hydrogen electrode (black) and illumination intensity (violet) as functions of time.* ***b)*** *Current response to the applied potential and illumination as a function of time.* ***c)*** *W dissolution as a function of time.*

As WO_3 appears to be stable in dark conditions, it is evident that the dissolution of W is connected to the processes triggered by illumination. These observations match with previous reports, where formation of reactive intermediates from anions due to the transfer of photogenerated holes was reported [196, 197]. The dissolution in the sulfur-containing electrolytes that form stable intermediates is strongly enhanced compared to perchloric acid and nitric acid, where no such behavior is known. In methanesulfonic acid and sulfuric acid, W dissolution of 250 ng cm^{-2} and 150 ng cm^{-2} are observed during one illuminated CV. In perchloric acid and nitric acid, on the other hand, the dissolution during one CV is significantly below 100 ng cm^{-2}. This indicates that the different reaction kinetics in different electrolytes have, in fact, a substantial impact on the stability of the WO_3 photoelectrodes.

The formation of stable complexes at the surface of the photoelectrodes seems to inhibit higher electrode degradation. The low dissolution rate in nitric acid is in line with the previous assumption that either OER or radical formation with fast decay takes place in this electrolyte.
However, currents deviate strongly in all electrolytes. Thus, a comparison on dissolution alone might be misleading. In previous publications and in chapter 7, the S-number, as described in section 3.1.2 was employed for such comparison [184, 207]. However, as discussed previously, the initial assumption regarding faradaic efficiency is misleading, as OER is not the dominant reaction. Thus, a generalized S-number concept for any oxidized species at the anode side Ox and the metallic content M of the catalyst is proposed.

$$\text{S-number(Ox)} = \frac{n(\text{Ox})}{n(\text{M})} \tag{8.3}$$

As the reaction product on WO_3 in different electrolytes is not clearly defined, a calculation of the S-number based on the number of transferred electrons e^- appears to be the right choice. Therefore, the S-number will here be calculated as

$$\text{S-number}(e^-) = \frac{n(e^-)}{n(\text{W})} \tag{8.4}$$

The S-number(e^-) is related to the previously established definition of the S-number as an OER metric by a factor of 4.

$$\text{S-number}(O_2) = \frac{\text{S-number}(e^-)}{4} \tag{8.5}$$

The S-numbers of WO_3 in all electrolytes calculated according to equation 8.4 are displayed in figure 8.5. The trends observed from the absolute dissolution in

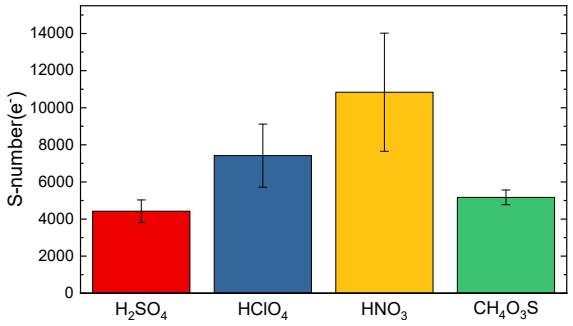

Figure 8.5: S-number $= \frac{n(e^-)}{n(\text{W})}$ ***of WO_3 thin films measured in different electrolytes.*** *Errorbars were calculated as standard deviation from five independent measurements.*

different electrolytes are confirmed by the S-numbers. In perchloric acid and nitric acid, the WO_3 photoelectrodes are significantly more stable compared to measurements in sulfuric acid and methanesulfonic acid. The higher stability in those electrolytes may be due to a faster detachment of reaction intermediates $ClO_4\cdot$

and speculatively $NO_3\cdot$. On the other hand, the reaction products of sulfuric acid and methanesulfonic acid, electrolytes that form stable persulfate complexes, might form complexes with dissolved W cations, leading to enhanced dissolution [208]. Similar effects were recently found in $BiVO_4$, another material considered for photoanodes in PEC water splitting [207]. Also, in classical electrocatalysis, similar effects, such as destabilization of Pt in the presence of Cl^- anions, are well known [209]. The destabilization occurs due to the formation of stable complexes that hinder redeposition of dissolved Pt, leading to higher dissolution rates. Complex formation has also been considered a significant factor in the degradation of photoanodes [41, 151, 193].
Compared to the study shown in Chapter 7, where photoelectrodes were synthesized from nanoparticles, the S-numbers increase by a factor of 5 (S-number(O_2)=200, chapter 7; S-number(e^-)=4000, this Chapter). Structural differences are known to influence kinetics at the surface of photoelectrodes [41]. The spray-coated photoelectrodes shown in this Chapter are more compact than photoelectrodes synthesized from commercial nanoparticles. This indicates a high impact of sample preparation methods and the resulting morphology of the electrode on the stability of photoelectrodes.
Furthermore, a glimpse at the reasons for the degradation of semiconductors in photoelectrochemical water splitting is taken. The decomposition of a semiconductor occurs via a transition state that requires activation energy. The activation energy has to be large enough to reach the surface back-bond energy of the semiconductor. While decomposition potentials are always calculated for structurally perfect materials, many factors can influence both the activation energy and the decomposition potential in reality. For example, defects on the electrode surface are much lower coordinated than sites in the bulk material and, thus, much more susceptible to photocorrosion. Photocorrosion usually starts at defect sites and increases alongside the defect concentration. Furthermore, the nature of the semiconductor/electrolyte interface plays a crucial role in photocorrosion. A few factors to name are adsorbing/desorbing anions/cations, reaction intermediates, complexation, redox processes, or photogenerated charge carriers [41, 201]. Theoretical calculations suggest that WO_3 photoelectrodes should be kinetically stable, if no ions are involved in the process, although they are thermodynamically susceptible to photocorrosion [41]. However, as shown in this Chapter, the kinetic barriers might be lowered in the presence of electrolyte anions leading to the photocorrosion of the WO_3 electrode. The decomposition potential of electrolytes used in this study are depicted in figure 8.6 alongside the thermodynamical potentials of water oxidation and reduction, the valence and conduction band of WO_3, and a calculated decomposition potential of WO_3 in the presence of Cl^- anions [151]. The decomposition potentials of the complex forming electrolytes (H_2SO_4, CH_4SO_3) are on a similar energy level as the decomposition potential of WO_3 in the presence of Cl^- anions. Thus, it is likely that similar decomposition processes occur in these electrolytes. The (estimated) potentials of $HClO_4$ and HNO_3, on the other hand, are energetically close to the valence band of WO_3. Thus, the oxidation of the photoanode with these electrolytes is less likely.

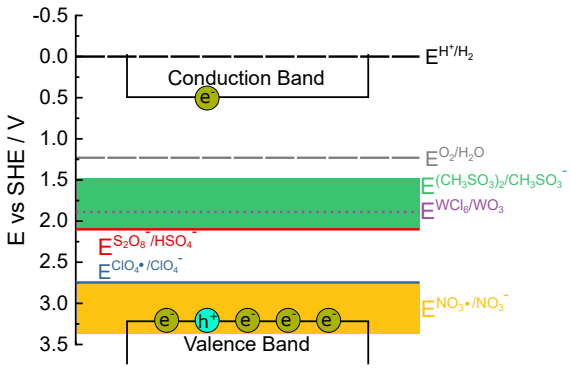

Figure 8.6: Schematic display of the energy levels of different electrolytic RedOx pairs with respect to the valence and conduction band of WO_3. *Narrow lines (red, blue) were taken from the literature. Broad lines (green, yellow) are estimated from stability data. The violet dashed line indicates the decomposition potential of WO_3 as estimated from theoretical calculation [151].*

8.3 Conclusions

In this Chapter, the stability of WO_3 photoanodes in different electrolytes was studied. A new method for the preparation of WO_3 thin films based on a peroxotungstic acid route was used. The films spray-coated films showed photoactivities similar to those seen in the literature. The achievable limiting photocurrent depends strongly on the electrolyte which suggests, that OER is not the dominant charge transfer reaction on the surface of WO_3 photoanodes. As previous reports suggest, the difference in maximally achievable photocurrent is probably related to anion oxidation on the photoelectrode surface. This is a severe issue for utilization of photoelectrodes in industrial applications. Moreover, it was found that the presence of different anions and their oxidation intermediate seriously affect the stability of WO_3 photoanodes. The lowest photostability was measured in electrolytes that form stable complexes in the form of persulfates by oxidation on the photoanode surface. It is possible that these intermediates either react with WO_3 or complex with dissolved W limiting redeposition reactions. Both would lead to increased dissolution.

9 Enhanced photostability of WO_3 photoanodes with iridium atomic layer depostion

Parts of the following study were summarized to a manuscript under the title: "Enhanced photostability of WO_3 photoanodes through iridium atomic layer deposition" [210].
Julius Knöppel, as the first author, designed the experiments, prepared the precursor, performed PEC-ICP-MS measurements, data analysis, and wrote the original draft of the manuscript.

9.1 Introduction

In the last two Chapters, the newly developed PEC-ICP-MS system showed that perceivably stable WO_3 photoanodes suffer from grave materials degradation under operation. In this Chapter, the mitigation strategy of coating WO_3 photoanodes with a co-catalyst is discussed.
The coating of photoelectrodes with additional layers is a common mitigation strategy towards stable photoelectrochemical applications. In general, two principles are most common. The first is surface passivation with a tunneling oxide. A chemically inert film, commonly TiO_2, is applied to the photoanode. The electrolyte does not contact the semiconductor, and the electrons produced in the reaction tunnel through the TiO_2 thin film [211–215]. The second mitigation strategy, which is also used in this Chapter, is coating the photoanode surface with OER catalysts, such as Co, Ir, or Ru, for co-catalytic effects [140, 216–218]. In addition to the protection from the electrolyte, these catalysts provide catalytic reaction sites towards OER. Ru decoration of WO_3 photoanodes significantly enhanced their activity [218]. Enhancement of WO_3 photoanodes with a Co-based co-catalyst significantly enhanced their photoactivity and photostability [140]. Also, the utilization of Ir in end-on bound dinuclear catalysts on WO_3 photoelectrodes resulted in a significant improvement of photoactivity [219].
Furthermore, some photoelectrode co-catalyst combinations change the reaction kinetics at the photoelectrode surface. A pristine WO_3 photoelectrode decomposes the sulfuric acid electrolyte into persulfates or produces peroxides instead of oxidizing water. Co, Ru, and Ir-based co-catalysts applied to the surface of such

photoelectrodes shift the dominant reaction at the photoanode surface to OER Iridium-based catalysts, applied to the surface of such photoelectrodes, shift the dominant reaction at the photoanode surface from persulfate production to OER [140, 218–220].
Photostability is greatly affected by the reaction kinetics at the surface of WO_3 photoanodes, as shown in the previous Chapter 8. The purpose of this Chapter is to study the effect of the application of co-catalysts to the surface of WO_3 photoanodes on their stability. The spray-coated WO_3 thin films, synthesized in Chapter 8, were coated with iridium in layers of different, controlled thicknesses by ALD to serve as a model system. Photoactivity and photostability were determined with the PEC-ICP-MS. The photoanodes show decreasing activity with increasing iridium layer thickness. This trend is supported by the literature [220]. Photostability of the electrodes, on the other hand, increases with increasing iridium layer thickness.

9.2 Results and discussion

9.2.1 Characterization

The WO_3 thin films synthesized and characterized in Chapter 8 were decorated with thin iridium layers by ALD. After the ALD treatment, the WO_3 films appear to be less transparent, as shown in figure 4.5. The decreased transparency was experimentally corroborated by UV-Vis measurements. UV-Vis data, as shown in figure 9.1, proves a non-characteristic increase of absorbance that can be attributed to Ir on the surface blocking fractions of the incident light. Note: slight qualitative changes between different samples can be attributed to the presence of scratches at the backside of the FTO coated glass slides. The thickness of the iridium layers

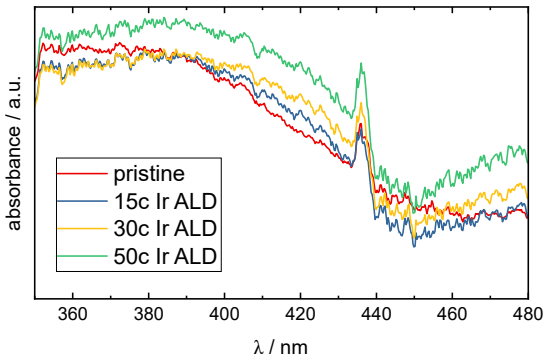

Figure 9.1: UV-Vis absorption spectra of iridium coated WO_3 thin films. *The non-characteristic increase of absorbance can be attributed to iridium on the film surface, blocking the incident light.*

was determined indirectly by ellipsometry. Si wafers were introduced during the coating process to the chamber alongside the samples. The ellipsometry measurements determined the iridium layer thicknesses after 15 (30, 50) cycles to be 0.5 nm (1.1 nm, 2.2 nm).

XPS measurements, as shown in figure 9.2, confirm these layer thicknesses qualitatively. Figure 9.2 a) shows XPS measurements of the W4f peak of all samples. The characteristic binding energy of the $W4f_{1/2}$ peak is observed at 35.7 eV, while the peak splitting to $W4f_{5/2}$ occurs with a $\Delta BE = 2.1$ eV [221]. The Ir deposited by ALD, shown in Figure 9.2 b), shows a chemical shift of 61.6 eV, suggesting mostly IrO_2 for the thinnest film. With metallic Ir expected at 60.6 eV, thicker films appear less oxidized [222]. Previous reports suggest that Ir deposited by ALD is deposited as oxides in thinner films while thicker layers tend to be fully reduced [223, 224]. The intensities of the high-resolution spectra coincide with the atomic composition from survey scans, shown in Figure 9.2 c). With increasing ALD cycles, the probed region increases in Ir content, while W and O become less abundant at the surface. These results are in line with the ellipsometry data.

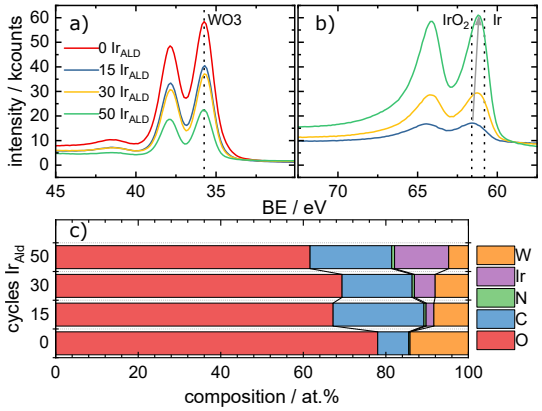

Figure 9.2: *High-resolution W4f* ***a)*** *and Ir4f* ***b)*** *spectra of the four WO_3 samples covered with various amounts of Ir. The color code corresponds to the number of Ir ALD cycles.* ***c)*** *Surface composition of each sample from a survey scan depending on Ir coverage.*

9.2.2 Photoelectrochemical behavior

To evaluate the photoelectrochemical behavior of the Ir coated WO_3 films, ramps with $10\,mV\,s^{-1}$ dark and illuminated (385 nm, $50\,mW\,cm^{-2}$) were performed in 0.1 M H_2SO_4. The results are shown in Figure 9.3.

The pristine film shows negligible dark currents. With increasing iridium layer thickness, dark currents increase as well. Metallic iridium, as present in the samples, shows a transition to iridium oxide at $0.926\,V_{RHE}$ [60, 225]. As OER starts above $1.23\,V_{RHE}$, it is possible that a combination of iridium electrooxidation and OER onset on iridium is responsible for this behavior. Further evidence towards an increase of the influence that the electrocatalytic properties of iridium have on the characteristics of the samples is obtained with dark CVs. As presented in Figure 9.4, the CVs show an increase of the characteristic Ir(IV) to Ir(III) electroreduction peak [70]. A similar increase in dark current was shown for Ru decorated WO_3 photoelectrodes [218].

Under illumination, the pristine WO_3 thin film shows limiting photocurrents of around $5\,mA\,cm^{-2}$. The photocurrent is higher than in other WO_3 thin films, which can be attributed to the utilization of low wavelength UV-light [195, 198].

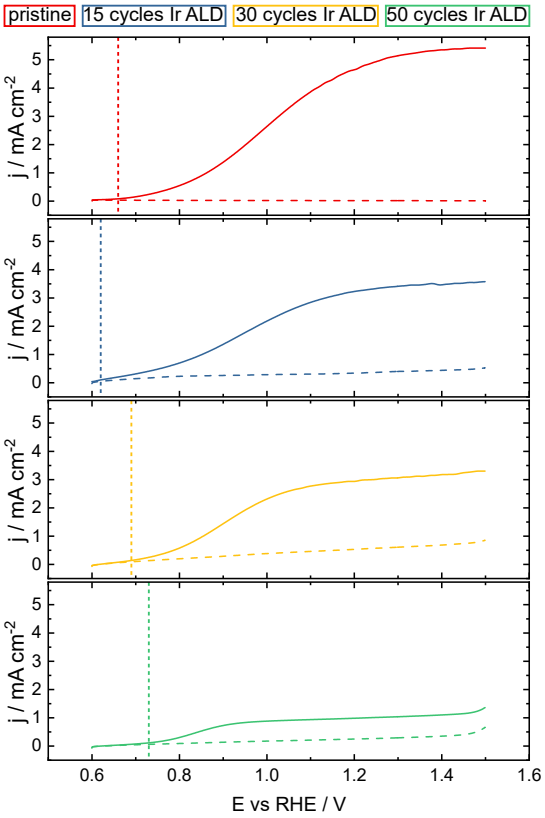

Figure 9.3: *Dark (dashed) and illuminated (solid, 50 mW cm^{-2} at 385 nm) LSVs of WO_3 thin films coated with iridium layers of different thickness by ALD in 0.1 M H_2SO_4 with a scan speed of 10 mV s^{-1}. The dashed, vertical lines indicate the photocurrent onset potentials.*

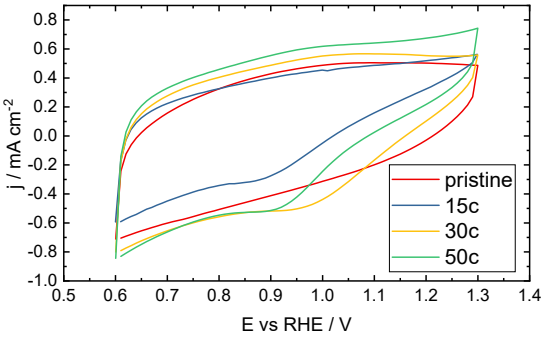

Figure 9.4: *Dark CVs of WO_3 thin films coated with iridium layers of different thickness by ALD. The characteristic Ir(IV) to Ir(III) reduction peak increases alongside the iridium layer thickness, indicating a stronger influence of the electrocatalytic properties of iridium.*

Compared to the standard 100 mW cm^{-2} of a full spectrum AM1.5G solar simulator, a much more significant fraction of the incident photons is absorbed and converted to photocurrent [226].
As indicated by dashed, vertical lines in Figure 9.3, the photocurrent onset potentials decrease slightly with the thinnest Ir layer. This behavior can be related to the catalytic effect of Ir on the WO_3 surface and was similarly shown in Ru decorated WO_3 thin films [218]. For thicker ALD layers, however, the photocurrent onset potential increases again. This behavior might be related to the aforementioned stronger emphasis of Ir properties in the samples. In samples with thicker iridium layers, the fraction of photocurrents might decrease in contrast to increased electrooxidative currents.

The limiting photocurrents decrease to around 3 mA cm^{-2} for the samples coated

with 15 and 30 ALD cycles. Samples coated with 50 cycles of iridium show even lower limiting photocurrents of 1.5 mA cm^{-2}. This behavior can not solely be attributed to increasing absorption with increasing iridium layer thickness. Similar behavior was shown for Ir coated WO_3 electrodes with backlight illumination, where increased absorption should not influence the photocurrents [220]. Parts of the change in limiting photocurrents can be attributed to changes in kinetics at the surface of the photoelectrodes. Pristine WO_3 photoelectrodes in sulfuric acid show almost 100 % faradaic efficiency towards the decomposition of electrolyte anions [199].

$$2\,HSO_4^- \longrightarrow S_2O_8^- + 2\,H^+ + 2\,e^-; \quad E^0(S_2O_8^-/HSO_4^-) = 2.12\,V_{RHE} \quad (9.1)$$

With even small layers of iridium on the surface, the reaction kinetics at the photoelectrode surface shifts towards OER.

$$2\,H_2O \longrightarrow O_2 + 4\,H^+ + 2\,e^-; \qquad E^0(O_2/H_2O) = 1.23\,V_{RHE} \quad (9.2)$$

The iridium coating facilitates the thermodynamically favorable but more sluggish four-electron OER process over the two-electron formation of persulfates [220]. However, as the shown Ir coatings have shown to decrease current, and thus, H_2 production at the cathode side, such modification is not expedient. Different behavior was shown for Ru decoration on WO_3 surfaces. The Ru decoration had a beneficial effect on the activity of WO_3 photoelectrodes [218]. No clear conclusions regarding the differences to this work can be drawn, as no measurement of Ru layer thickness was provided. However, it can be speculated that the enhanced photoelectrochemical performance of Ru compared to Ir can be attributed to its better electrocatalytic activity towards OER [83]. With iridium as co-catalyst for WO_3 photoelectrodes, lower activity limitation was recently overcome by utilizing Ir as active centers on dinuclear heterogeneous catalysts bound to the surface of the photoelectrodes [219]. Similar to the aforementioned Ir coated WO_3 photoelectrodes, the selectivity of the photoanodes shifted from persulfate species to OER. However, the results from the literature are not fully comparable to the results shown in this study. The electrolytes in the aforementioned studies were 0.1 M K_2SO_4 at pH 3 and 0.1 M H_2SO_4 respectively [219, 220], respectively. On the other hand, the electrolyte used in this work was 0.1 M H_2SO_4. As the last Chapter 8 showed, electrolyte choices influence activity, selectivity, and stability of WO_3 photoanodes Thus, an effect of electrolyte pH on the results cannot be excluded. Therefore, no clear comparison regarding the system shown in this work and literature data can be drawn.
However, the reaction kinetics at photoelectrodes appear to be changing significantly with iridium coating. As reaction kinetics have been shown to change stability as well in Chapter 8, the stability of the iridium coated WO_3 photoelectrodes is tested with the PEC-ICP-MS.

9.2.3 Photoelectrochemical stability

The photoelectrochemical stability of the iridium-coated WO_3 samples was measured with the previously established PEC-ICP-MS system. It is known from electrocatalysis research that iridium dissolution is not dependent on applied potential but transferred charge [38]. As the limiting photocurrents diverge between all samples, a constant current protocol at $2\,mA\,cm^{-2}$ was used to enable better comparison. The resulting potential, tungsten dissolution, and iridium dissolution as functions of time are displayed in Figure 9.5. The operating potential, as shown in Figure 9.5 a), increases in this protocol with increasing iridium layer thickness. As discussed before, the photoelectrochemical behavior is driven by the reaction taking place at the electrode surface. However, as shown in Figure 9.5 b), the real-time tungsten dissolution rate is strongly enhanced against the samples with iridium coating. While the dissolution peak of the pristine sample reaches its maximum at $1.5\,ng\,s^{-1}\,cm^{-2}$ and stabilizes around $1\,ng\,s^{-1}\,cm^{-2}$, W dissolution rates of the Ir coated samples do not exceed $250\,pg\,s^{-1}\,cm^{-2}$. With increasing thickness of the iridium coating, the stability of the WO_3 photoelectrodes increases. The sample coated with 50 ALD cycles shows only minor signs of tungsten dissolution. Figure 9.5 c) shows that the Ir coated samples show a similar trend in iridium dissolution. The strongest iridium dissolution of up to $200\,pg\,s^{-1}\,cm^{-2}$ is observed in the sample coated with 15 ALD cycles. Dissolution rates of the samples with the thickest iridium coating of 50 ALD cycles stabilize around $50\,pg\,s^{-1}\,cm^{-2}$.

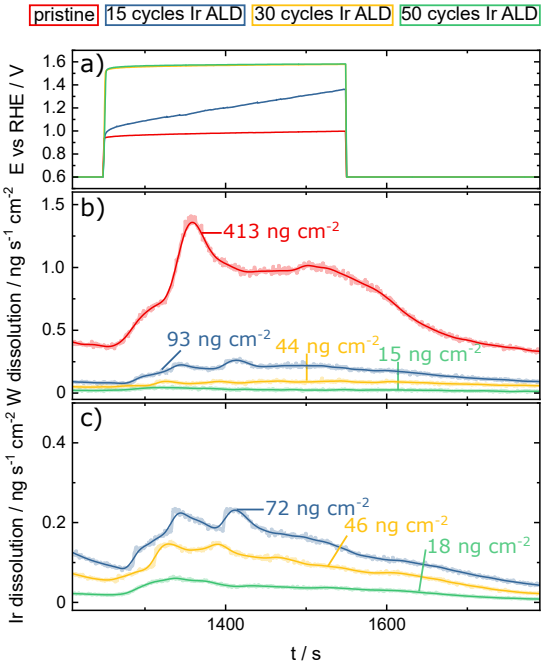

Figure 9.5: Potential and dissolution profiles at a constant current step of $2\,mA\,cm^{-2}$ under continuous illumination at $\lambda = 385\,nm$ at an intensity of $50\,mW\,cm^{-2}$. ***a)*** *resulting potential.* ***b)*** *tungsten dissolution.* ***c)*** *iridium dissolution.*

These dissolution rates reflect on the total dissolved W amounts during the photocurrent step. While the pristine sample loses $413\,ng\,cm^{-2}$ W, the sample with 50 ALD cycles of Ir loses only $15\,ng\,cm^{-2}$ W- a decrease by a factor of 30. Even the

thinnest layer of iridium increases the photostability of WO_3 drastically. Also, the stability of iridium increases with increasing iridium layer thickness. The sample with 15 ALD cycles of Ir suffers an Ir loss of 72 ng cm^{-2} throughout the protocol, decreasing to 72 ng cm^{-2} for the sample with 50 ALD cycles Ir. This stabilization with increasing Ir layer thickness is unexpected if the results from the XPS measurements are viewed from the perspective of Ir electrocatalysis. The XPS spectra shed decreasing oxidation with increasing iridium layer thickness. In OER electrocatalysis, iridium-based electrocatalysts show typically increased stability with an increasing oxidation state [38]. However, the higher stability of samples with thicker iridium coating might originate from the structural features of the coating itself. A larger number of ALD cycles will always produce a coating with fewer defects and better shielding from the electrolyte. As discussed before, the iridium coating of WO_3 photoanodes most likely shifts the dominant reaction in the sulfuric acid electrolyte from persulfate production to OER. As the highly reactive persulfates have shown to enhance dissolution in the previous Chapter 8. The O_2 molecules produced in OER, on the other hand, do not lead to enhanced complexation. Another factor preventing dissolution might be the sealed electrode-electrolyte interface. The iridium layers act here as an intermediate layer that prevents contact of the electrolyte with tungsten oxide.
The results show a clear advantage of iridium for the stabilization of WO_3 photoanodes at the cost of photoactivity. Nevertheless, regarding the possible use of iridium in a hypothetical commercial device, other considerations must be considered. In PEMWE, iridium is a crucial component of the anode catalyst layer [33]. As iridium is a scarce noble metal, hypothetic utilization as co-catalyst in upscaling of photoelectrochemical water splitting has to compete against utilization in PEMWE. Thus, it is necessary to draw a comparison of Ir operations stability in PEMWE vs. photoelectrochemical water splitting.
For this comparison, the S-number(e^-), as introduced in equation 8.5 (Chapter 8) is used. S-numbers were calculated for both metals (W, Ir) and all samples and are shown in Figure 9.6. As S-numbers were formerly only calculated for OER catalysts with a single active element, it has to be discussed if a separate calculation is justified in this case. The S-numbers range from 3600 to higher numbers for both metals. This shows that only a tiny fraction of the observed currents drive the individual dissolution reactions, concluding that it is justified to treat both iridium dissolution and tungsten dissolution as independent side reactions to the primary reaction at the electrode. Thus, the S-numbers can be calculated individually for both metals.

As iridium is a scarce noble metal, a comparison of iridium stability in a photoelectrochemical system, where it is used as a co-catalyst, and electrochemical systems, where it is used as component of electrocatalysts, is required. It has to be noted that the S-numbers(e^-) used in this Chapter have to be divided by four to be comparable with the S-number used in Chapter 5. The S-numbers(e^-) of Ir coatings on WO_3 photoelectrode, shown in this Chapter, range from 20 000 to 40 000. This corresponds to S-numbers of 5000 to 10 000 in the Ir electrocatalysis

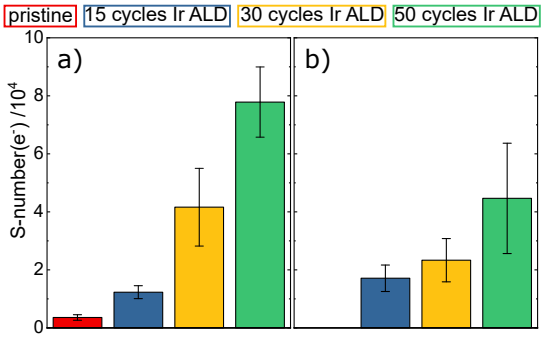

Figure 9.6: S-number(e^-) = $\frac{e^-}{M}$ for iridium coated WO_3 thin films. ***a)*** *S-numbers calculated for W.* ***b)*** *S-numbers calculated for Ir.*

literature. Similar S-numbers have been shown for metallic iridium [38]. However, with increasing oxidation state, the S-numbers of iridium increase drastically. For hydrous iridium oxide, S-numbers between 10×10^4 to 10×10^5 would be expected. For rutile iridium oxide, the S-numbers even increase to 10×10^7 [38]. On top of that iridium is even more stable if utilized in PEMWE in contrast to acidic electrolyte. As shown in Chapter 5, the S-numbers rise to 10×10^9 - several orders of magnitude above the S-numbers of iridium as a co-catalyst on the WO_3 photoanode, questioning the use of iridium as co-catalyst in a photoelectrochemical system.

9.3 Conclusions

In this Chapter, the successful ALD coating of spray-coated WO_3 photoanodes with iridium in layers of defined thickness was demonstrated. The thickness of iridium was measured by ellipsometry to be 0.5 nm to 2.2 nm. The order of magnitude was confirmed by XPS. The iridium coatings exhibit a less oxidized state with increasing layer thickness. The samples showed a non-specific increase in absorbance in UV-vis measurements due to the iridium layers blocking the light.
Photoelectrochemical measurements showed decreased limiting photocurrents with increasing iridium layer thickness, although iridium is a sufficient anode catalyst for electrochemical water splitting. The decrease in photoactivity was attributed to a change in the anode reaction. Based on previous findings, it was concluded that the dominant reaction on the pristine WO_3 photoanode is the decomposition of the sulfuric acid electrolyte, while the dominant reaction on the iridium coated samples is OER [219, 220].
As changes in the kinetics of the reactions at the photoanode are expected to change the photostability, PEC-ICP-MS measurements were performed to obtain *in-situ* dissolution data. While the pristine sample dissolves at a rate at which the photoelectrode would fully degrade in several hours, even the thinnest iridium coating stabilizes the whole electrode significantly. This effect continues with increasing iridium layer thickness, which can be attributed to a coating with fewer defects at increased iridium layer thickness. However, the downside of the stabilization is that the iridium coating dissolves at rates similar to those of iridium as a catalyst

in electrochemical water splitting.
Even the thinnest iridium layer of ca. 0.5 nm notably enhances the photostability of WO_3 photoelectrodes. This stability enhancement, however, comes with severe disadvantages. The photocurrent density decreases by around 40 % compared to pristine WO_3 photoelectrodes, partly because of incident light blocking and partly because of the shift of the dominant reaction. The former problem might be solved by decorating the surface with iridium nanoparticles, single-atom catalysts, or dinuclear iridium catalysts [219, 220, 227]. However, these catalysts might pronounce smaller stability enhancements, as the shielding of the photoelectrode from the electrolyte is less efficient. The difference in the S-numbers of iridium as co-catalyst on WO_3 photoanode to iridium in PEMWE makes it inherently clear that utilization of iridium in such a device would not be expedient. However, this work shows that co-catalysts, even in extremely low amounts, and their related kinetic shifts, can already notably increase photostability. These findings open the possibility to design better systems in terms of photostability by coating the surface of photoelectrodes with very thin overlayers. However, since the price of iridium significantly increased recently, and iridium is better utilized in PEMWE, abundant materials that are as stable as their noble counterparts at low pH have to be found for efficient utilization.

10 Summary and Conclusions

In this work, substantial progress towards understanding the degradation mechanisms of OER electrocatalysts for acidic electrolysis in PEMWE was made. In Chapter 5, the discrepancy between OER electrocatalyst dissolution in AMS and MEA, which already had been predicted before [38], was confirmed. A newly developed MEA with a cell body made from Teflon, gold-coated bipolar plates, and a platinized stretched metal as PTL, excluding GR as a factor for measurement errors, was used to determine catalyst dissolution in MEA. The obtained S-numbers were compared to those measured in the established SFC-ICP-MS system and revealed a discrepancy of almost five orders of magnitude. A thorough parameter study of the factors catalyst loading, flow rate, dissolved ions in the electrolyte, Nafion® content in the catalyst layer and electrolyte pH in SFC-ICP-MS revealed that only pH plays a substantial role from all the observed parameters. MEA measurements with acidic electrolyte in the anode water cycle confirmed the stability dependence of Ir-based OER catalysts on pH. Furthermore, time-resolved long-term measurements of catalyst stability in an H-cell as AMS and MEA revealed a catalyst stabilization over time in the MEA, which does not occur in AMS. Additionally, a comparison of different OER catalysts in both AMS and MEA revealed that the stability trends observed in AMS can be transferred to MEA on a short timescale. However, the Ru-based catalyst is already fully degraded on a longer timescale, and the Ir-based catalysts equilibrate in terms of stability after a more prolonged operation.

Similar progress was made regarding the understanding of photoelectrocatalysts. A new PEC-ICP-MS system with a UV-light source, as shown in Chapter 6, was developed to study the dissolution of photoelectrocatalysts in real-time. The PEC-ICP-MS was used to study the degradation of WO_3, a material which has been a candidate for a photoanode since the beginning of photoelectrochemical water splitting.

As shown in Chapter 7, the proof of concept exhibited that WO_3 photoelectrodes dropcast from nanoparticles on an Au backing electrode suffer from substantial dissolution under illumination. The dissolution was shown to be significantly higher than OER electrocatalyst dissolution in electrochemical devices. Furthermore, a linear dependence of WO_3 dissolution on the intensity of incident light was shown. These findings on WO_3 stability were further extended in the following Chapters. In Chapter 8, a study on the effect of different acidic electrolytes on photostability was shown. WO_3 thin films on FTO were spray-coated from a peroxotungstic acid precursor and utilized as photoelectrodes. Photoactivity was shown to decrease in the electrolyte from $CH_3OSH > H_2SO_4 \approx HClO_4 > HNO_3$, while photostability

showed the opposite trend. The higher dissolution in sulfur-containing electrolytes was related to the formation of highly reactive persulfate species that can complexate with photoelectrodes. In $HClO_4$ and HNO_3, on the other hand, water oxidation with radical intermediates drives the reaction.
In the final study of this work, shown in Chapter 9, a common mitigation strategy towards higher stability is studied. The WO_3 photoanodes are coated with iridium as OER co-catalyst in different thicknesses by ALD. Thus, the study was able to provide not only insights about the stability of co-catalysts in photoelectrochemical water splitting, but also about the feasibility of using iridium for this purpose in comparison to utilization in PEMWE. The iridium layers decrease the photoactivity of the photoelectrodes significantly. This decrease in photoactivity was related to a change of kinetics on the photoelectrode surface. While the pristine WO_3 photoelectrode produces mainly persulfates, iridium-coating shifts the dominant reaction to the more sluggish OER. The iridium-coating significantly stabilizes the WO_3 photoelectrodes. Even the thinnest iridium layer enhances WO_3 stability by a factor of four, increasing with thicker layers. However, the iridium-coating dissolves as well, which opens the question, if utilization of iridium as co-catalyst in photoelectrochemical water splitting is the proper use for this scarce noble metal, or if it is better used as electrocatalyst in PEMWE.
The stability of iridium as an OER catalyst in electrochemical systems with aqueous acidic electrolyte is slightly higher than in photoelectrochemical devices. If PEMWE devices are compared to photoelectrochemical devices, as shown in Chapter 5, the differences increase to several orders of magnitude. In the light of the iridium scarcity, it is evident that utilization of iridium as a co-catalyst in photoelectrochemical devices is not expedient if maximizing hydrogen production is the goal. Thus, efficient resource utilization of iridium would mean using it in PEMWE and not photoelectrochemical devices.
The observed stabilization of photoelectrodes through a shift in kinetics, on the other hand, indicates that photoelectrochemical water splitting might be valuable in the future, if abundant and stable co-catalysts can be found.
In the bigger picture of current research, the methods shown in this work will help to gain further insights. Other works regarding the discrepancies between AMS and MEA have been published at a similar time as the corresponding paper with data from Chapter 5. Browne et al. compared activities of different catalysts in AMS and MEA, showing that several catalysts over or underperform in the AMS [117]. Fathi Tovini et al. related the stability discrepancies between AMS and MEA to bubbles from gas evolution at the micro- and nanoscale that do not detach from the catalyst surface [228]. As also other works indicate that the gap between academic research has to be crossed, further development of the GR-free MEA is necessary [228]. Further research should include dynamic operation, parameter studies such as loading, and potentially coupling to analytics for real-time data. Furthermore, the potential of GDE setups regarding utilization in OER catalyst research has to be evaluated.
Also, the advances made in this work have found their way into photoelectrochemical research. Similar methods to the PEC-ICP-MS have been developed

shortly after the work shown in Chapter 7 was published [207, 229, 230], showing that research interest in this area has increased recently. The next challenges towards further development of this method are exchanging the light source for a full AM1.5G spectrum towards more realistic measurement conditions and rapid screening of multiple catalysts towards a faster detection of potential stable semiconductor electrolyte interfaces.

11 Outlook

In this work, several steps towards a better understanding of the stability of anode catalysts in electrochemical and photoelectrochemical systems, which are essential for the transition to a sustainable energy system, were shown. The results shown here, however, only allow a small glimpse. As seen in Chapter 5, the real conditions under which electrocatalysts operate in PEMWE are not fully understood. Thus, in order to proceed further in the development, a complete understanding of the conditions in PEMWE is sufficient. A further step towards this goal has already been taken by Mayerhöfer et al. by showing that polymer electrolytes, in fact, do not change pH on the surface of an electrode [231]. These insights, combined with a transfer from this work towards MEAs based on alkaline ionomers might assist in the development of stable and efficient electrolytes based on abundant transition metals. Furthermore, catalyst dissolution in the MEA system was only studied under steady-state conditions. For studying catalyst dissolution in MEA systems under dynamic conditions, however, the low dissolution rates might provide a challenge regarding measurement sensitivity. Some insights might be gained in bulk measurements under dynamic operation but if real-time analysis was the goal, measurements sensitivity compared to the ICP-MS system must be enhanced.
As this work has shown, the scarce noble metals are better utilized in electrochemical than photoelectrochemical systems. In the far future, however, and with abundant catalysts, they might be helpful to produce value added chemicals. However, to achieve this goal, a deeper understanding of the degradation mechanisms across the range of potential materials has to be achieved. The LED setup used in this work is a sufficient first step, but future works should test photoelectrocatalysts under more realistic conditions. A first step towards this goal has already been taken, as Jenewein et al. further developed the PEC-ICP-MS to operate with an AM1.5G light source instead of an LED light source [232]. This system will help to identify stable photoelectrocatalysts to utilize in upcoming devices.

Bibliography

1. Arrhenius, S. On the Influence of Carbonic Acid in the Air upon the Temperature of the Ground. *Philosophical Magazine* **5,** 237–276 (1896).
2. Plass, G. N. The Carbon Dioxide Theory of Climatic Change. *Tellus* **8,** 140–154 (1956).
3. Callendar, G. S. On the Amount of Carbon Dioxide in the Atmosphere. *Tellus* **10,** 243–248 (1958).
4. Keeling, C. D. Is Carbon Dioxide from Fossil Fuel Changing Man's Environment? *Proc. American Philosophical Society* **114,** 10–17 (1970).
5. *Energy, transport and environment statistics | 2020 Edition* ISBN: ISBN 978-92-76-20737-5. `https://ec.europa.eu/eurostat/de/web/products-statistical-books/-/ks-dk-20-001` (eurostat, 2020).
6. Oliver, J. E. in *Encyclopedia of World Climatology* (ed Oliver, J. E.) 443–443 (Springer Netherlands, Dordrecht, 2005). ISBN: 978-1-4020-3264-6.
7. Horowitz, C. A. Paris Agreement. *International Legal Materials* **55,** 740–755 (2017).
8. Rogelj, J. *et al.* Paris Agreement climate proposals need a boost to keep warming well below 2 °C. *Nature* **534,** 631–639 (2016).
9. Jacobson, T. A. *et al.* Direct human health risks of increased atmospheric carbon dioxide. *Nature Sustainability* **2,** 691–701 (2019).
10. Kim, J. H., Hansora, D., Sharma, P., Jang, J. W. & Lee, J. S. Toward practical solar hydrogen production - an artificial photosynthetic leaf-to-farm challenge. *Chem Soc Rev* **48,** 1908–1971 (2019).
11. Armaroli, N. & Balzani, V. *Energy for a Sustainable World: From the Oil Age to a Sun-Powered Future* 390. ISBN: 978-3527325405 (Wiley-VCH, 2010).
12. Jacobson, M. Z. Review of solutions to global warming, air pollution, and energy security. *Energy Environ. Sci.* **2,** 148–173 (2009).
13. Ran, J., Jaroniec, M. & Qiao, S. Z. Cocatalysts in Semiconductor-based Photocatalytic CO_2 Reduction: Achievements, Challenges, and Opportunities. *Adv Mater* **30,** 1704649 (2018).
14. Yang, M. Q. & Xu, Y. J. Photocatalytic conversion of CO_2 over graphene-based composites: current status and future perspective. *Nanoscale Horiz* **1,** 185–200 (2016).

15. Habisreutinger, S. N., Schmidt-Mende, L. & Stolarczyk, J. K. Photocatalytic reduction of CO_2 on TiO_2 and other semiconductors. *Angew Chem Int Ed Engl* **52,** 7372–7408 (2013).

16. Lewis, N. S. & Nocera, D. G. Powering the planet: Chemical challenges in solar energy utilization. *Proceedings of the National Academy of Sciences* **103,** 15729–15735 (2006).

17. *International Energy Agency, Data and Statistics* Web Page. 2021. `https://www.iea.org/data-and-statistics?country=WORLD&fuel=Energy%20supply&indicator=TPESbySource`.

18. De Luna, P. *et al.* What would it take for renewably powered electrosynthesis to displace petrochemical processes? *Science* **364** (2019).

19. Katsounaros, I., Serhiy, C., Zeradjanin, A. & Mayrhofer, K. J. Oxygen Electrochemistry as a Cornerstone for Sustainable Energy Conversion. *Angewandte Chemie International Edition* **53,** 102–121 (2014).

20. Inglis, J. L., MacLean, B. J., Pryce, M. T. & Vos, J. G. Electrocatalytic pathways towards sustainable fuel production from water and CO_2. *Coordination Chemistry Reviews* **256.** Solar Fuels- by invitation only, 2571–2600 (2012).

21. Verne, J. *The Mysterious Island* ISBN: 9780684209722 (C. Scribner's Sons, 1920).

22. Turner, J. A. Sustainable Hydrogen Production. *Science* **305,** 972–974 (2004).

23. Bockris, J. O. A Hydrogen Economy. *Science* **176,** 1323–1323 (1972).

24. Norskov, J. K. *et al. Research needs towards sustainable production of fuels and chemicals - EnergyX* Report (2019).

25. Faber, C. *et al. Solar Energy for a Circular Economy* Report (2020). `https://sunriseaction.com/wp-content/uploads/2020/06/Roadmap_finalversion_web.pdf`.

26. *Kopernikus P2X Project funded by the German Ministry of Education and Research (BMBF)* Web Page. 2020. `https://www.kopernikus-projekte.de/projekte/p2x`.

27. Bundesministerium für Wirtschaft und Energie. Die Nationale Wasserstoffstrategie (2020).

28. Stockford, C. *et al.* H2FC SUPERGEN: An overview of the Hydrogen and Fuel Cell research across the UK. *International Journal of Hydrogen Energy* **40,** 5534–5543 (2015).

29. Yano, J. *et al.* JCAP Research on Solar Fuel Production at Light Sources. *Synchrotron Radiation News* **27,** 14–17 (2014).

30. Max-Planck-Institute for chemical energy conversion. *Solarify - Wüsten-wasserstoff: Neuer Anlauf mit Destertec 3.0* Web Page. 2019. https://www.solarify.eu/2019/11/26/582-wuesten-wasserstoff-neuer-anlauf-mit-desertec-3-0/.

31. Wendt, H. & Imarisio, G. Nine years of research and development on advanced water electrolysis. A review of the research programme of the Commission of the European Communities. *Journal of Applied Electrochemistry* **18,** 1–14 (1988).

32. Mayyas, A., Ruth, M., Pivovar, B., Bender, G. & Wipke, K. Manufacturing Cost Analysis for Proton Exchange Membrane Water Electrolyzers. *Golden, CO: National Renewable Energy Laboratory.* **NREL/TP-6A20-72740.** https://www.nrel.gov/docs/fy10osti/72740.pdf (2018).

33. Carmo, M., Fritz, D. L., Mergel, J. & Stolten, D. A comprehensive review on PEM water electrolysis. *International Journal of Hydrogen Energy* **38,** 4901–4934 (2013).

34. Bareiß, K., de la Rua, C., Möckl, M. & Hamacher, T. Life cycle assessment of hydrogen from proton exchange membrane water electrolysis in future energy systems. *Applied Energy* **237,** 862–872 (2019).

35. Johnson Matthey. *Daily prices between 01 Jul 2020 and 28 May 2021* Web Page, accession date May 28th 2021. http://www.platinum.matthey.com/prices/price-charts#.

36. Minke, C., Suermann, M., Bensmann, B. & Hanke-Rauschenbach, R. Is iridium demand a potential bottleneck in the realization of large-scale PEM water electrolysis? *International Journal of Hydrogen Energy* **46,** 23581–23590 (2021).

37. Ardo, S. *et al.* Pathways to electrochemical solar-hydrogen technologies. *Energy & Environmental Science* **11,** 2768–2783 (2018).

38. Geiger, S. *et al.* The stability number as a metric for electrocatalyst stability benchmarking. *Nature Catalysis* **1,** 508–515 (2018).

39. Alia, S. M. & Anderson, G. C. Iridium Oxygen Evolution Activity and Durability Baselines in Rotating Disk Electrode Half-Cells. *Journal of The Electrochemical Society* **166,** F282–F294 (2019).

40. Alia, S. M. *et al.* Activity and Durability of Iridium Nanoparticles in the Oxygen Evolution Reaction. *Journal of The Electrochemical Society* **163,** F3105–F3112 (2016).

41. Nandjou, F. & Haussener, S. Kinetic Competition between Water-Splitting and Photocorrosion Reactions in Photoelectrochemical Devices. *ChemSusChem* **12,** 1984–1994 (2019).

42. Arthurs, C. & Kusoglu, A. Compressive Creep of Polymer Electrolyte Membranes: A Case Study for Electrolyzers. *ACS Applied Energy Materials* **4,** 3249–3254 (2021).

43. Yu, Y. *et al.* Enhanced photoelectrochemical efficiency and stability using a conformal TiO_2 film on a black silicon photoanode. *Nature Energy* **2,** 17045 (2017).
44. Bard, A. J. & Faulkner, L. R. *Electrochemical Methods: Fundamentals and Applications* 2nd (Wiley, 2001).
45. Hamann, C. & Vielstich, W. *Elektrochemie* ISBN: 9783527310685 (John Wiley & Sons Australia, Limited, 2005).
46. Smolinka, T., Ojong, E. T. & Garche, J. *Hydrogen Production from Renewable Energies—Electrolyzer Technologies* in *Electrochemical Energy Storage for Renewable Sources and Grid Balancing* 103–128. ISBN: 9780444626165 (2015).
47. Perez, N. *Electrochemistry and Corrosion Science* ISBN: 978-1-4020-7860-6 (2004).
48. Roel Van de Krol, M. G. *Photoelectrochemical Hydrogen Production* ISBN: 978-1-4614-1379-0 (Springer US, Boston, MA, 2012).
49. Wagmann, D. D. *et al.* The NBS Tables of Chemical Thermodynamic Properties: Selected Values for Inorganic and C1 and C2 Organic Substances in SI Units. *Journal of physical and Chemical Reference Data* **11,** Supplement No. 2 (1982).
50. Binninger, T. *et al.* Thermodynamic explanation of the universal correlation between oxygen evolution activity and corrosion of oxide catalysts. *Sci Rep* **5,** 12167 (2015).
51. Guidelli, R. *et al.* Defining the transfer coefficient in electrochemistry: An assessment (IUPAC Technical Report). *Pure and Applied Chemistry* **86,** 245–258 (2014).
52. Guidelli, R. *et al.* Definition of the transfer coefficient in electrochemistry (IUPAC Recommendations 2014). *Pure and Applied Chemistry* **86,** 259–262 (2014).
53. Fabbri, E. & Schmidt, T. J. Oxygen Evolution Reaction—The Enigma in Water Electrolysis. *ACS Catalysis* **8,** 9765–9774 (2018).
54. Bockris, J. O. Kinetics of Activation Controlled Consecutive Electrochemical Reactions - Anodic Evolution of Oxygen. *Journal of Chemical Physics* **24,** 817–827 (1956).
55. Exner, K. S. & Over, H. Beyond the Rate-Determining Step in the Oxygen Evolution Reaction over a Single-Crystalline IrO_2(110) Model Electrode: Kinetic Scaling Relations. *ACS Catalysis* **9,** 6755–6765 (2019).
56. Geppert, J., Kubannek, F., Röse, P. & Krewer, U. Identifying the oxygen evolution mechanism by microkinetic modelling of cyclic voltammograms. *Electrochimica Acta* **380,** 137902 (2021).

57. Rossmeisl, J., Qu, Z. W., Zhu, H., Kroes, G. J. & Norskov, J. K. Electrolysis of water on oxide surfaces. *Journal of Electroanalytical Chemistry* **607,** 83–89 (2007).

58. Man, I. C. *et al.* Universality in Oxygen Evolution Electrocatalysis on Oxide Surfaces. *ChemCatChem* **3,** 1159–1165 (2011).

59. Gelderman, K., Lee, L. & Donne, S. W. Flat-Band Potential of a Semiconductor: Using the Mott–Schottky Equation. *Journal of Chemical Education* **84,** 685–688 (2007).

60. Pourbaix, M. *Atlas of Electrochemical Equlibria in Aqueous Solutions* ISBN: 0915567989 (NACE International, 1974).

61. Cherevko, S. & Mayrhofer, K. J. J. *On-Line Inductively Coupled Plasma Spectrometry in Electrochemistry: Basic Principles and Applications* in *Encyclopedia of Interfacial Chemistry* 326–335. ISBN: 9780128098943 (2018).

62. Ayers, K. The potential of proton exchange membrane–based electrolysis technology. *Current Opinion in Electrochemistry* **18,** 9–15 (2019).

63. Mauritz, K. A. & Moore, R. B. State of understanding of nafion. *Chem Rev* **104,** 4535–4585 (2004).

64. Onda, K. *et al.* Performance Analysis of Polymer-Electrolyte Water Electrolysis Cell at a Small-Unit Test Cell and Performance Prediction of Large Stacked Cell. *Journal of The Electrochemical Society* **149,** A1069 (2002).

65. Shin, H.-S. & Oh, B. S. Water transport according to temperature and current in PEM water electrolyzer. *International Journal of Hydrogen Energy* **45,** 56–63 (2020).

66. Lædre, S., Kongstein, O. E., Oedegaard, A., Karoliussen, H. & Seland, F. Materials for Proton Exchange Membrane water electrolyzer bipolar plates. *International Journal of Hydrogen Energy* **42,** 2713–2723 (2017).

67. Hsueh, K.-L., Tsai, L.-D., Lai, C.-C. & Peng, Y.-M. Direct Methanol Fuel Cells. *Electrochemical Technologies for Energy Storage and Conversion,* 701–727 (2012).

68. McCrory, C. C. L. *et al.* Benchmarking Hydrogen Evolving Reaction and Oxygen Evolving Reaction Electrocatalysts for Solar Water Splitting Devices. *Journal of the American Chemical Society* **137,** 4347–4357 (2015).

69. McCrory, C. C. L., Jung, S., Peters, J. C. & Jaramillo, T. F. Benchmarking Heterogeneous Electrocatalysts for the Oxygen Evolution Reaction. *Journal of the American Chemical Society* **135,** 16977–16987 (2013).

70. Pickup, P. G. & Birss, V. I. A model for anodic hydrous oxide growth at iridium. *Journal of Electroanalytical Chemistry and Interfacial Electrochemistry* **220,** 83–100 (1987).

71. Schmidt, T. J. *et al.* Characterization of high-surface area electrocatalysts using a rotating disk electrode configuration. *Journal of the Electrochemical Society* **145,** 2354–2358 (1998).

72. Mayrhofer, K. J. J. *et al.* Measurement of oxygen reduction activities via the rotating disc electrode method: From Pt model surfaces to carbon-supported high surface area catalysts. *Electrochimica Acta* **53,** 3181–3188 (2008).
73. Garsany, Y., Baturina, O. A., Swider-Lyons, K. E. & Kocha, S. S. Experimental methods for quantifying the activity of platinum electrocatalysts for the oxygen reduction reaction. *Anal Chem* **82,** 6321–6328 (2010).
74. Pham, C. V. *et al.* IrO_2 coated TiO_2 core-shell microparticles advance performance of low loading proton exchange membrane water electrolyzers. *Applied Catalysis B: Environmental* **269,** 118762 (2020).
75. Geiger, S. *et al.* Catalyst Stability Benchmarking for the Oxygen Evolution Reaction: The Importance of Backing Electrode Material and Dissolution in Accelerated Aging Studies. *ChemSusChem* **10,** 4140–4143 (2017).
76. Li, T. *et al.* Atomic-scale insights into surface species of electrocatalysts in three dimensions. *Nature Catalysis* **1,** 300–305 (2018).
77. Cherevko, S. Stability and dissolution of electrocatalysts: Building the bridge between model and "real world" systems. *Current Opinion in Electrochemistry* **8,** 118–125 (2018).
78. Frydendal, R. *et al.* Benchmarking the Stability of Oxygen Evolution Reaction Catalysts: The Importance of Monitoring Mass Losses. *ChemElectroChem* **1,** 2075–2081 (2014).
79. Brightman, E., Dodwell, J., van Dijk, N. & Hinds, G. In situ characterisation of PEM water electrolysers using a novel reference electrode. *Electrochemistry Communications* **52,** 1–4 (2015).
80. Trasatti, S. & Buzzanca, G. Ruthenium dioxide: A new interesting electrode material. Solid state structure and electrochemical behaviour. *Journal of Electroanalytical Chemistry and Interfacial Electrochemistry* **29,** A1–A5 (1971).
81. Kötz, R., Lewerenz, H. J. & Stucki, S. XPS Studies of Oxygen Evolution on Ru and RuO_2 Anodes. *Journal of The Electrochemical Society* **130,** 825–829 (1983).
82. Kötz, R., Lewerenz, H. J., Brüesch, P. & Stucki, S. Oxygen evolution on Ru and Ir electrodes. *Journal of Electroanalytical Chemistry and Interfacial Electrochemistry* **150,** 209–216 (1983).
83. Cherevko, S. *et al.* Oxygen and hydrogen evolution reactions on Ru, RuO_2, Ir, and IrO_2 thin film electrodes in acidic and alkaline electrolytes: A comparative study on activity and stability. *Catalysis Today* **262,** 170–180 (2016).
84. Roy, C. *et al.* Trends in Activity and Dissolution on RuO_2 under Oxygen Evolution Conditions: Particles versus Well-Defined Extended Surfaces. *ACS Energy Letters,* 2045–2051 (2018).
85. Ayers, K. E., Dalton, L. T. & Anderson, E. B. (Invited) Efficient Generation of High Energy Density Fuel from Water. *ECS Transactions* **41,** 27–38 (2019).

86. Kasian, O. *et al.* On the Origin of the Improved Ruthenium Stability in RuO_2–IrO_2 Mixed Oxides. *Journal of The Electrochemical Society* **163,** F3099–F3104 (2016).

87. Taie, Z. *et al.* Pathway to Complete Energy Sector Decarbonization with Available Iridium Resources using Ultralow Loaded Water Electrolyzers. *ACS Appl Mater Interfaces* **12,** 52701–52712 (2020).

88. Vesborg, P. C. K. & Jaramillo, T. F. Addressing the terawatt challenge: scalability in the supply of chemical elements for renewable energy. *RSC Advances* **2,** 7933–7947 (2012).

89. Ayers, K. *et al.* Perspectives on Low-Temperature Electrolysis and Potential for Renewable Hydrogen at Scale. *Annu Rev Chem Biomol Eng* **10,** 219–239 (2019).

90. Ayers, K. E. *et al.* Pathways to ultra-low platinum group metal catalyst loading in proton exchange membrane electrolyzers. *Catalysis Today* **262,** 121–132 (2016).

91. Hufnagel, A. G. *et al.* Carbon-templated conductive oxide supports for oxygen evolution catalysis. *Nanoscale* **11,** 14285–14293 (2019).

92. Kibsgaard, J. & Chorkendorff, I. Considerations for the scaling-up of water splitting catalysts. *Nature Energy* **4,** 430–433 (2019).

93. Diaz-Morales, O. *et al.* Iridium-based double perovskites for efficient water oxidation in acid media. *Nat Commun* **7,** 12363 (2016).

94. Montoya, J. H. *et al.* Materials for solar fuels and chemicals. *Nat Mater* **16,** 70–81 (2016).

95. Yang, L. *et al.* Efficient oxygen evolution electrocatalysis in acid by a perovskite with face-sharing IrO_6 octahedral dimers. *Nat Commun* **9,** 5236 (2018).

96. Chen, Y. *et al.* Exceptionally active iridium evolved from a pseudo-cubic perovskite for oxygen evolution in acid. *Nat Commun* **10,** 572 (2019).

97. Wang, W., Xu, M., Xu, X., Zhou, W. & Shao, Z. Perovskite Oxide Based Electrodes for High-Performance Photoelectrochemical Water Splitting. *Angew Chem Int Ed Engl* **59,** 136–152 (2020).

98. Song, H. J., Yoon, H., Ju, B. & Kim, D.-W. Highly Efficient Perovskite-Based Electrocatalysts for Water Oxidation in Acidic Environments: A Mini Review. *Advanced Energy Materials* (2020).

99. Strickler, A. L. *et al.* Systematic Investigation of Iridium-Based Bimetallic Thin Film Catalysts for the Oxygen Evolution Reaction in Acidic Media. *ACS Appl Mater Interfaces* **11,** 34059–34066 (2019).

100. Nong, H. N. *et al.* Oxide-supported $IrNiO_x$ core-shell particles as efficient, cost-effective, and stable catalysts for electrochemical water splitting. *Angew Chem Int Ed Engl* **54,** 2975–2979 (2015).

101. Bernsmeier, D. *et al.* Oxygen Evolution Catalysts Based on Ir-Ti Mixed Oxides with Templated Mesopore Structure: Impact of Ir on Activity and Conductivity. *ChemSusChem* **11,** 2367–2374 (2018).

102. Böhm, D. *et al.* Efficient OER Catalyst with Low Ir Volume Density Obtained by Homogeneous Deposition of Iridium Oxide Nanoparticles on Macroporous Antimony-Doped Tin Oxide Support. *Advanced Functional Materials* **30,** 1906670 (2019).

103. Regmi, Y. N. *et al.* Supported Oxygen Evolution Catalysts by Design: Toward Lower Precious Metal Loading and Improved Conductivity in Proton Exchange Membrane Water Electrolyzers. *ACS Catalysis,* 13125–13135 (2020).

104. Hartig-Weiss, A. *et al.* Iridium Oxide Catalyst Supported on Antimony-Doped Tin Oxide for High Oxygen Evolution Reaction Activity in Acidic Media. *ACS Applied Nano Materials* **3,** 2185–2196 (2020).

105. Saveleva, V. A. *et al.* Insight into the Mechanisms of High Activity and Stability of Iridium Supported on Antimony-Doped Tin Oxide Aerogel for Anodes of Proton Exchange Membrane Water Electrolyzers. *ACS Catalysis* **10,** 2508–2516 (2020).

106. Kasian, O., Grote, J. P., Geiger, S., Cherevko, S. & Mayrhofer, K. J. J. The Common Intermediates of Oxygen Evolution and Dissolution Reactions during Water Electrolysis on Iridium. *Angew Chem Int Ed Engl* **57,** 2488–2491 (2018).

107. Zhao, Y., Hernandez-Pagan, E. A., Vargas-Barbosa, N. M., Dysart, J. L. & Mallouk, T. E. A high yield synthesis of ligand-free iridium oxide nanoparticles with high electrocatalytic activity. *Journal of Physical Chemistry Letters* **2,** 402–406 (2011).

108. Lee, Y., Suntivich, J., May, K. J., Perry, E. E. & Shao-Horn, Y. Synthesis and Activities of Rutile IrO_2 and RuO_2 Nanoparticles for Oxygen Evolution in Acid and Alkaline Solutions. *J Phys Chem Lett* **3,** 399–404 (2012).

109. Kötz, R., Neff, H. & Stucki, S. Anodic Iridium Oxide Films: XPS-Studies of Oxidation State Changes and O_2 evolution. *Journal of The Electrochemical Society* **131,** 72–77 (1984).

110. Cherevko, S., Geiger, S., Kasian, O., Mingers, A. & Mayrhofer, K. J. Oxygen evolution activity and stability of iridium in acidic media. Part 2. - Electrochemically grown hydrous iridium oxide. *Journal of Electroanalytical Chemistry* **774,** 102–110 (2016).

111. Da Silva, G. C., Perini, N. & Ticianelli, E. A. Effect of temperature on the activities and stabilities of hydrothermally prepared IrO_x nanocatalyst layers for the oxygen evolution reaction. *Applied Catalysis B: Environmental* **218,** 287–297 (2017).

112. Geiger, S. *et al.* Activity and Stability of Electrochemically and Thermally Treated Iridium for the Oxygen Evolution Reaction. *Journal of The Electrochemical Society* **163,** F3132–F3138 (2016).

113. Kasian, O. *et al.* Degradation of iridium oxides via oxygen evolution from the lattice: correlating atomic scale structure with reaction mechanisms. *Energy & Environmental Science* **12,** 3548–3555 (2019).

114. Geiger, S. *Stability investigations of iridium-based catalysts towards acidic water splitting* PhD Thesis, Ruhr-Universität Bochum (2017).

115. El-Sayed, H. A., Weiss, A., Olbrich, L. F., Putro, G. P. & Gasteiger, H. A. OER Catalyst Stability Investigation Using RDE Technique: A Stability Measure or an Artifact? *Journal of the Electrochemical Society* **166,** F458–F464 (2019).

116. Hartig-Weiss, A., Tovini, M. F., Gasteiger, H. A. & El-Sayed, H. A. OER Catalyst Durability Tests Using the Rotating Disk Electrode Technique: The Reason Why This Leads to Erroneous Conclusions. *ACS Applied Energy Materials* **3,** 10323–10327 (2020).

117. Browne, M. P. *et al.* Oxygen evolution catalysts under proton exchange membrane conditions in a conventional three electrode cell vs. electrolyser device: a comparison study and a 3D-printed electrolyser for academic labs. *Journal of Materials Chemistry A* **9,** 9113–9123 (2021).

118. Babic, U., Tarik, M., Schmidt, T. J. & Gubler, L. Understanding the effects of material properties and operating conditions on component aging in polymer electrolyte water electrolyzers. *Journal of Power Sources* **451,** 227778 (2020).

119. Regmi, Y. N. *et al.* A low temperature unitized regenerative fuel cell realizing 60% round trip efficiency and 10,000 cycles of durability for energy storage applications. *Energy & Environmental Science* **13,** 2096–2105 (2020).

120. Zeng, K. & Zhang, D. Recent progress in alkaline water electrolysis for hydrogen production and applications. *Progress in Energy and Combustion Science* **36,** 307–326 (2010).

121. Kraglund, M. R. *et al.* Ion-solvating membranes as a new approach towards high rate alkaline electrolyzers. *Energy & Environmental Science* **12,** 3313–3318 (2019).

122. Miller, H. A. *et al.* Green hydrogen from anion exchange membrane water electrolysis: a review of recent developments in critical materials and operating conditions. *Sustainable Energy & Fuels* **4,** 2114–2133 (2020).

123. Abbasi, R. *et al.* A Roadmap to Low-Cost Hydrogen with Hydroxide Exchange Membrane Electrolyzers. *Adv Mater* **31,** e1805876 (2019).

124. Lindquist, G. A., Xu, Q., Oener, S. Z. & Boettcher, S. W. Membrane Electrolyzers for Impure-Water Splitting. *Joule* **4,** 2549–2561 (2020).

125. Giesbrecht, P. K. & Freund, M. S. Recent Advances in Bipolar Membrane Design and Applications. *Chemistry of Materials* **32,** 8060–8090 (2020).

126. Mayerhöfer, B. *et al.* Bipolar Membrane Electrode Assemblies for Water Electrolysis. *ACS Applied Energy Materials* **3,** 9635–9644 (2020).

127. Oener, S. Z., Foster, M. J. & Boettcher, S. W. Accelerating water dissociation in bipolar membranes and for electrocatalysis. *Science* **369,** 1099–1103 (2020).

128. Zheng, Y. *et al.* A review of high temperature co-electrolysis of H_2O and CO_2 to produce sustainable fuels using solid oxide electrolysis cells (SOECs): advanced materials and technology. *Chem Soc Rev* **46,** 1427–1463 (2017).

129. Fujishima, A. & Honda, K. Electrochemical photolysis of water at a semiconductor electrode. *Nature* **238,** 37–38 (1972).

130. NREL. *Reference Air Mass 1.5G Spectra* Web Page. 1976. `https://www.nrel.gov/grid/solar-resource/spectra-am1.5.html`.

131. Khaselev, O. & Turner, J. A. A monolithic photovoltaic-photoelectrochemical device for hydrogen production via water splitting. *Science* **280,** 425–427 (1998).

132. Cheng, W.-H. *et al.* Monolithic Photoelectrochemical Device for Direct Water Splitting with 19% Efficiency. *ACS Energy Letters* **3,** 1795–1800 (2018).

133. Ahmet, I. Y. *et al.* Demonstration of a 50 cm^2 $BiVO_4$ tandem photoelectrochemical-photovoltaic water splitting device. *Sustainable Energy & Fuels* **3,** 2366–2379 (2019).

134. Vilanova, A. *et al.* Solar water splitting under natural concentrated sunlight using a 200 cm^2 photoelectrochemical-photovoltaic device. *Journal of Power Sources* **454,** 227890 (2020).

135. Tembhurne, S., Nandjou, F. & Haussener, S. A thermally synergistic photoelectrochemical hydrogen generator operating under concentrated solar irradiation. *Nature Energy* **4,** 399–407 (2019).

136. Sivula, K. & van de Krol, R. Semiconducting materials for photoelectrochemical energy conversion. *Nature Reviews Materials* **1,** 15010 (2016).

137. Parkinson, B. On the efficiency and stability of photoelectrochemical devices. *Accounts of Chemical Research* **17,** 431–437 (1984).

138. Nandjou, F. & Haussener, S. Degradation in photoelectrochemical devices: Review with an illustrative case study. *Journal of Physics D: Applied Physics* **50,** 124002 (2017).

139. Ben-Naim, M. *et al.* Addressing the Stability Gap in Photoelectrochemistry: Molybdenum Disulfide Protective Catalysts for Tandem III–V Unassisted Solar Water Splitting. *ACS Energy Letters,* 2631–2640 (2020).

140. Seabold, J. A. & Choi, K.-S. Effect of a Cobalt-Based Oxygen Evolution Catalyst on the Stability and the Selectivity of Photo-Oxidation Reactions of a WO_3 Photoanode. *Chemistry of Materials* **23,** 1105–1112 (2011).

141. Bae, D. *et al.* Carrier-selective p- and n-contacts for efficient and stable photocatalytic water reduction. *Catalysis Today* **290,** 59–64 (2017).

142. Bolts, J. M. & Wrighton, M. S. Correlation of photocurrent-voltage curves with flat-band potential for stable photoelectrodes for the photoelectrolysis of water. *The Journal of Physical Chemistry* **80,** 2641–2645 (1976).

143. Janáky, C., Rajeshwar, K., De Tacconi, N. R., Chanmanee, W. & Huda, M. N. Tungsten-based oxide semiconductors for solar hydrogen generation. *Catalysis Today* **199,** 53–64 (2013).

144. Bignozzi, C. A. *et al.* Nanostructured photoelectrodes based on WO_3: applications to photooxidation of aqueous electrolytes. *Chem Soc Rev* **42,** 2228–2246 (2013).

145. Zheng, H. *et al.* Nanostructured Tungsten Oxide - Properties, Synthesis, and Applications. *Advanced Functional Materials* **21,** 2175–2196 (2011).

146. Kwong, W. L., Savvides, N. & Sorrell, C. C. Electrodeposited nanostructured WO_3 thin films for photoelectrochemical applications. *Electrochimica Acta* **75,** 371–380 (2012).

147. Meulenkamp, E. A. Mechanism of WO_3 Electrodeposition from Peroxy-Tungstate Solution. *Journal of The Electrochemical Society* **144,** 1664 (1997).

148. Kim, C.-Y., Lee, M., Huh, S.-H. & Kim, E.-K. WO_3 thin film coating from H_2O-controlled peroxotungstic acid and its electrochromic properties. *Journal of Sol-Gel Science and Technology* **53,** 176–183 (2009).

149. Yamanaka, K., Oakamoto, H., Kidou, H. & Kudo, T. Peroxotungstic Acid Coated Films for Electrochromic Display Devices. *Japanese Journal of Applied Physics* **25,** 1420–1426 (1986).

150. Vidmar, T., Topič, M., Dzik, P. & Opara Krašovec, U. Inkjet printing of sol–gel derived tungsten oxide inks. *Solar Energy Materials and Solar Cells* **125,** 87–95 (2014).

151. Chen, S. & Wang, L.-W. Thermodynamic Oxidation and Reduction Potentials of Photocatalytic Semiconductors in Aqueous Solution. *Chemistry of Materials* **24,** 3659–3666 (2012).

152. Klemm, S. O., Topalov, A. A., Laska, C. A. & Mayrhofer, K. J. J. Coupling of a high throughput microelectrochemical cell with online multielemental trace analysis by ICP-MS. *Electrochemistry Communications* **13,** 1533–1535 (2011).

153. Cherevko, S., Zeradjanin, A. R., Keeley, G. P. & Mayrhofer, K. J. J. A Comparative Study on Gold and Platinum Dissolution in Acidic and Alkaline Media. *Journal of The Electrochemical Society* **161,** H822–H830 (2014).

154. Topalov, A. A. *et al.* Towards a comprehensive understanding of platinum dissolution in acidic media. *Chem. Sci.* **5,** 631–638 (2014).

155. Cherevko, S., Topalov, A. A., Zeradjanin, A. R., Keeley, G. P. & Mayrhofer, K. J. J. Temperature-Dependent Dissolution of Polycrystalline Platinum in Sulfuric Acid Electrolyte. *Electrocatalysis* **5,** 235–240 (2014).

156. Grote, J. P., Zeradjanin, A. R., Cherevko, S. & Mayrhofer, K. J. Coupling of a scanning flow cell with online electrochemical mass spectrometry for screening of reaction selectivity. *Rev Sci Instrum* **85,** 104101 (2014).

157. Grote, J.-P. *et al.* Screening of material libraries for electrochemical CO_2 reduction catalysts – Improving selectivity of Cu by mixing with Co. *Journal of Catalysis* **343,** 248–256 (2016).

158. Khanipour, P. *et al.* Electrochemical Real-Time Mass Spectrometry (EC-RTMS): Monitoring Electrochemical Reaction Products in Real Time. *Angew Chem Int Ed Engl* **58,** 7273–7277 (2019).

159. Löffler, M., Khanipour, P., Kulyk, N., Mayrhofer, K. J. J. & Katsounaros, I. Insights into Liquid Product Formation during Carbon Dioxide Reduction on Copper and Oxide-Derived Copper from Quantitative Real-Time Measurements. *ACS Catalysis* **10,** 6735–6740 (2020).

160. Martić, N. *et al.* $Ag_2Cu_2O_3$ – a catalyst template material for selective electroreduction of CO to C_2^+ products. *Energy & Environmental Science* **13,** 2993–3006 (2020).

161. Ranninger, J., Wachs, S. J., Möller, J., Mayrhofer, K. J. J. & Berkes, B. B. On-line monitoring of dissolution processes in nonaqueous electrolytes – A case study with platinum. *Electrochemistry Communications* **114,** 106702 (2020).

162. Ranninger, J. *et al.* Dissolution of Pt and Its Temperature Dependence in Anhydrous Acetonitrile- and Methanol-Based Electrolytes. *Journal of The Electrochemical Society* **167,** 121507 (2020).

163. Wachs, S. J. *et al.* Online Monitoring of Transition-Metal Dissolution from a High-Ni-Content Cathode Material. *ACS Appl Mater Interfaces* **13,** 33075–33082 (2021).

164. Knöppel, J. *et al.* On the limitations in assessing stability of oxygen evolution catalysts using aqueous model electrochemical cells. *Nat Commun* **12,** 2231 (2021).

165. Sandbeck, D. J. S. *On the Dissolution of Platinum: From Fundamental to Advanced Catalytic Materials* PhD Thesis, Friedrich-Alexander-Universiät Erlangen-Nürnberg (2020).

166. Speck, F. D. *et al.* On the Electrolytic Stability of Iron-Nickel Oxides. *Chem* **2,** 590–597 (2017).

167. Nanba, T., Takano, S., Yasui, I. & Kudo, T. Structural study of peroxopolytungstic acid prepared from metallic tungsten and hydrogen peroxide. *Journal of Solid State Chemistry* **90,** 47–53 (1991).

168. Kim, Y. T. *et al.* Balancing activity, stability and conductivity of nanoporous core-shell iridium/iridium oxide oxygen evolution catalysts. *Nat Commun* **8,** 1449 (2017).

169. Siracusano, S. *et al.* New insights into the stability of a high performance nanostructured catalyst for sustainable water electrolysis. *Nano Energy* **40,** 618–632 (2017).

170. Rozain, C., Mayousse, E., Guillet, N. & Millet, P. Influence of iridium oxide loadings on the performance of PEM water electrolysis cells: Part II – Advanced oxygen electrodes. *Applied Catalysis B: Environmental* **182,** 123–131 (2016).

171. Shkirskiy, V., Speck, F. D., Kulyk, N. & Cherevko, S. On the Time Resolution of Electrochemical Scanning Flow Cell Coupled to Downstream Analysis. *Journal of The Electrochemical Society* **166,** H866–H870 (2019).

172. Giordano, L. *et al.* pH dependence of OER activity of oxides: Current and future perspectives. *Catalysis Today* **262,** 2–10 (2016).

173. Rakousky, C., Keeley, G. P., Wippermann, K., Carmo, M. & Stolten, D. The stability challenge on the pathway to high-current-density polymer electrolyte membrane water electrolyzers. *Electrochimica Acta* **278,** 324–331 (2018).

174. Kopp, M. *et al.* Energiepark Mainz: Technical and economic analysis of the worldwide largest Power-to-Gas plant with PEM electrolysis. *International Journal of Hydrogen Energy* **42,** 13311–13320 (2017).

175. Pinaud, B. A., Bonakdarpour, A., Daniel, L., Sharman, J. & Wilkinson, D. P. Key Considerations for High Current Fuel Cell Catalyst Testing in an Electrochemical Half-Cell. *Journal of The Electrochemical Society* **164,** F321–F327 (2017).

176. Ehelebe, K. *et al.* Evaluating Electrocatalysts at Relevant Currents in a Half-Cell: The Impact of Pt Loading on Oxygen Reduction Reaction. *Journal of The Electrochemical Society* **166,** F1259–F1268 (2019).

177. Inaba, M. *et al.* Benchmarking high surface area electrocatalysts in a gas diffusion electrode: measurement of oxygen reduction activities under realistic conditions. *Energy & Environmental Science* **11,** 988–994 (2018).

178. Ehelebe, K. *et al.* Platinum Dissolution in Realistic Fuel Cell Catalyst Layers. *Angew Chem Int Ed Engl* **60,** 8882–8888 (2021).

179. Schröder, J. *et al.* The Gas Diffusion Electrode Setup as Straightforward Testing Device for Proton Exchange Membrane Water Electrolyzer Catalysts. *JACS Au* **1,** 247–251 (2021).

180. Langemann, M., Fritz, D. L., Müller, M. & Stolten, D. Validation and characterization of suitable materials for bipolar plates in PEM water electrolysis. *International Journal of Hydrogen Energy* **40,** 11385–11391 (2015).

181. Gregoire, J. M., Xiang, C., Liu, X., Marcin, M. & Jin, J. Scanning droplet cell for high throughput electrochemical and photoelectrochemical measurements. *Review of Scientific Instruments* **84,** 024102 (2013).

182. Kollender, J. P., Mardare, A. I. & Hassel, A. W. Localized photoelectrochemistry on a tungsten oxide-iron oxide thin film material library. *ACS Comb Sci* **15,** 601–608 (2013).

183. Sliozberg, K. *et al.* High-throughput screening of thin-film semiconductor material libraries I: system development and case study for Ti-W-O. *ChemSusChem* **8,** 1270–1278 (2015).

184. Knöppel, J. *et al.* Time-resolved analysis of dissolution phenomena in photoelectrochemistry – A case study of WO_3 photocorrosion. *Electrochemistry Communications* **96,** 53–56 (2018).

185. Cherevko, S., Topalov, A. A., Katsounaros, I. & Mayrhofer, K. J. J. Electrochemical dissolution of gold in acidic medium. *Electrochemistry Communications* **28,** 44–46 (2013).

186. Hilliard, S. *et al.* Mesoporous thin film WO_3 photoanode for photoelectrochemical water splitting: a sol–gel dip coating approach. *Sustainable Energy & Fuels* **1,** 145–153 (2017).

187. Yang, B., Barnes, P. R. F., Bertram, W. & Luca, V. Strong photoresponse of nanostructured tungsten trioxide films prepared via a sol–gel route. *J. Mater. Chem.* **17,** 2722–2729 (2007).

188. Yang, B., Zhang, Y., Drabarek, E., Barnes, P. R. F. & Luca, V. Enhanced Photoelectrochemical Activity of Sol-Gel Tungsten Trioxide Films through Textural Control. *Chemistry of Materials* **19,** 5664–5672 (2007).

189. Butler, M. A. Photoelectrolysis and physical properties of the semiconducting electrode WO_3. *Journal of Applied Physics* **48,** 1914–1920 (1977).

190. Tanaka, D., Oaki, Y. & Imai, H. Enhanced photocatalytic activity of quantum-confined tungsten trioxide nanoparticles in mesoporous silica. *Chem Commun (Camb)* **46,** 5286–5288 (2010).

191. Danilovic, N. *et al.* Activity-Stability Trends for the Oxygen Evolution Reaction on Monometallic Oxides in Acidic Environments. *J Phys Chem Lett* **5,** 2474–8 (2014).

192. Cherevko, S., Zeradjanin, A. R., Topalov, A. A., Keeley, G. P. & Mayrhofer, K. J. J. Effect of Temperature on Gold Dissolution in Acidic Media. *Journal of The Electrochemical Society* **161,** H501–H507 (2014).

193. Gerischer, H. On the stability of semiconductor electrodes against photodecomposition. *Journal of Electroanalytical Chemistry and Interfacial Electrochemistry* **82,** 133–143 (1977).

194. Hill, J. C. & Choi, K.-S. Effect of Electrolytes on the Selectivity and Stability of n-type WO_3 Photoelectrodes for Use in Solar Water Oxidation. *The Journal of Physical Chemistry C* **116,** 7612–7620 (2012).

195. Reinhard, S., Rechberger, F. & Niederberger, M. Commercially Available WO_3 Nanopowders for Photoelectrochemical Water Splitting: Photocurrent versus Oxygen Evolution. *ChemPlusChem* **81,** 935–940 (2016).

196. Mi, Q., Coridan, R. H., Brunschwig, B. S., Gray, H. B. & Lewis, N. S. Photoelectrochemical oxidation of anions by WO_3 in aqueous and nonaqueous electrolytes. *Energy & Environmental Science* **6,** 2646 (2013).

197. Mi, Q., Zhanaidarova, A., Brunschwig, B. S., Gray, H. B. & Lewis, N. S. A quantitative assessment of the competition between water and anion oxidation at WO_3 photoanodes in acidic aqueous electrolytes. *Energy & Environmental Science* **5,** 5694 (2012).

198. Solarska, R., Jurczakowski, R. & Augustynski, J. A highly stable, efficient visible-light driven water photoelectrolysis system using a nanocrystalline WO_3 photoanode and a methane sulfonic acid electrolyte. *Nanoscale* **4,** 1553–1556 (2012).

199. Nakajima, T., Hagino, A., Nakamura, T., Tsuchiya, T. & Sayama, K. WO_3 nanosponge photoanodes with high applied bias photon-to-current efficiency for solar hydrogen and peroxydisulfate production. *Journal of Materials Chemistry A* **4,** 17809–17818 (2016).

200. Knöppel, J. *et al.* Photocorrosion of WO_3 Photoanodes in different electrolytes. *ACS Physical Chemistry Au.* `https://doi.org/10.1021/acsphyschemau.1c00004` (2021).

201. Samu, G. F. & Janaky, C. Photocorrosion at Irradiated Perovskite/Electrolyte Interfaces. *J Am Chem Soc* **142,** 21595–21614 (2020).

202. Grazulis, S. *et al.* Crystallography Open Database - an open-access collection of crystal structures. *J Appl Crystallogr* **42,** 726–729 (2009).

203. Hilaire, S. *et al.* Microwave-assisted nonaqueous synthesis of WO3nanoparticles for crystallographically oriented photoanodes for water splitting. *J. Mater. Chem. A* **2,** 20530–20537 (2014).

204. Tacca, A. *et al.* Photoanodes based on nanostructured WO_3 for water splitting. *Chemphyschem* **13,** 3025–3034 (2012).

205. Huang, Z., Miseki, Y. & Sayama, K. Solar-light-driven photocatalytic production of peroxydisulfate over noble-metal loaded WO_3. *Chem Commun (Camb)* **55,** 3813–3816 (2019).

206. Xie, W., Huang, Z., Wang, R., Wen, C. & Zhou, Y. Metallic Pt and PtO_x dual-cocatalyst-loaded WO_3 for photocatalytic production of peroxydisulfate and hydrogen peroxide. *Journal of Materials Science* **55,** 11829–11840 (2020).

207. Zhang, S. *et al.* Different Photostability of $BiVO_4$ in Near-pH-Neutral Electrolytes. *ACS Appl Energy Mater* **3,** 9523–9527 (2020).

208. Paulsen, A. L., Kalampounias, A. G., Berg, R. W. & Boghosian, S. Raman spectroscopic study of tungsten(VI) oxosulfato complexes in WO_3-$K_2S_2O_7$-K_2SO_4 molten mixtures: stoichiometry, vibrational properties, and molecular structure. *J Phys Chem A* **115,** 4214–4222 (2011).

209. Geiger, S., Cherevko, S. & Mayrhofer, K. J. J. Dissolution of Platinum in Presence of Chloride Traces. *Electrochimica Acta* **179,** 24–31 (2015).

210. Knöppel, J. *et al.* Enhanced photostability of WO3 photoanodes through iridium atomic layer deposition. *Unpublished work* (2021).

211. Bae, D., Seger, B., Vesborg, P. C., Hansen, O. & Chorkendorff, I. Strategies for stable water splitting via protected photoelectrodes. *Chem Soc Rev* **46,** 1933–1954 (2017).

212. Mei, B. *et al.* Crystalline TiO_2: A Generic and Effective Electron-Conducting Protection Layer for Photoanodes and -cathodes. *The Journal of Physical Chemistry C* **119,** 15019–15027 (2015).

213. Tang-Kong, R. *et al.* The Role of Catalyst Adhesion in ALD-TiO_2 Protection of Water Splitting Silicon Anodes. *ACS Applied Materials & Interfaces* **10,** 37103–37109 (2018).

214. Scheuermann, A. G., Prange, J. D., Gunji, M., Chidsey, C. E. D. & McIntyre, P. C. Effects of catalyst material and atomic layer deposited TiO_2 oxide thickness on the water oxidation performance of metal–insulator–silicon anodes. *Energy & Environmental Science* **6.** ISSN: 1754-5692 1754-5706 (2013).

215. Papp, J., Soled, S., Dwight, K. & Wold, A. Surface Acidity and Photocatalytic Activity of TiO_2, WO_3/TiO_2, and MoO_3/TiO_2 Photocatalysts. *Chemistry of Materials* **6,** 496–500 (1994).

216. Mei, B. *et al.* Protection of p(+)-n-Si Photoanodes by Sputter-Deposited Ir/IrOx Thin Films. *J Phys Chem Lett* **5,** 1948–1952 (2014).

217. Ben-Naim, M. *et al.* A Spin Coating Method To Deposit Iridium-Based Catalysts onto Silicon for Water Oxidation Photoanodes. *ACS Appl Mater Interfaces* **12,** 5901–5908 (2020).

218. Janáky, C., Chanmanee, W. & Rajeshwar, K. On the Substantially Improved Photoelectrochemical Properties of Nanoporous WO_3 Through Surface Decoration with RuO_2. *Electrocatalysis* **4,** 382–389 (2013).

219. Zhao, Y. *et al.* End-On Bound Iridium Dinuclear Heterogeneous Catalysts on WO_3 for Solar Water Oxidation. *ACS Cent Sci* **4,** 1166–1172 (2018).

220. Spurgeon, J. M., Velazquez, J. M. & McDowell, M. T. Improving O_2 production of WO_3 photoanodes with IrO_2 in acidic aqueous electrolyte. *Phys Chem Chem Phys* **16,** 3623–3631 (2014).

221. Fleisch, T. H. & Mains, G. J. An XPS study of the UV reduction and photochromism of MoO_3 and WO_3. *The Journal of Chemical Physics* **76,** 780–786 (1982).

222. Kasian, O. *et al.* Using Instability of a Non-stoichiometric Mixed Oxide Oxygen Evolution Catalyst As a Tool to Improve Its Electrocatalytic Performance. *Electrocatalysis* **9,** 139–145 (2017).

223. Schlicht, S., Haschke, S., Mikhailovskii, V., Manshina, A. & Bachmann, J. Highly Reversible Water Oxidation at Ordered Nanoporous Iridium Electrodes Based on an Original Atomic Layer Deposition. *ChemElectroChem* **5,** 1259–1264 (2018).

224. Hämäläinen, J., Ritala, M. & Leskelä, M. Atomic Layer Deposition of Noble Metals and Their Oxides. *Chemistry of Materials* **26,** 786–801 (2013).

225. Cherevko, S., Geiger, S., Kasian, O., Mingers, A. & Mayrhofer, K. J. Oxygen evolution activity and stability of iridium in acidic media. Part 1. - Metallic iridium. *Journal of Electroanalytical Chemistry* **773,** 69–78 (2016).

226. Grätzel, M. Photoelectrochemical cells. *Nature* **414,** 338–344 (2001).

227. Zhao, Y. *et al.* Stable iridium dinuclear heterogeneous catalysts supported on metal-oxide substrate for solar water oxidation. *Proc Natl Acad Sci U S A* **115,** 2902–2907 (2018).

228. Siegmund, D. *et al.* Crossing the Valley of Death: From Fundamental to Applied Research in Electrolysis. *JACS Au* **1,** 527–535 (2021).

229. Zhang, S. Y. *et al.* Dissolution of $BiVO_4$ Photoanodes Revealed by Time-Resolved Measurements under Photoelectrochemical Conditions. *Journal of Physical Chemistry C* **123,** 23410–23418 (2019).

230. Dworschak, D., Brunnhofer, C. & Valtiner, M. Photocorrosion of ZnO Single Crystals during Electrochemical Water Splitting. *ACS Applied Materials & Interfaces* **12,** 51530–51536 (2020).

231. Mayerhöfer, B. *et al.* On the effect of anion exchange ionomer binders in bipolar electrode membrane interface water electrolysis. *Journal of Materials Chemistry A* **9,** 14285–14295 (2021).

232. Jenewein, K. J., Kormányos, A., Knöppel, J., Mayrhofer, K. J. J. & Cherevko, S. Accessing In Situ Photocorrosion under Realistic Light Conditions: Photoelectrochemical Scanning Flow Cell Coupled to Online ICP-MS. *ACS Measurement Science Au.* `https://doi.org/10.1021/acsmeasuresciau.1c00016` (2021).

List of Figures

Appendix

1 ICP-MS standards

Analyte	Internal Standard	c(IS)/µg l^{-1}
Ir	Re	10
Au	Re	10
Pt	Re	10
Ti	Sc	10
Ru	Rh	10
W	Re	10

Table 1: *List of internal standards used for ICP-MS experiments and their respective concentrations*